



Publication Year	2017
Acceptance in OA	2021-01-05T09:54:34Z
Title	KiDS-450: cosmological parameter constraints from tomographic weak gravitational lensing
Authors	Hildebrandt, H., Viola, M., Heymans, C., Joudaki, S., Kuijken, K., Blake, C., Erben, T., Joachimi, B., Klaes, D., Miller, L., Morrison, C. B., Nakajima, R., Verdoes Kleijn, G., Amon, A., Choi, A., Covone, G., de Jong, J. T. A., Dvornik, A., Fenech Conti, I., GRADO, ANIELLO, Harnois-Déraps, J., Herbonnet, R., Hoekstra, H., Köhlinger, F., McFarland, J., Mead, A., Merten, J., NAPOLITANO, NICOLA ROSARIO, Peacock, J. A., RADOVICH, MARIO, Schneider, P., Simon, P., Valentijn, E. A., van den Busch, J. L., van Uitert, E., Van Waerbeke, L.
Publisher's version (DOI)	10.1093/mnras/stw2805
Handle	http://hdl.handle.net/20.500.12386/29478
Journal	MONTHLY NOTICES OF THE ROYAL ASTRONOMICAL SOCIETY
Volume	465



KiDS-450: cosmological parameter constraints from tomographic weak gravitational lensing

H. Hildebrandt,¹ M. Viola,² C. Heymans,³ S. Joudaki,⁴ K. Kuijken,² C. Blake,⁴ T. Erben,¹ B. Joachimi,⁵ D. Klaes,¹ L. Miller,⁶ C. B. Morrison,¹ R. Nakajima,¹ G. Verdoes Kleijn,⁷ A. Amon,³ A. Choi,³ G. Covone,⁸ J. T. A. de Jong,² A. Dvornik,² I. Fenech Conti,^{9,10} A. Grado,¹¹ J. Harnois-Déraps,^{3,12} R. Herbonnet,² H. Hoekstra,² F. Köhlinger,² J. McFarland,⁷ A. Mead,¹² J. Merten,⁶ N. Napolitano,¹¹ J. A. Peacock,³ M. Radovich,¹³ P. Schneider,¹ P. Simon,¹ E. A. Valentijn,⁷ J. L. van den Busch,¹ E. van Uitert⁵ and L. Van Waerbeke¹²

Affiliations are listed at the end of the paper

Accepted 2016 October 28. Received 2016 October 28; in original form 2016 June 16

ABSTRACT

We present cosmological parameter constraints from a tomographic weak gravitational lensing analysis of $\sim 450 \text{ deg}^2$ of imaging data from the Kilo Degree Survey (KiDS). For a flat Λ cold dark matter (ΛCDM) cosmology with a prior on H_0 that encompasses the most recent direct measurements, we find $S_8 \equiv \sigma_8 \sqrt{\Omega_m/0.3} = 0.745 \pm 0.039$. This result is in good agreement with other low-redshift probes of large-scale structure, including recent cosmic shear results, along with pre-*Planck* cosmic microwave background constraints. A 2.3σ tension in S_8 and ‘substantial discordance’ in the full parameter space is found with respect to the *Planck* 2015 results. We use shear measurements for nearly 15 million galaxies, determined with a new improved ‘self-calibrating’ version of lensfit validated using an extensive suite of image simulations. Four-band *ugri* photometric redshifts are calibrated directly with deep spectroscopic surveys. The redshift calibration is confirmed using two independent techniques based on angular cross-correlations and the properties of the photometric redshift probability distributions. Our covariance matrix is determined using an analytical approach, verified numerically with large mock galaxy catalogues. We account for uncertainties in the modelling of intrinsic galaxy alignments and the impact of baryon feedback on the shape of the non-linear matter power spectrum, in addition to the small residual uncertainties in the shear and redshift calibration. The cosmology analysis was performed blind. Our high-level data products, including shear correlation functions, covariance matrices, redshift distributions, and Monte Carlo Markov chains are available at <http://kids.strw.leidenuniv.nl>.

Key words: gravitational lensing: weak – surveys – galaxies: photometry – cosmology: observations.

1 INTRODUCTION

The current ‘standard cosmological model’ ties together a diverse set of properties of the observable Universe. Most importantly, it describes the statistics of anisotropies in the cosmic microwave background (CMB) radiation (e.g. Hinshaw et al. 2013; Planck Collaboration XIII 2016a), the Hubble diagram of Type Ia super-

novae (SNIa; e.g. Betoule et al. 2014), big bang nucleosynthesis (e.g. Fields & Olive 2006), and galaxy clustering. It successfully predicts key aspects of the observed large-scale structure, from baryonic acoustic oscillations (e.g. Anderson et al. 2014; Kazin et al. 2014; Ross et al. 2015) on the largest scales down to Mpc-scale galaxy clustering and associated inflow velocities (e.g. Peacock et al. 2001). It is also proving to be a successful paradigm for (predominantly hierarchical) galaxy formation and evolution theories.

This model, based on general relativity, is characterized by a flat geometry, a non-zero cosmological constant Λ that is responsible

*E-mail: hendrik@astro.uni-bonn.de (HH); viola@strw.leidenuniv.nl (MV)

for the late-time acceleration in the expansion of the Universe, and cold dark matter (CDM), which drives cosmological structure formation. Increasingly detailed observations can further stress-test this model, search for anomalies that are not well described by flat Λ CDM, and potentially yield some guidance for a deeper theoretical understanding. Multiple cosmological probes are being studied, and their concordance will be further challenged by the next generation of cosmological experiments.

The two main ways in which to test the cosmological model are observations of the large-scale geometry and the expansion rate of the Universe, and of the formation of structures (inhomogeneities) in the Universe. Both aspects are exploited by modern imaging surveys using the weak gravitational lensing effect of the large-scale structure (cosmic shear; for a review, see Kilbinger 2015). Measuring the coherent distortions of millions of galaxy images as a function of angular separation on the sky and also as a function of their redshifts provides a great amount of cosmological information complementary to other probes. The main benefits of this tomographic cosmic shear technique are its relative insensitivity to galaxy biasing, its clean theoretical description (though there are complications due to baryon physics; see e.g. Semboloni et al. 2011), and its immense potential statistical power compared to other probes (Albrecht et al. 2006).

In terms of precision, currently cosmic shear measurements do not yet yield cosmological parameter constraints that are competitive with other probes, due to the limited cosmological volumes covered by contemporary imaging surveys (see Kilbinger 2015, table 1 and fig. 7). The volumes surveyed by cosmic shear experiments will, however, increase tremendously with the advent of very large surveys such as LSST¹ (see for example Chang et al. 2013), Euclid² (Laureijs et al. 2011), and WFIRST³ over the next decade. In order to harvest the full statistical power of these surveys, our ability to correct for several systematic effects inherent to tomographic cosmic shear measurements will have to keep pace. Each enhancement in statistical precision comes at the price of requiring increasing control on low-level systematic errors. Conversely, only this statistical precision gives us the opportunity to identify, understand, and correct for new systematic effects. It is therefore of utmost importance to develop the cosmic shear technique further and understand systematic errors at the highest level of precision offered by the best data today.

Confidence in the treatment of systematic errors becomes particularly important when a tension between different cosmological probes is found. Recent tomographic cosmic shear results from the Canada–France–Hawaii Telescope Lensing Survey (CFHTLenS;⁴ Heymans et al. 2012, 2013) are in tension with the CMB results from *Planck* (Planck Collaboration XIII 2016a) as described in MacCrann et al. (2015), yielding a lower amplitude of density fluctuations (usually parametrized by the root-mean-square (rms) fluctuations in spheres with a radius of 8 Mpc, σ_8) at a given matter density (Ω_m). A careful reanalysis of the data (Joudaki et al. 2016a) incorporating new knowledge about systematic errors in the photometric redshift (photo- z) distributions (Choi et al. 2016) was not found to alleviate the tension. Only conservative analyses, measuring the lensing power spectrum (Kitching et al. 2014; Köhlinger et al. 2016) or limiting the real-space measurements to large angu-

lar scales (Joudaki et al. 2016a), reduce the tension primarily as a result of the weaker cosmological constraints.

The first results from the Dark Energy Survey (DES; Abbott et al. 2016) do not show such tension, but their uncertainties on cosmological parameters are roughly twice as large as the corresponding constraints from CFHTLenS. In addition to rigorous reanalyses of CFHTLenS with new tests for weak-lensing systematics (Asgari et al. 2017), there have also been claims in the literature of possible residual systematic errors or internal tension in the *Planck* analysis (Spergel, Flauger & Hložek 2015; Addison et al. 2016; Riess et al. 2016). It is hence timely to revisit the question of inconsistencies between CMB and weak-lensing measurements with the best data available.

The ongoing Kilo Degree Survey (KiDS⁵; de Jong et al. 2015) was designed specifically to measure cosmic shear with the best possible image quality attainable from the ground. In this paper, we present intermediate results from 450 deg² (about one-third of the full target area) of the KiDS data set, with the aim to investigate the agreement or disagreement between CMB and cosmic shear observations with new data of comparable statistical power to CFHTLenS but from a different telescope and camera. In addition, the analysis includes an advanced treatment of several potential systematic errors. This paper is organized as follows. We present the KiDS data and their reduction in Section 2, and describe how we calibrate the photometric redshifts in Section 3. Section 4 summarizes the theoretical basis of cosmic shear measurements. Different estimates of the covariance between the elements of the cosmic shear data vector are described in Section 5. We present the shear correlation functions and the results of fitting cosmological models to them in Section 6, followed by a discussion in Section 7. A summary of the findings of this study and an outlook (Section 8) conclude the main body of this paper. The more technical aspects of this work are available in extensive appendices, which cover requirements on shear and photo- z calibration (Appendix A), the absolute photometric calibration with stellar locus regression (SLR; Appendix B), systematic errors in the photo- z calibration (Appendix C), galaxy selection, shear calibration, and E/B-mode analyses (Appendix D), a list of the independent parallel analyses that provide redundancy and validation, right from the initial pixel reduction all the way through to the cosmological parameter constraints (Appendix E), and an exploration of the full multidimensional likelihood chain (Appendix F).

Readers who are primarily interested in the cosmology findings of this study may wish to skip straight to Section 6, referring back to the earlier sections for details of the data and covariance estimate, and of the fitted models.

2 DATA SET AND REDUCTION

In this section, we briefly describe the KiDS-450 data set, highlighting significant updates to our analysis pipeline since it was first documented in the context of the earlier KiDS-DR1/2 data release (de Jong et al. 2015; Kuijken et al. 2015). These major changes include incorporating a global astrometric solution in the data reduction, improved photometric calibration, using spectroscopic training sets to increase the accuracy of our photometric redshift estimates, and analysing the data using an upgraded ‘self-calibrating’ version of the shear measurement method *lensFIT* (Fenech Conti et al. 2016).

¹ <http://www.lsst.org/>

² <http://sci.esa.int/euclid/>

³ <http://wfirst.gsfc.nasa.gov/>

⁴ <http://www.cfhtlens.org/>

⁵ <http://kids.strw.leidenuniv.nl/>

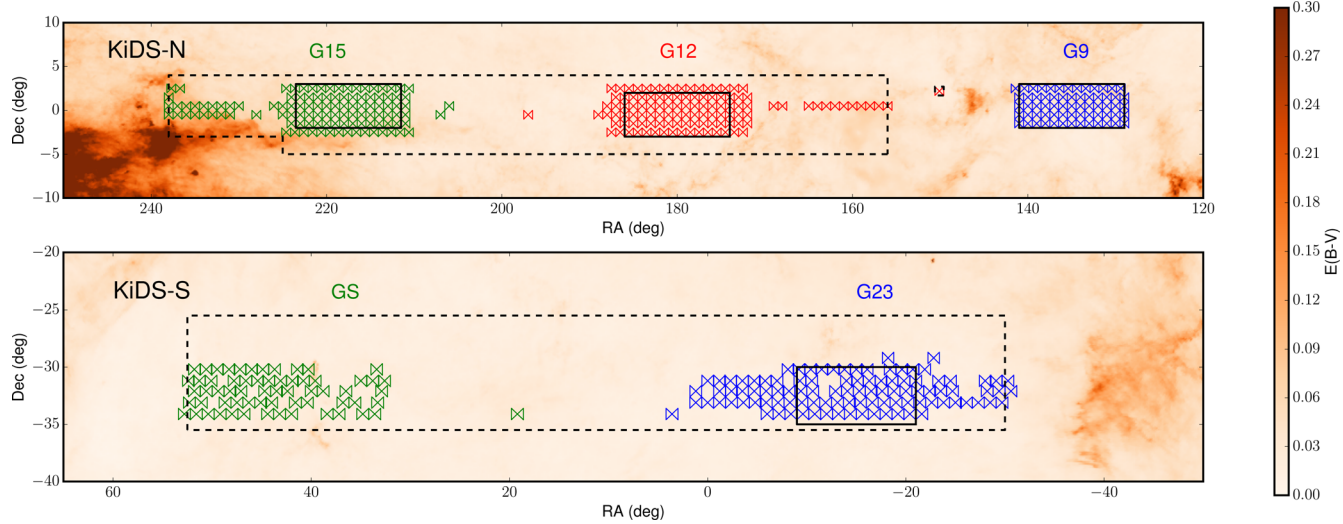


Figure 1. Footprint of the KiDS-450 data set. The dashed contours outline the full KiDS area (observations ongoing) and the $\langle \rangle$ symbols represent the pointings included in KiDS-450 and used in this study corresponding to 449.7 deg^2 . The different colours indicate which pointing belongs to which of the five patches (G9, G12, G15, G23, GS). The solid rectangles indicate the areas observed by the GAMA spectroscopic survey. The background shows the reddening $E(B - V)$ from the Schlegel et al. (1998) maps.

2.1 KiDS-450 data

KiDS is a four-band imaging survey conducted with the Omega-CAM CCD mosaic camera mounted at the Cassegrain focus of the VLT Survey Telescope (VST). This telescope-camera combination, with its small camera shear and its well-behaved and nearly round point spread function (PSF), was specifically designed with weak-lensing measurements in mind. Observations are carried out in the SDSS-like u , g , r , and i bands with total exposure times of 17, 15, 30, and 20 min, respectively. This yields limiting magnitudes of 24.3, 25.1, 24.9, 23.8 (5σ in a 2-arcsec aperture) in $ugri$, respectively. The observations are queue-scheduled such that the best-seeing dark time is reserved for the r -band images, which are used to measure the shapes of galaxies (see Section 2.5). KiDS targets two $\sim 10 \times 75 \text{ deg}^2$ strips, one on the celestial equator (KiDS-N) and the other around the South Galactic Pole (KiDS-S). The survey is constructed from individual dithered exposures that each covers a ‘tile’ of roughly 1 deg^2 at a time.

The basis for our data set is the 472 KiDS tiles which had been observed in four bands on 2015 July 31. These data had also survived initial quality control, but after further checks, some i -band and u -band images were rejected and placed back in the observing queue. Those that were reobserved before 2015 October 4 were incorporated into the analysis where possible such that the final data set consists of 454 tiles covering a total area of 449.7 deg^2 on the sky. The median seeing of the r -band data is 0.66 arcsec with no r -band image having a seeing larger than 0.96 arcsec. The sky distribution of our data set, dubbed ‘KiDS-450’, is shown in Fig. 1. It consists of 2.5 TB of co-added $ugri$ images (for the photometry, see Section 2.2), 3 TB of individual r -band exposures for shear measurements (Section 2.3), and similar amounts of calibration, masks, and weight map data.

Initial KiDS observations prioritized the parts of the sky covered by the spectroscopic GAMA survey (Driver et al. 2011), and these were the basis of the first set of lensing analyses (Sifón et al. 2015; Viola et al. 2015; Brouwer et al. 2016; van Uitert et al. 2016). Even though KiDS currently extends beyond the GAMA regions, we continue to group the tiles in five ‘patches’, which we call G9, G12, G15, G23, and GS, following the convention of the GAMA survey,

with each patch indicated by the letter ‘G’ and a rough RA (hour) value. Note that GS does not have GAMA observations; however, we decided to maintain the naming scheme nevertheless. GS should not be confused with the G2 GAMA patch, which does not overlap with KiDS. Each KiDS patch consists of a central core region as well as nearby survey tiles observed outside the GAMA boundaries. As the survey progresses, these areas will continue to be filled.

2.2 Multicolour processing with ASTRO-WISE

The multicolour KiDS data, from which we estimate photometric redshifts, are reduced and calibrated with the ASTRO-WISE system (Valentijn et al. 2007; Begeman et al. 2013). The reduction closely follows the procedures described in de Jong et al. (2015) for the previous KiDS data release (DR1/2), and we refer the reader to that paper for more in-depth information.

The first phase of data reduction involves detrending the raw data, consisting of the following steps: correction for cross-talk, debiasing, flat-fielding, illumination correction, defringing (only in the i band), masking of hot and cold pixels as well as cosmic rays, satellite track removal, and background subtraction.

Next the data are photometrically calibrated. This is a three-stage process. First, the 32 individual CCDs are assigned photometric zero-points based on nightly observations of standard star fields. Secondly, all CCDs entering a co-add are relatively calibrated with respect to each other using sources in overlap areas. The third step, which was not applied in DR1/2 and is only described as a quality test in de Jong et al. (2015), involves a tile-by-tile SLR with the recipe of Ivezić et al. (2004). This alignment of the colours of the stars in the images (keeping the r -band magnitudes fixed) further homogenizes the data and ensures that the photometric redshifts are based on accurate colours. In the SLR procedure, which is described in detail in Appendix B, we use the Schlegel, Finkbeiner & Davis (1998) maps to correct for Galactic extinction for each individual star.

Astrometric calibration is performed with 2MASS (Skrutskie et al. 2006) as an absolute reference. After that the calibrated images are co-added and further defects (reflections, bright stellar

Table 1. Properties of the galaxy source samples in the four tomographic bins used in the cosmic shear measurement as well as the full KiDS-450 shear catalogue. The effective number density in column 4 is determined with the method proposed by Heymans et al. (2012), whereas the one in column 5 is determined with the method developed by Chang et al. (2013). The ellipticity dispersion in column 6 includes the effect of the *lensfit* weight. Columns 7 and 8 are obtained with the DIR calibration (see Section 3.2).

Bin	z_B range	Number of objects	n_{eff} H12 (arcmin $^{-2}$)	n_{eff} C13 (arcmin $^{-2}$)	σ_e	Median(z_{DIR}) weighted	$\langle z_{\text{DIR}} \rangle$ weighted	BPZ mean $P(z)$
1	$0.1 < z_B \leq 0.3$	3879 823	2.35	1.94	0.293	0.418 ± 0.041	0.736 ± 0.036	0.495
2	$0.3 < z_B \leq 0.5$	2990 099	1.86	1.59	0.287	0.451 ± 0.012	0.574 ± 0.016	0.493
3	$0.5 < z_B \leq 0.7$	2970 570	1.83	1.52	0.279	0.659 ± 0.003	0.728 ± 0.010	0.675
4	$0.7 < z_B \leq 0.9$	2687 130	1.49	1.09	0.288	0.829 ± 0.004	0.867 ± 0.006	0.849
Total	No z_B cuts	14 640 774	8.53	6.85	0.290			

light haloes, previously unrecognized satellite tracks) are masked out.

2.3 Lensing reduction with THELI

Given the stringent requirements of weak gravitational lensing observations on the quality of the data reduction, we employ a second pipeline, THELI (Erben et al. 2005; Schirmer 2013), to reduce the KiDS-450 *r*-band data. The handling of the KiDS data with this pipeline evolved from the CARS (Erben et al. 2009) and CFHTLenS (Erben et al. 2013) projects, and is described in more detail in Kuijken et al. (2015); the key difference from the multicolour data reduction described in Section 2.2 is the preservation of the individual exposures, without the regridding or interpolation of pixels, which allows for a more accurate measurement of the sheared galaxy shapes. The major refinement for the KiDS-450 analysis over KiDS-DR1/2 concerns the astrometric calibration of the data. A cosmic shear analysis is particularly sensitive to optical camera distortions, and it is therefore essential to aim for the best possible astrometric alignment of the images. The specific improvements in the KiDS-450 data reduction are as follows:

(i) We simultaneously astrometrically calibrate *all* data from a given patch, i.e. we perform a patch-wide global astrometric calibration of the data. This allows us to take into account information from overlap areas of individual KiDS tiles.⁶

(ii) For the northern KiDS-450 patches G9, G12, and G15, we use accurate astrometric reference sources from the SDSS-Data Release 12 (Alam et al. 2015) for the absolute astrometric reference frame.

(iii) The southern patches G23 and GS do not overlap with the SDSS, and we have to use the less accurate 2MASS catalogue (see Skrutskie et al. 2006) for the absolute astrometric reference frame. However, the area of these patches is covered by the public VST ATLAS Survey (Shanks et al. 2015). ATLAS is significantly shallower than KiDS (each ATLAS pointing consists of two 45-s OmegaCAM exposures), but it covers the area with a different pointing footprint from KiDS. This allows us to constrain optical distortions better, and to compensate for the less accurate astrometric 2MASS catalogue. Our global patch-wide astrometric calibration includes *all* KiDS and ATLAS *r*-band images covering the corresponding area.

We obtain a master detection catalogue for each tile by running SExtractor (Bertin & Arnouts 1996) on the corresponding co-added THELI *r*-band image. These catalogues are the input for both the shape measurements and the multicolour photometry.

⁶ The global astrometric solution is not calculated for the nine isolated tiles that do not currently overlap with other tiles (see Fig. 1).

Masks that cover image defects, reflections, and ghosts are also created for the THELI reduction. Those are combined with the masks for the multicolour catalogues described above and applied to the galaxy catalogues. After masking and accounting for overlap between the tiles, we have a unique effective survey area of 360.3 deg 2 .

2.4 Galaxy photometry and photo-z

The KiDS-450 galaxy photometry is based on the same algorithms as were used in KiDS-DR1/2. We extract multicolour photometry for all objects in the *r*-band master catalogue from PSF-homogenized ASTRO-WISE images in the *ugri* bands.

We model the PSFs of the calibrated images in the four bands with shapelets (Refregier 2003), and calculate convolution kernels that transform the PSFs into circular Gaussians. After convolving the images, we extract the photometry using elliptical Gaussian-weighted apertures designed to maximize the precision of colour measurements while properly accounting for seeing differences. The only significant difference in the photometric analysis procedures of the KiDS-450 data with respect to those used for KiDS-DR1/2 is the adjustment of the zero-points using SLR, as mentioned in Section 2.2. The resulting improved photometric homogeneity is particularly important for the calibration of the photometric redshifts, which relies on a small number of calibration fields with deep spectroscopy (see Section 3).

For photometric redshift estimation, we use the BPZ code (Benítez 2000), as described in Hildebrandt et al. (2012). The quality of the Bayesian point estimates of the photo- z , z_B , is presented in detail in Kuijken et al. (2015, see figs 10–12 of that paper). Based on those findings, we restrict the photo- z range for the cosmic shear analysis in the range of $0.1 < z_B \leq 0.9$ to limit the outlier⁷ rates to values below 10 per cent. In order to achieve a sufficient resolution in the radial direction for the tomographic weak-lensing measurement, we subdivide this range into four equally spaced tomographic bins of width $\Delta z_B = 0.2$. A finer binning is not useful, given our photo- z uncertainty, and would compromise our ability to calibrate for additive shear (see Section 2.5 and Appendix D4). Table 1 summarizes the properties of the source samples in those bins.

It should be noted that the photo- z code is merely used to provide a convenient quantity (the Bayesian redshift estimate z_B) to bin the source sample, and that in this analysis, we do not rely on the posterior redshift probability distribution functions $P(z)$ estimated by BPZ. Instead of stacking the $P(z)$ to obtain an estimate of the underlying true redshift distribution, i.e. the strategy adopted by

⁷ Outliers are defined as objects with $\left| \frac{z_{\text{spec}} - z_B}{z_{\text{spec}}} \right| > 0.15$.

CFHTLenS (see e.g. Heymans et al. 2013; Kitching et al. 2014) and the KiDS early-science papers (Sifón et al. 2015; Viola et al. 2015; Brouwer et al. 2016; van Uitert et al. 2016), we now employ spectroscopic training data to estimate the redshift distribution in the tomographic bins directly (see Section 3). The reason for this approach is that the output of BPZ (and essentially every photo- z code; see e.g. Hildebrandt et al. 2010) is biased at a level that cannot be tolerated by contemporary and especially future cosmic shear measurements (for a discussion, see Newman et al. 2015).

2.5 Shear measurements with *lensFIT*

Gravitational lensing manifests itself as small coherent distortions of background galaxies. Accurate measurements of galaxy shapes are hence fundamental to mapping the matter distribution across cosmic time and to constraining cosmological parameters. In this work, we use the *lensFIT* likelihood-based model-fitting method to estimate the shear from the shape of a galaxy (Miller et al. 2007, 2013; Kitching et al. 2008; Fenech Conti et al. 2016).

We refer the reader to the companion paper Fenech Conti et al. (2016) for a detailed description of the most recent improvements to the *lensFIT* algorithm, shown to successfully ‘self-calibrate’ against noise bias effects, as determined through the analysis of an extensive suite of image simulations. This development is a significant advance on the version of the algorithm used in previous analyses of CFHTLenS, the KiDS-DR1/2 data, and the Red Cluster Sequence Lensing Survey (RCSLenS; Hildebrandt et al. 2016). The main improvements to the *lensFIT* algorithm and to our shape-measurement analysis since Kuijken et al. (2015) are summarized as follows:

(i) All measurements of galaxy ellipticities are biased by pixel noise in the images. Measuring ellipticity involves a non-linear transformation of the pixel values, which causes a skewness of the likelihood surface and hence a bias in any single point ellipticity estimate (Melchior & Viola 2012; Refregier et al. 2012; Miller et al. 2013; Viola, Kitching & Joachimi 2014). In order to mitigate this problem for *lensFIT*, we apply a correction for noise bias, based on the actual measurements, which we refer to as ‘self-calibration’. When a galaxy is measured, a nominal model is obtained for that galaxy, whose parameters are obtained from a maximum-likelihood estimate. The idea of ‘self-calibration’ is to create a simulated noise-free test galaxy with those parameters, remeasure its shape using the same measurement pipeline, and measure the difference between the remeasured ellipticity and the known test model ellipticity. We do not add multiple noise realizations to the noise-free galaxies, as this is computationally too expensive, but we calculate the likelihood as if noise were present. It is assumed that the measured difference is an estimate of the true bias in ellipticity for that galaxy, which is then subtracted from the data measurement. This method approximately corrects for noise bias only, not for other effects such as model bias. It leaves a small residual noise bias, of significantly reduced amplitude, which we parametrize and correct for using image simulations (see Appendix D3).

(ii) The shear for a population of galaxies is computed as a weighted average of the measured ellipticities. The weight accounts both for shape-noise variance and for ellipticity measurement-noise variance, as described in Miller et al. (2013). As the measurement noise depends to some extent on the degree of correlation between the intrinsic galaxy ellipticity and the PSF distortion, the weighting introduces biases in the shear measurements. We empirically correct for this effect (see Fenech Conti et al. 2016, for further details) by quantifying how the variance of the measured mean galaxy

ellipticity depends on galaxy ellipticity, signal-to-noise ratio (S/N), and isophotal area. We then require that the distribution of the recalibrated weights is neither a strong function of observed ellipticity nor a strong function of the relative PSF–galaxy position angle. The correction is determined from the full survey split into 125 subsamples. The sample selection is based on the local PSF model ellipticity ($\epsilon_1^*, \epsilon_2^*$) and PSF model size in order to accommodate the variation in the PSF across the survey using five bins for each PSF observable.

(iii) The sampling of the likelihood surface is improved in both speed and accuracy, by first identifying the location of the maximum likelihood and then applying the adaptive sampling strategy described by Miller et al. (2013). More accurate marginalization over the galaxy size parameter is also implemented.

(iv) In surveys at the depth of CFHTLenS or KiDS, it is essential to deal with the contamination from closely neighbouring galaxies (or stars). The *lensFIT* algorithm fits only individual galaxies, masking contaminating stars or galaxies in the same postage stamp during the fitting process. The masks are generated from an image segmentation and masking algorithm, similar to that employed in SExtractor. We find that the CFHTLenS and KiDS-DR1/2 version of *lensFIT* rejected too many target galaxies that were close to a neighbour. For this analysis, a revised deblending algorithm is adopted, which results in fewer rejections and thus a higher density of measured galaxies. The distance to the nearest neighbour, known as the ‘contamination radius’, is recorded in the catalogue output so that any bias as a function of neighbour distance can be identified and potentially rectified by selecting on that measure (see Fig. D1 in Appendix D).

(v) A large set of realistic, end-to-end image simulations (including chip layout, gaps, dithers, co-addition using SWARP, and object detection using SExtractor) are created to test for and calibrate a possible residual multiplicative shear-measurement bias in *lensFIT*. These simulations are briefly described in Appendix D3 with the full details presented in Fenech Conti et al. (2016). We estimate the multiplicative shear-measurement bias m to be less than about 1 per cent with a statistical uncertainty, set by the volume of the simulation, of ~ 0.3 per cent. We further quantify the additional systematic uncertainty coming from differences between the data and the simulations and choices in the bias estimation to be 1 per cent. Such a low bias represents a factor of 4 improvement over previous *lensFIT* measurements (e.g. CFHTLenS) that did not benefit from the ‘self-calibration’. As shown in Fig. A2 of Appendix A, this level of precision on the estimate of m is necessary not to compromise on the statistical power of the shear catalogue for cosmology.

(vi) We implement a blinding scheme designed to prevent or at least suppress confirmation bias in the cosmology analysis, along similar lines to what was done in KiDS-DR1/2. The catalogues used for the analysis contain three sets of shear and weight values: the actual measurements, as well as two fake versions. The fake data contain perturbed shear and weight values that are derived from the true measurements through parametrized smooth functions designed to prevent easy identification of the true data set. The parameters of these functions as well as the labelling of the three sets are determined randomly using a secret key that is known only to an external ‘blinder’, Matthias Bartelmann. The amplitude of the changes is tuned to ensure that the best-fitting S_8 values for the three data sets differ by at least the 1σ error on the *Planck* measurement. All computations are run on the three sets of shears and weights, and the lead authors add a second layer of blinding (i.e. randomly shuffling the three columns again for each particular science project) to allow for phased unblinding within the consortium.

In this way, co-authors can remain blind because only the second layer is unblinded for them. Which one of the three shear data sets in the catalogues is the truth is only revealed to the lead authors once the analysis is complete.

In Appendix D1, we detail the object selection criteria that are applied to clean the resulting *lensFIT* shear catalogue. The final catalogue provides shear measurements for close to 15 million galaxies, with an effective number density of $n_{\text{eff}} = 8.53 \text{ galaxies arcmin}^{-2}$ over a total effective area of 360.3 deg^2 . The inverse shear variance per unit area of the KiDS-450 data, $\hat{w} = \sum w_i / A$, is 105 arcmin^{-2} . We use the effective number density n_{eff} as defined in Heymans et al. (2012) as this estimate can be used to directly populate numerical simulations to create an unweighted mock galaxy catalogue, and it is also used in the creation of the analytical covariance (Section 5.3). We note that this value represents an ~ 30 per cent increase in the effective number density over the previous KiDS DR1/2 shear catalogue. This increase is primarily due to the improved *lensFIT* masking algorithm. Table 1 lists the effective number density for each of the four tomographic bins used in this analysis and the corresponding weighted ellipticity variance. For completeness, we also quote the number densities according to the definition by Chang et al. (2013).

3 CALIBRATION OF PHOTOMETRIC REDSHIFTS

The cosmic shear signal depends sensitively on the redshifts of all sources used in a measurement. Any cosmological interpretation requires a very accurate calibration of the photometric redshifts that are used for calculating the model predictions (Huterer et al. 2006; Van Waerbeke et al. 2006). The requirements for a survey like KiDS are already quite demanding if the systematic error in the photo- z is not to dominate over the statistical errors. For example, as detailed in Appendix A, even a Gaussian 1σ uncertainty on the measured mean redshift of each tomographic bin of $0.05(1+z)$ can degrade the statistical errors on relevant cosmological parameters by ~ 25 per cent. While such analytic estimates based on Gaussian redshift errors are a useful guideline, photometric redshift distributions of galaxy samples typically have highly non-Gaussian tails, further complicating the error analysis.

In order to obtain an accurate calibration and error analysis of our redshift distribution, we compare three different methods that rely on spectroscopic redshift (spec- z) training samples.

- (i) DIR: a weighted direct calibration obtained by a magnitude-space reweighting (Lima et al. 2008) of spectroscopic redshift catalogues that overlap with KiDS.
- (ii) CC: an angular cross-correlation-based calibration (Newman 2008) with some of the same spectroscopic catalogues.
- (iii) BOR: a recalibration of the $P(z)$ of individual galaxies estimated by BPZ in probability space, as suggested by Bordoloi, Lilly & Amara (2010).

An important aspect of our KiDS-450 cosmological analysis is an investigation into the impact of these different photometric redshift calibration schemes on the resulting cosmological parameter constraints, as presented in Section 6.3.

3.1 Overlap with spectroscopic catalogues

KiDS overlaps with several spectroscopic surveys that can be exploited to calibrate the photo- z : in particular GAMA (Driver

Table 2. Spectroscopic samples used for KiDS photo- z calibration. The COSMOS catalogue is dominated by objects from zCOSMOS–bright and zCOSMOS–deep but also includes spec- z from several other projects. While the DIR and BOR approaches make use of the full sample, the CC approach is limited to the DEEP2 sample and the original zCOSMOS sample.

sample	Number of objects	r_{lim}	z_{spec} range
COSMOS	13 397	$r \lesssim 24.5$	$0.0 < z < 3.5$
CDFS	2290	$r \lesssim 25$	$0.0 < z < 4$
DEEP2	7401	$r \lesssim 24.5$	$0.6 < z < 1.5$

et al. 2011), SDSS (Alam et al. 2015), 2dFLenS (Blake et al. 2016), and various spectroscopic surveys in the COSMOS field (Scoville et al. 2007). Additionally, there are KiDS-like data obtained with the VST in the *Chandra Deep Field-South* (CDF-S) from the VOICE project (Vaccari et al. 2012) and in two DEEP2 (Newman et al. 2013) fields, as detailed in Appendix C1.

The different calibration techniques we apply require different properties of the spec- z catalogues. The weighted direct calibration as well as the recalibration of the $P(z)$ require a spec- z catalogue that covers the same volume in colour and magnitude space as the photometric catalogue that is being calibrated. This strongly limits the use of GAMA, 2dFLenS, and SDSS for these methods since our shear catalogue is limited at $r > 20$, whereas all three of these spectroscopic projects target only objects at brighter magnitudes.

The cross-correlation technique does not have this requirement. In principle, one can calibrate a faint photometric sample with a bright spectroscopic sample, as long as both cluster with each other. Being able to use brighter galaxies as calibrators represents one of the major advantages of the cross-correlation technique. However, for this method to work, it is still necessary for the spec- z sample to cover the full redshift range that objects in the photometric sample could potentially span, given their apparent magnitude. For our shear catalogue with $r \lesssim 25$, this means that one needs to cover redshifts all the way out to $z \sim 4$. While GAMA and SDSS could still yield cross-correlation information at low z over a wide area, those two surveys do not cover the crucial high z range where most of the uncertainty in our redshift calibration lies. Hence, we limit ourselves to the deeper surveys in order to reduce processing time and data handling. The SDSS quasi-stellar object redshift catalogue can be used out to very high z for cross-correlation techniques, but due to its low surface density, the statistical errors when cross-correlated to KiDS-450 are too large for our purposes.

In the COSMOS field, we use a non-public catalogue that was kindly provided by the zCOSMOS (Lilly et al. 2009) team and goes deeper than the latest public data release. It also includes spec- z measurements from a variety of other spectroscopic surveys in the COSMOS field, which are all used in the weighted direct calibration and the recalibration of the $P(z)$ but are not used for the calibration with cross-correlations (for the reasons behind this choice, see Section 3.3). In the CDF-S, we use a compilation of spec- z released by ESO.⁸ This inhomogeneous sample cannot be used for cross-correlation studies but is well suited for the other two approaches. The DEEP2 catalogue is based on the fourth data release (Newman et al. 2013). While DEEP2 is restricted in terms of redshift range, in comparison to zCOSMOS and CDFS, it is more complete at $z \gtrsim 1$. Thus, it adds crucial information for all three calibration techniques. Table 2 summarizes the different spec- z samples used for photo- z .

⁸ [http://www.eso.org/sci/activities/garching/projects/goods/](http://www.eso.org/sci/activities/garching/projects/goods/MasterSpectroscopy.html)

calibration. The number of objects listed refers to the number of galaxies in the spec- z catalogues for which we have photometry from KiDS-450 or the auxiliary VST imaging data described in Appendix C1. For details about the completeness of DEEP2, see Newman et al. (2013). COSMOS and CDFS, however, lack detailed information on the survey completeness.

3.2 Weighted direct calibration (DIR)

The most direct way to calibrate photo- z distributions is simply to use the distribution of spec- z for a sample of objects selected in the same way as the photometric sample of interest (e.g. a tomographic photo- z bin). While this technique requires very few assumptions, in practice spec- z catalogues are almost never a complete, representative sub-sample of contemporary shear catalogues. The other main disadvantage of this method is that typical deep spec- z surveys cover less area than the photometric surveys they are supposed to calibrate, such that sample variance becomes a concern.

A way to alleviate both problems has been suggested by Lima et al. (2008). Using a k -nearest-neighbour search, the volume density of objects in multidimensional magnitude space is estimated in both the photometric and spectroscopic catalogues. These estimates can then be used to upweight spec- z objects in regions of magnitude space where the spec- z are underrepresented and to downweight them where they are overrepresented. It is clear that this method will be successful only if the spec- z catalogue spans the whole volume in magnitude space that is occupied by the photo- z catalogue and samples this colour space densely enough. Another requirement is that the dimensionality of the magnitude space is high enough to allow a unique matching between colour and redshift. These two requirements certainly also imply that the spec- z sample covers the whole redshift range of the photometric sample. A first application of this method to a cosmic shear measurement is presented in Bonnett et al. (2016).

Since the spectroscopic selection function is essentially removed by the reweighting process, we can use any object with good magnitude estimates as well as a secure redshift measurement. Thus, we employ the full spec- z sample described in Section 3.1 for this method.

When estimating the volume density in magnitude space of the photometric sample, we incorporate the *lensfit* weight into the estimate. Note that we use the full distribution of *lensfit* weights in the *unblinded* photometric catalogue for this. Weights are different for the different blinding, but we separate the data flows for calibration and further catalogue processing to prevent accidental unblinding. By incorporating the *lensfit* weight, we naturally account for the weighting of the shear catalogue without analysing the VST imaging of the spec- z fields with the *lensfit* shear measurement algorithm. This yields a more representative and robust estimate of the weighted redshift distribution.

Special care has to be taken for objects that are not detected in all four bands. Those occur in the photometric as well as in the spectroscopic sample but in different relative abundances. We treat these objects as separate classes essentially reducing the dimensionality of the magnitude space for each class and reweighting those separately. After reweighting, the classes are properly combined taking their relative abundances in the photometric and spectroscopic catalogue into account. Errors are estimated from 1000 bootstrap samples drawn from the full spec- z training catalogue. These bootstrap errors include shot noise but do not correct for residual effects of sample variance, which can still play a role because of the discrete sampling of magnitude space by the spec- z sample. Note though that

sample variance is strongly suppressed by the reweighting scheme compared to an unweighted spec- z calibration since the density in magnitude space is adjusted to the cosmic (or rather KiDS-450) average. A discussion of the influence of sample variance in the DIR redshift calibration can be found in Appendix C3.1.

A comparison of the resulting redshift distributions of the weighted direct calibration and the stacked $P(z)$ from BPZ (see Section 2.4) for the four tomographic bins is shown in Fig. 2 (blue line with confidence regions). Note that especially the $n(z)$ in the first tomographic bin is strongly affected by the $r > 20$ cut introduced by *lensfit*, which skews the distribution to higher redshifts and increases the relative amplitude of the high- z tail compared to the low- z bump. This is also reflected in the large difference between the mean and median redshifts of this bin given in Table 1. In Appendix C3.1, we discuss and test the assumptions and parameter choices made for this method. Note that we determine the redshift distributions up to the highest spectroscopic redshifts of $z \sim 4$ but only plot the range $0 < z < 2$ in Fig. 2. There are no significant $z > 2$ bumps in the DIR redshift distribution for these four tomographic bins.

3.3 Calibration with cross-correlations (CC)

The use of angular cross-correlation functions between photometric and spectroscopic galaxy samples for reconstructing photometric redshift distributions was described in detail by Newman (2008). This approach has the great advantage of being rather insensitive to the spectroscopic selection function in terms of magnitude, galaxy type, etc., as long as it spans the full redshift range of interest. However, angular autocorrelation function measurements of the spectroscopic as well as the photometric samples are needed, to measure and correct for the – typically unknown – galaxy bias. In order to estimate these autocorrelations, precise knowledge of the angular selection function (i.e. the weighted footprint) of the samples is required.

For the photometric catalogues, the angular selection functions can be estimated from the masks mentioned in Section 2.2. We do not correct for depth and seeing variations, as described in Morrison & Hildebrandt (2015), since those are relatively unimportant on the small spec- z fields used here. Regarding the spectroscopic data sets, DEEP2 provide maps of the angular selection function, allowing us to calculate all correlation functions over the full 0.8 deg^2 overlap area with KiDS-like VST imaging. We do not have a similar spectroscopic selection function for COSMOS or CDF-S. Given the small size and heterogeneity of the CDFS catalogue, we cannot use it for the cross-correlation calibration; for COSMOS, we restrict ourselves to the central 0.7 deg^2 region covered very homogeneously by zCOSMOS, and we assume a constant selection function outside the masks of the KiDS data.⁹ We do not use spec- z measurements from other surveys in the COSMOS field for the cross-correlations. Both samples, DEEP2 and zCOSMOS, are analysed independently, and only at the very end of the analysis, the redshift distributions are averaged with inverse variance weighting.

We employ an advanced version of the original technique proposed by Newman (2008) and Matthews & Newman (2010), which is described in Ménard et al. (2013) and Schmidt et al. (2013). Unlike Newman (2008), who proposed using only linear scales,

⁹ Using the KiDS masks here makes sense since photometric as well as spectroscopic surveys are affected by, for example, bright stars, and typical footprints often look quite similar.

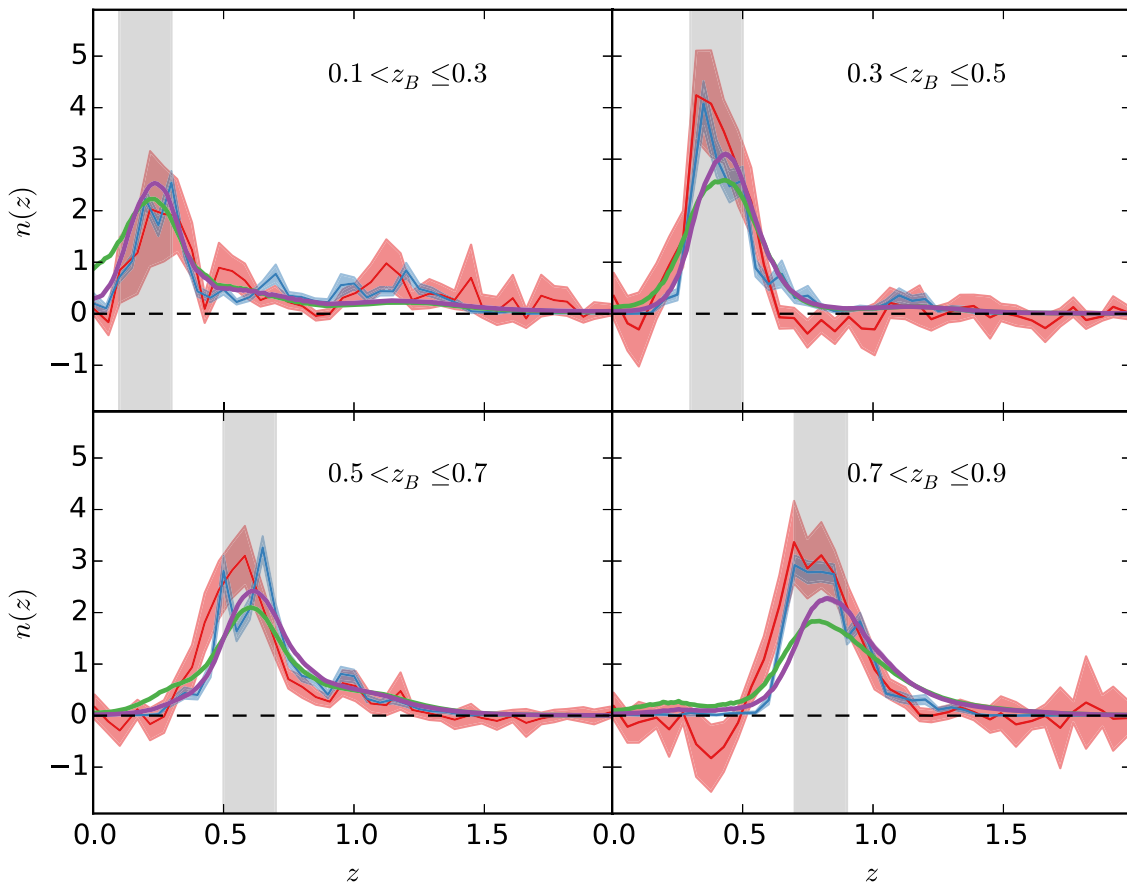


Figure 2. Comparison of the normalized redshift distributions for the four tomographic bins as estimated from the weighted direct calibration (DIR, blue with errors), the calibration with cross-correlations (CC, red with errors), the recalibrated stacked $P_{\text{recal}}(z)$ (BOR, purple with errors that are barely visible), and the original stacked $P(z)$ from BPZ (green). The grey-shaded regions indicate the target redshift range selected by cuts on the Bayesian photo- z z_B . Errors shown here do not include the effects of sample variance in the spec- z calibration sample.

Ménard et al. (2013) and Schmidt et al. (2013) advocate exploiting the much higher S/N available on smaller non-linear scales, even though this comes at the cost of more complicated galaxy bias modelling. Additionally, they describe how preselection of the photometric sample by photometric quantities can narrow down the underlying redshift distribution and make the technique less susceptible to the galaxy bias correction (see also Rahman et al. 2016).

A description of the full details and tests of our implementation of this calibration method can be found in Appendix C3.2. We summarize the steps here.

All correlation functions are estimated over a fixed range of proper separation of 30–300 kpc. The conversion of angular to proper scales requires a cosmological model. Here we assume a WMAP5 cosmology (Komatsu et al. 2009), noting that the redshift recovery is insensitive to this choice and therefore does not bias the constraints given in Section 6. The autocorrelation functions of the spec- z samples are estimated with a coarse redshift binning to allow for reliable power-law fits with small errors. We assume a linear relation between redshift and the power-law parameters r_0 and γ and fit it to the results of all the redshift bins with $0 < z_{\text{spec}} < 1.2$. For $z_{\text{spec}} > 1.2$, we fit a constant r_0 and γ .

The cross-correlation functions are estimated with a finer binning in spec- z in order to obtain redshift distributions for the tomographic bins with a high resolution. The raw cross-correlations are corrected for evolving galaxy bias with the recipe by Newman (2008) and

Matthews & Newman (2010). We estimate statistical uncertainties from a bootstrap resampling of the spectroscopic training set (1000 bootstrap samples). The whole recalibration procedure, including correlation function estimates and bias correction, is run for each bootstrap sample.

Note that the cross-correlation function can attain negative values that would lead to unphysical negative amplitudes in the $n(z)$. Nevertheless, it is important to allow for these negative values in the estimation of the cross-correlation functions so as not to introduce any bias. Such negative amplitudes can, for example, be caused by local overdensities or underdensities in the spec- z catalogue, as explained by Rahman et al. (2015). Only after the full redshift recovery process do we rebin the distributions with a coarser redshift resolution to attain positive values for $n(z)$ throughout.

The redshift distributions from this method, based on the combination of the DEEP2 and zCOSMOS results, are displayed in Fig. 2 (red line with confidence regions). Note that the uncertainties on the redshift distributions from the cross-correlation technique are larger than the uncertainties on the weighted direct calibration, owing to the relatively small area of sky covered by the spec- z catalogues. As will be shown in Section 6, propagating the $n(z)$ and associated errors from the CC method into the cosmological analysis yields cosmological parameters that are consistent with the ones that are obtained when using the DIR redshift distributions, despite some differences in the details of the redshift distributions.

3.4 Recalibration of the photometric $P(z)$ (BOR)

Many photo- z codes estimate a full redshift likelihood, $\mathcal{L}(z)$, for each galaxy or a posterior probability distribution, $P(z)$, in the case of a Bayesian code like BPZ. Bordoloi et al. (2010) suggested to use a representative spectroscopic training sample and analyse the properties of the photometric redshift likelihoods of those galaxies.

For each spectroscopic training object, the photometric $P(z)$ is integrated from zero to z_{spec} , yielding the cumulative quantity:

$$P_{\Sigma}(z_{\text{spec}}) = \int_0^{z_{\text{spec}}} P(z') dz'. \quad (1)$$

If the $P(z)$ are a fair representation of the underlying probability density, the P_{Σ} for the full training sample should be uniformly distributed between zero and 1. If this distribution $N(P_{\Sigma})$ is not flat, its shape can be used to recalibrate the original $P(z)$, as explained in Bordoloi et al. (2010).

One requirement for this approach to work is that the training sample is completely representative of the photometric sample to be calibrated. Since this is not the case for KiDS-450, we employ this recalibration technique in combination with the reweighting procedure in magnitude space, as described in Section 3.2. Some tests on the performance of this method are described in Appendix C3.3.

We make use of the full spec- z sample, similar to the weighted direct calibration mentioned above. The resulting recalibrated, stacked $P_{\text{recal}}(z)$ are also included in Fig. 2 (purple lines). Errors are estimated from 1000 bootstrap samples. The recalibration changes very little between the bootstrap samples, which is reflected in the comparably small errors on the purple lines. This is due to the fact that the BOR method uses the $P(z)$ output from BPZ directly, whereas the DIR and CC methods are completely ignorant about this information.

3.5 Discussion

The four sets of redshift distributions from the different techniques displayed in Fig. 2 show some differences, most prominently in the first and fourth tomographic bins. While most of these differences are not very significant within the errors,¹⁰ it is clear that the resulting theoretical model will differ depending on which set is chosen. This is particularly true for the first redshift bin, where the redshift distribution obtained with the stacked $P(z)$ from BPZ is quite different from the recalibrated distributions obtained by DIR and CC. This is also reflected in the different mean redshifts in this bin for DIR and BPZ reported in Table 1. Due to the more pronounced high- z tail in the DIR (and CC) distributions, the mean redshift in this first bin is actually higher than the mean redshift in the second and third bins in contrast to what is found for BPZ. The fact that both, DIR and CC, independently recover this high- z tail with a similar amplitude makes us confident that it is real. As discussed in Section 6, this has profound consequences for the best-fitting intrinsic alignment amplitude, A_{IA} . Apart from these differences, it is encouraging to see that some of the features that are not present in the stacked BPZ $P(z)$ are recovered by all three recalibration techniques, e.g. the much lower amplitude for DIR, CC, and BOR compared to BPZ at a very low redshift in the first tomographic bin.

Applying the calibrations determined from a few deep spectroscopic fields to the full survey requires a consistent photometric calibration. As briefly mentioned above (Section 2.2) and described

in more detail in Appendix B, we rely on SLR to achieve homogeneous photometry over the full survey area.

4 COSMOLOGICAL ANALYSIS

4.1 Shear two-point correlation functions

In this analysis, we measure the tomographic angular two-point shear correlation function $\hat{\xi}_{\pm}^{ij}$, which can be estimated from two tomographic redshift bins i and j as

$$\hat{\xi}_{\pm}^{ij}(\theta) = \frac{\sum_{ab} w_a w_b [\epsilon_t^i(\chi_a) \epsilon_t^j(\chi_b) \pm \epsilon_x^i(\chi_a) \epsilon_x^j(\chi_b)]}{\sum_{ab} w_a w_b}. \quad (2)$$

Galaxy weights w are included when the sum is taken over pairs of galaxies with an angular separation $|\chi_a - \chi_b|$ within an interval $\Delta\theta$ around θ . The tangential and cross components of the ellipticities $\epsilon_{t,x}$ are measured with respect to the vector $\chi_a - \chi_b$ joining each pair of objects (Bartelmann & Schneider 2001). This estimator $\hat{\xi}_{\pm}$ can be related to the underlying matter power spectrum P_{δ} , via

$$\xi_{\pm}^{ij}(\theta) = \frac{1}{2\pi} \int d\ell \ell P_{\kappa}^{ij}(\ell) J_{0,4}(\ell\theta), \quad (3)$$

where $J_{0,4}(\ell\theta)$ is the zeroth-order (for ξ_+) or fourth-order (for ξ_-) Bessel function of the first kind. $P_{\kappa}(\ell)$ is the convergence power spectrum at an angular wavenumber ℓ . Using the Limber approximation, one finds

$$P_{\kappa}^{ij}(\ell) = \int_0^{\chi_H} d\chi \frac{q_i(\chi) q_j(\chi)}{[f_K(\chi)]^2} P_{\delta} \left(\frac{\ell}{f_K(\chi)}, \chi \right), \quad (4)$$

where χ is the comoving radial distance and χ_H is the horizon distance. The lensing efficiency function $q(\chi)$ is given by

$$q_i(\chi) = \frac{3H_0^2 \Omega_m}{2c^2} \frac{f_K(\chi)}{a(\chi)} \int_{\chi}^{\chi_H} d\chi' n_i(\chi') \frac{f_K(\chi' - \chi)}{f_K(\chi')}, \quad (5)$$

where $a(\chi)$ is the dimensionless scalefactor corresponding to the comoving radial distance χ , $n_i(\chi) d\chi$ is the effective number of galaxies in $d\chi$ in redshift bin i , normalized so that $\int_0^{\chi_H} n(\chi) d\chi = 1$. $f_K(\chi)$ is the comoving angular diameter distance out to the comoving radial distance χ , H_0 is the Hubble constant, and Ω_m is the matter density parameter at $z = 0$. Note that in this derivation we ignore the difference between shear and reduced shear as it is completely negligible for our analysis. For more details, see Bartelmann & Schneider (2001), and references therein.

Cosmological parameters are directly constrained from KiDS-450 measurements of the observed angular two-point shear correlation function ξ_{\pm} in Section 6. This base measurement could also be used to derive a wide range of alternative statistics. Schneider et al. (2002b) and Schneider, Eifler & Krause (2010) discuss the relationship between a number of different real-space two-point statistics. Especially the COSEBIs (Complete Orthogonal Sets of E-/B-Integrals; Schneider et al. 2010) statistic yields a very useful separation of E and B modes as well as an optimal data compression. We choose not to explore these alternatives in this analysis, however, as Kilbinger et al. (2013) showed that they provide no significant additional cosmological information over the base ξ_{\pm} measurement. The real-space measurements of ξ_{\pm} are also input data for the two Fourier-mode conversion methods to extract the power spectrum presented in Becker et al. (2016). This conversion does not result in additional cosmological information over the base ξ_{\pm} measurement, however, if the observed shear field is B-mode free.

¹⁰ Note that errors at different redshifts are correlated.

Direct power spectrum measurements that are not based on ξ_{\pm} with CFHTLenS were made by Köhlinger et al. (2016), who present a measurement of the tomographic lensing power spectra using a quadratic estimator, and Kitching et al. (2014, 2016) present a full 3D power spectrum analysis. The benefit of using these direct power spectrum estimators is a cleaner separation of Fourier modes which are blended in the ξ_{\pm} measurement. Uncertainty in modelling the high- k non-linear power spectrum can therefore be optimally resolved by directly removing these k -scales (see e.g. Kitching et al. 2014; Alsing et al. 2016). The alternative for real-space estimators is to remove small θ scales. The conclusions reached by these alternative and more conservative analyses, however, still broadly agree with those from the base ξ_{\pm} statistical analysis (Heymans et al. 2013; Joudaki et al. 2016a).

Owing to these literature results, we have chosen to limit this first cosmological analysis of KiDS-450 to the ξ_{\pm} statistic, with a series of future papers to investigate alternative statistics. In Appendix D6, we also present an E/B-mode decomposition and analysis of KiDS-450 using the $\xi_{E/B}$ statistic.

4.2 Modelling intrinsic galaxy alignments

The two-point shear correlation function estimator from equation (2) does not measure ξ_{\pm} directly but is corrupted by the following terms:

$$\langle \hat{\xi}_{\pm} \rangle = \xi_{\pm} + \xi_{\pm}^{\text{II}} + \xi_{\pm}^{\text{GI}}, \quad (6)$$

where ξ_{\pm}^{II} measures correlations between the intrinsic ellipticities of neighbouring galaxies (known as ‘II’) and ξ_{\pm}^{GI} measures correlations between the intrinsic ellipticity of a foreground galaxy and the shear experienced by a background galaxy (known as ‘GI’).

We account for the bias introduced by the presence of intrinsic galaxy alignments by simultaneously modelling the cosmological and intrinsic alignment contributions to the observed correlation functions $\hat{\xi}_{\pm}$. We adopt the ‘non-linear–linear’ intrinsic alignment model developed by Hirata & Seljak (2004), Bridle & King (2007), and Joachimi et al. (2011). This model has been used in many cosmic shear analyses (Kirk, Bridle & Schneider 2010; Heymans et al. 2013; Abbott et al. 2016; Joudaki et al. 2016a) as it provides a reasonable fit to both observations and simulations of intrinsic galaxy alignments (see Joachimi et al. 2015, and references therein). In this model, the non-linear intrinsic alignment II and GI power spectra are related to the non-linear matter power spectrum as

$$\begin{aligned} P_{\text{II}}(k, z) &= F^2(z)P_{\delta}(k, z), \\ P_{\text{GI}}(k, z) &= F(z)P_{\delta}(k, z), \end{aligned} \quad (7)$$

where the redshift- and cosmology-dependent modifications to the power spectrum are given by

$$F(z) = -A_{\text{IA}}C_1\rho_{\text{crit}}\frac{\Omega_m}{D_+(z)}\left(\frac{1+z}{1+z_0}\right)^{\eta}\left(\frac{\bar{L}}{L_0}\right)^{\beta}. \quad (8)$$

Here A_{IA} is a free dimensionless amplitude parameter that multiplies the fixed normalization constant $C_1 = 5 \times 10^{-14} h^{-2} M_{\odot}^{-1} \text{Mpc}^3$, ρ_{crit} is the critical density at $z = 0$, and $D_+(z)$ is the linear growth factor normalized to unity today. The free parameters η and β allow for a redshift and luminosity dependence in the model around arbitrary pivot values z_0 and L_0 , and \bar{L} is the weighted average luminosity of the source sample. The II and GI contributions to the

observed two-point correlation function in equation (6) are related to the II and GI power spectra as

$$\xi_{\pm}^{ij}(\theta)_{\text{II,GI}} = \frac{1}{2\pi} \int d\ell \ell C_{\text{II,GI}}^{ij}(\ell) J_{0,4}(\ell\theta), \quad (9)$$

with

$$C_{\text{II}}^{ij}(\ell) = \int d\chi \frac{n_i(\chi)n_j(\chi)}{[f_K(\chi)]^2} P_{\text{II}}\left(\frac{\ell}{f_K(\chi)}, \chi\right), \quad (10)$$

$$C_{\text{GI}}^{ij}(\ell) = \int d\chi \frac{q_i(\chi)n_j(\chi) + n_i(\chi)q_j(\chi)}{[f_K(\chi)]^2} P_{\text{GI}}\left(\frac{\ell}{f_K(\chi)}, \chi\right), \quad (11)$$

where the projection takes into account the effective number of galaxies in redshift bin i , $n_i(\chi)$, and, in the case of GI correlations, the lensing efficiency $q_i(\chi)$ (see equation 5).

Late-type galaxies make up the majority of the KiDS-450 source sample, and no significant detection of intrinsic alignments for this type of galaxy exists. A luminosity-dependent alignment signal has, however, been measured in massive early-type galaxies with $\beta \approx 1.2 \pm 0.3$, with no evidence for redshift dependence (Joachimi et al. 2011; Singh, Mandelbaum & More 2015). We therefore determine the level of luminosity evolution with redshift for a sample of galaxies similar to KiDS-450 using the ‘COSMOS2015’ catalogue (Laigle et al. 2016). We select galaxies with $20 < m_r < 24$ and compute the mean luminosity in the r band for two redshift bins, $0.1 < z < 0.45$ and $0.45 < z < 0.9$. We find the higher redshift bin to be only 3 per cent more luminous, on average, than the lower redshift bin. Any luminosity dependence of the intrinsic alignment signal can therefore be safely ignored in this analysis, given the very weak luminosity evolution across the galaxy sample and the statistical power of the current data.

Joudaki et al. (2016a) present cosmological constraints from CFHTLenS, which has a similar statistical power to KiDS-450, using a range of priors for the model parameters A_{IA} , η , and β from equation (8) (see also Abbott et al. 2016, who allow A_{IA} and η to vary, keeping $\beta = 0$). Using the Deviance Information Criterion (DIC; see Section 7) to quantify the relative performance of different models, they find that a flexible two-parameter (A_{IA}, β) or three-parameter ($A_{\text{IA}}, \beta, \eta$) intrinsic alignment model, with or without informative priors, is disfavoured by the data, implying that the CFHTLenS data are insensitive to any redshift or luminosity dependence in the intrinsic alignment signal.

Taking all this information into account, we fix $\eta = 0$ and $\beta = 0$ for our mixed population of early- and late-type galaxies, and set a non-informative prior on the amplitude of the signal A_{IA} , allowing it to vary in the range of $-6 < A_{\text{IA}} < 6$.

4.3 Modelling the matter power spectrum, including baryon physics

Cosmological parameter constraints are derived from the comparison of the measured shear correlation function with theoretical models for the cosmic shear and intrinsic alignment contributions (equation 6). One drawback to working with the ξ_{\pm} real-space statistic is that the theoretical models integrate the matter power spectrum P_{δ} over a wide range of k -scales (see e.g. equation 4). As such we require an accurate model for the matter power spectrum that retains its accuracy well into the non-linear regime.

The non-linear dark matter power spectrum model of Takahashi et al. (2012) revised the ‘HALOFIT’ formalism of Smith et al. (2003).

The free parameters in the fit were constrained using a suite of N -body simulations spanning 16 different Λ CDM cosmological models. This model has been shown to be accurate to ~ 5 per cent down to $k = 10 \text{ h Mpc}^{-1}$ when compared with the wide range of N -body cosmological simulations from the ‘Coyote Universe’ (Heitmann et al. 2014). Where this model lacks flexibility, however, is when we consider the impact that baryon physics could have on the small-scale clustering of matter (van Daalen et al. 2011).

In Sembolini et al. (2011), matter power spectra from the ‘Overwhelmingly Large’ (OWLS) cosmological hydrodynamical simulations were used to quantify the biases introduced in cosmic shear analyses that neglect baryon feedback. The impact ranged from being insignificant to significant, where the most extreme case modelled the baryon feedback with a strong active galactic nucleus (AGN) component. For the smallest angular scales ($\theta \gtrsim 0.5 \text{ arcmin}$) used in this KiDS-450 cosmic shear analysis, in the AGN case the amplitude of ξ_{\pm} was found to decrease by up to 20 per cent, relative to a gravity-only model. This decrement is the result of changes in the total matter distribution by baryon physics, which can be captured by adjusting the parameters in the halo model. This provides a simple and sufficiently flexible parametrization of this effect, and we therefore favour this approach over alternatives that include polynomial models and principal component analyses of the hydrodynamical simulations (Eifler et al. 2015; Harnois-Déraps et al. 2015).

In order to model the non-linear power spectrum of dark matter and baryons, we adopt the effective halo model from Mead et al. (2015) with its accompanying software HMcode (Mead 2015). In comparison to cosmological simulations from the ‘Coyote Universe’, the HMcode dark-matter-only power spectrum has been shown to be as accurate as the Takahashi et al. (2012) model. As the model is built directly from the properties of haloes, it has the flexibility to vary the amplitude of the halo mass-concentration relation B , and also includes a ‘halo bloating’ parameter η_0 (see equations 14 and 26 in Mead et al. 2015). Allowing these two parameters to vary when fitting data from the OWLS simulations results in a model that is accurate to ~ 3 per cent down to $k = 10 \text{ h Mpc}^{-1}$ for all the feedback scenarios presented in van Daalen et al. (2011). Mead et al. (2015) show that these two parameters are degenerate, recommending the use of a single free parameter B to model the impact of baryon feedback on the matter power spectrum, fixing $\eta_0 = 1.03 - 0.11B$ in the likelihood analysis. For this reason, we call B the baryon feedback parameter in the following, noting that a pure dark matter model does not correspond to $B = 0$ but to $B = 3.13$. We choose to impose top-hat priors on the feedback parameter $2 < B < 4$ given by the range of plausible feedback scenarios from the OWLS simulations. Fig. 9 of Mead et al. (2015) illustrates how this range of B broadens the theoretical expectation of $\xi_{\pm}(\theta)$ by less than a per cent for scales with $\theta > 6 \text{ arcmin}$ for ξ_+ and $\theta > 1^\circ$ for ξ_- . We show in Section 6.5 that taking a conservative approach by excluding small angular scales from our cosmological analysis does not significantly alter our conclusions.

We refer the reader to Joudaki et al. (2016a), who show that there is no strong preference for or against including this additional degree of freedom in the model of the matter power spectrum when analysing CFHTLenS. They also show that when considering a dark-matter-only power spectrum, the cosmological parameter constraints are insensitive to which power spectrum model is chosen: either HMcode with $B = 3.13$, the best-fitting value for a dark-matter-only power spectrum, or Takahashi et al. (2012). In the analysis that follows, whenever baryons are not included in the analysis, the faster (in terms of CPU time) Takahashi et al. (2012) model is used.

Mead et al. (2016) present an extension of the effective halo model to produce accurate non-linear matter power spectra for non-zero neutrino masses. This allows for a consistent treatment of the impact of both baryon feedback and neutrinos, both of which affect the power spectrum on small scales. We use this extension to verify that our cosmological parameter constraints are insensitive to a change in the neutrino mass from a fixed $\Sigma m_\nu = 0.00 \text{ eV}$ to a fixed $\Sigma m_\nu = 0.06 \text{ eV}$, the fiducial value used, for example, by Planck Collaboration XIII (2016a). We therefore choose to fix $\Sigma m_\nu = 0.00 \text{ eV}$ in order to minimize CPU time in the likelihood analysis. Whilst we are insensitive to a small change of 0.06 eV in Σm_ν , KiDS-450 can set an upper limit on the sum of the neutrino masses, and a full cosmological parameter analysis where Σm_ν varies as a free parameter will be presented in future work (Joudaki et al., 2016b; Köhlinger et al., in preparation).

5 COVARIANCE MATRIX ESTIMATION

We fit the correlation functions ξ_+ and ξ_- at seven and six angular scales, respectively, and in four tomographic bins. With 10 possible autocorrelation and cross-correlation functions from the tomographic bins, our data vector therefore has 130 elements. We construct three different estimators of the covariance matrix to model the correlations that exist between these measurements: an analytical model, a numerical estimate from mock galaxy catalogues, and a direct measurement from the data using a Jackknife approach. There are merits and drawbacks to each estimator, which we discuss below. In the cosmological analysis that follows in Section 6, we use the analytical covariance matrix as the default.

We neglect the dependence of the covariance matrix on cosmological parameters. According to Eifler, Schneider & Hartlap (2009) and Kilbinger et al. (2013), this is not expected to impact our conclusions as the cosmological parameter constraints from KiDS-450 data are consistent with the ‘WMAP9’ cosmology adopted for both our numerical and analytical approaches, with $\Omega_m = 0.2905$, $\Omega_\Lambda = 0.7095$, $\Omega_b = 0.0473$, $h = 0.6898$, $\sigma_8 = 0.826$, and $n_s = 0.969$ (Hinshaw et al. 2013).

5.1 Jackknife covariance matrix

The Jackknife approach to determine a covariance matrix is completely empirical and does not require any assumptions of a fiducial background cosmology (see e.g. Heymans et al. 2005; Friedrich et al. 2016). We measure $N_{JK} = 454$ Jackknife sample estimates of ξ_{\pm} by removing a single KiDS-450 tile in turn. We then construct a Jackknife covariance estimate from the variance between the partial estimates (Wall & Jenkins 2012). The main drawbacks of the Jackknife approach are the high levels of noise in the measurement of the covariance, which results in a biased inversion of the matrix, the bias that results from measuring the covariance between correlated samples, and the fact that the Jackknife estimate is only valid when the removed sub-samples are representative of the data set (see e.g. Zehavi et al. 2002). We therefore trust only our Jackknife estimate for angular scales less than half the extent of the excised Jackknife region, which in our analysis extends to 1° . With the patchwork layout of KiDS-450 (see Fig. 1), larger Jackknife regions are currently impractical, such that we only use the Jackknife estimate to verify the numerical and analytical estimators on scales $\theta < 30 \text{ arcmin}$.

5.2 Numerical covariance matrix

The standard approach to computing the covariance matrix employs a set of mock catalogues created from a large suite of N -body simulations. With a sufficiently high number of independent simulations, the impact of noise on the measurement can be minimized and any bias in the inversion can be corrected to good accuracy (Hartlap, Simon & Schneider 2007; Taylor & Joachimi 2014; Sellentin & Heavens 2016). The main benefit of this approach is that small-scale masks and observational effects can readily be applied and accounted for with the mock catalogue. The major drawback of this approach is that variations in the matter distribution that are larger than the simulation box are absent from the mock catalogues. As small-scale modes couple to these large-scale modes (known as ‘super-sample covariance’ or SSC), numerical methods tend to underestimate the covariance, particularly on large scales where sample variance dominates. This could be compensated for by simply using larger-box simulations, but for a fixed number of particles, the resulting lack of resolution then results in a reduction of power on small scales. This dilemma accounts for the main drawback of using mocks, which we address by taking an alternative analytical approach that includes the SSC contribution to the total covariance in Section 5.3.

Our methodology to construct a numerical covariance matrix follows that described in Heymans et al. (2013), which we briefly outline here. We produce mock galaxy catalogues using 930 simulations from the SLICS (Scinet LLight Cone Simulation) project (Harnois-Déraps et al. 2015). Each simulation follows the non-linear evolution of 1536^3 particles within a box of size $505 h^{-1}$ Mpc. The density field is output at 18 redshift snapshots in the range of $0 < z < 3$. The gravitational lensing shear and convergence are computed at these lens planes, and a survey cone spanning 60 deg^2 with a pixel resolution of 4.6 arcsec is constructed. In contrast to previous analyses, we have a sufficient number of simulations such that we do not need to divide boxes into sub-realizations to increase the number of mocks.

We construct mock catalogues for the four tomographic bins by Monte Carlo (MC) sampling sources from the density field to match the mean DIR redshift distribution and effective number density in each bin, from the values listed in Table 1. Since this $n(z)$ already includes the *lensFIT* weights, each mock source is assigned a weight $w_i = 1$. We assign two-component gravitational shears to each source by linearly interpolating the mock shear fields, and apply shape noise components drawn from a Gaussian distribution determined in each bin from the weighted ellipticity variance of the data (see Table 1). We apply representative small-scale masks to each realization using a fixed mask pattern drawn from a section of the real data. We hence produce 930 mock shear catalogues matching the properties of the KiDS-450 survey, each covering 60 deg^2 .

We measure the cosmic shear statistics in the mock catalogue using an identical setup to the measurement of the data. We derive the covariance through area-scaling of the effective area of the mock to match that of the effective area of the KiDS-450 data set, accounting for regions lost through masking. Area-scaling correctly determines the total shape noise contribution to the covariance. It is only approximate, however, when scaling the cosmological Gaussian and non-Gaussian terms. We use a lognormal approximation (Hilbert, Hartlap & Schneider 2011) to estimate the error introduced by area-scaling the mock covariance. We calculate that for the typical area of each KiDS patch ($\sim 100 \text{ deg}^2$) relative to the area of each mock catalogue (60 deg^2), area-scaling introduces less than a

10 per cent error on the amplitude of the cosmological contributions to the covariance.

5.3 Analytical covariance matrix

Our favoured approach to computing the correlation function covariance employs an analytical model. The model is composed of three terms:

- (i) a disconnected part that includes the Gaussian contribution to sample variance, shape noise, as well as a mixed noise-sample variance term;
- (ii) a non-Gaussian contribution from in-survey modes that originates from the connected trispectrum of matter; and
- (iii) a contribution due to the coupling of in-survey and super-survey modes.

This approach is an advance over the numerical or Jackknife approach as it does not suffer from the effects of noise, no area-scaling is required, and the model readily accounts for the coupling with modes larger than the simulation box. It does, however, require approximations to model higher order correlations, survey geometry, and pixel-level effects.

The first Gaussian term is calculated from the formula presented in Joachimi, Schneider & Eifler (2008), using the effective survey area (to account for the loss of area due to masking), the effective galaxy number density per redshift bin (to account for the impact of the *lensFIT* weights), and the weighted intrinsic ellipticity dispersion per redshift bin (see Table 1). The underlying matter power spectrum is calculated assuming the same cosmology as the SLICS N -body simulations, using the transfer function by Eisenstein & Hu (1998) and the non-linear corrections by Takahashi et al. (2012). Convergence power spectra are then derived by a line-of-sight integration over the DIR redshift distribution from Section 3.2.

To calculate the second, non-Gaussian ‘in-survey’ contribution, we closely follow the formalism of Takada & Hu (2013). The resulting convergence power spectrum covariance is transformed into that of the correlation functions via the relations laid out in Kaiser (1992). The connected trispectrum underlying this term is calculated via the halo model, using the halo mass function and halo bias of Tinker et al. (2010). We assume a Navarro, Frenk & White (1996) halo profile with the concentration–mass relation by Duffy et al. (2008) and employ the analytical form of its Fourier transform by Scoccimarro et al. (2001). The matter power spectra and line-of-sight integrations are performed in the same manner as for the Gaussian contribution. We do not account explicitly for the survey footprint in the in-survey covariance contributions. This will lead to a slight overestimation of the covariance of ξ_+ on large scales (Sato et al. 2011).

The final SSC term was modelled by Takada & Hu (2013) as the response of the matter power spectrum to a background density composed of modes larger than the survey footprint. This response can again be expressed in terms of the halo model. It comprises contributions sometimes referred to as halo sample variance and beat coupling, plus a dilation term identified by Li, Hu & Takada (2014). The coupling of super-survey modes into the survey is caused by the finite survey footprint, which therefore needs to be modelled accurately. We account for this by creating an $N_{\text{side}} = 1024$ pixel HEALPix map (Górski et al. 2005) of the current full KiDS survey footprint and convert the part of the formalism by Takada & Hu (2013) pertaining to survey geometry into spherical harmonics. We refer the reader to Joachimi et al. (in preparation) for a detailed description of our analytical model.

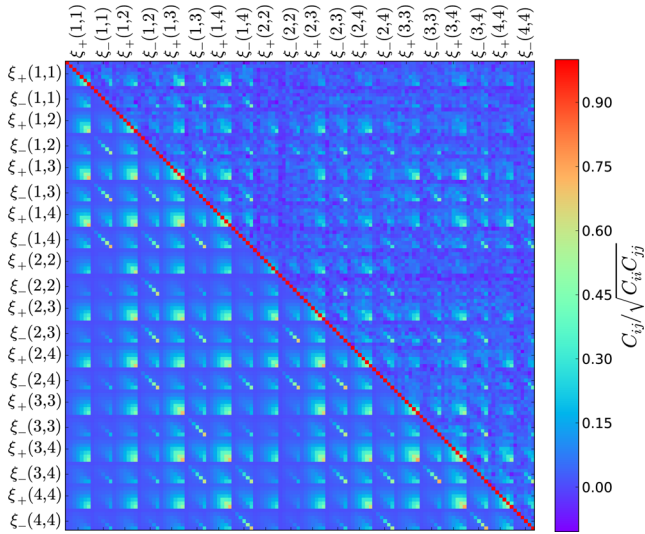


Figure 3. Comparison between the analytical correlation matrix (lower triangle) and the numerical correlation matrix (upper triangle). We order the ξ_{\pm} values in the data vector by redshift bins (m, n) as labelled, with the seven angular bins of ξ_+ followed by the six angular bins of ξ_- . In this figure, the covariance C_{ij} is normalized by the diagonal $\sqrt{C_{ii}C_{jj}}$ to display the correlation matrix.

5.4 Comparison of covariance estimators

In Fig. 3, we compare the correlation matrix of ξ_{\pm}^{ij} estimated using the analytical approach (lower triangle) with that estimated using the numerical approach (upper triangle) on the scales chosen for this analysis (see Section 6). We see a broad agreement between the two approaches that the ξ_+ statistic is highly correlated across angular scales and redshift bins, and that the correlation is less pronounced for the ξ_- statistic. The most striking result from this visual comparison, however, is that, even though we have 930 mock simulations, the noise on the numerical result is very pronounced. As shown in Section 6.4, the differences highlighted by Fig. 3, on a point-by-point basis, do not, however, significantly change our cosmological parameter constraints. These differences will be explored further in Joachimi et al. (in preparation).

Fig. 4 provides a quantitative comparison between the three covariance estimates, focusing on the ‘diagonal’ components and showing the S/N. For a representative sample of 6 out of the 10 different tomographic bin combinations, we show the expected S/N across the angular scales used in our analysis. The signal is taken from a theoretical model using the same cosmology as the SLICS simulations and the error is taken from the analytical (solid), numerical (dotted), and Jackknife (dashed) estimators. We find a good agreement between the three error estimates on scales $\theta < 30$ arcmin, with the highest S/N measurement coming from ξ_+ in the cross-correlated ‘3-4’ tomographic bin. On large scales, we find that the numerical approach underestimates the variance of ξ_{\pm} , in comparison to the analytical approach. This is expected as the mock galaxy catalogues do not include SSC and are subject to finite box effects which become significant on large scales (Harnois-Déraps & van Waerbeke 2015). Note that the Jackknife errors are invalid on these scales and hence are not shown.

Based on this comparison, we conclude that the analytical method provides a reliable (and quick) recipe for obtaining a noise-free estimate of the covariance matrix that includes SSC. We therefore use it as the default in our analysis. In Section 6.4, we run an additional analysis with the numerical covariance matrix.

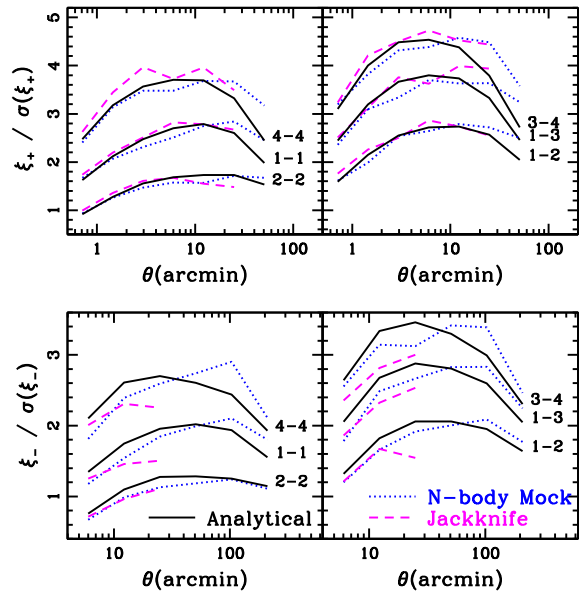


Figure 4. S/N estimates for the ξ_+ (upper panel) and ξ_- (lower panel) statistics using three different error estimates: an analytical approach (solid), N -body mock simulations (dotted), and Jackknife (dashed). A representative selection of 6 out of the 10 different tomographic bin combinations are shown with autocorrelations on the left-hand side (bins 1-1, 2-2, and 4-4) and cross-correlations shown on the right-hand side (bins 1-2, 1-3, and 3-4). There is a good agreement between the three error estimates on scales $\theta < 30$ arcmin with the highest S/N measurement coming from ξ_+ in the cross-correlated 3-4 bin. Note that the Jackknife errors are shown only for those scales for which the method is valid.

5.5 Propagation of shear calibration uncertainty

As described in Section 2.5 and Appendix D3, we apply a calibration correction factor of $(1 + m)^{-1}$ to our shear measurements. The correction is at the per cent level: In the four tomographic bins, we have $m = -0.0131, -0.0107, -0.0087$, and -0.0217 . In Appendix D3, we estimate the systematic uncertainty in m to be $\sigma_m = 0.01$. We therefore allow for an additional overall scaling of all shear values by a Gaussian random variable f of mean 1 and standard deviation $\sigma_m \ll 1$ by modifying the data covariance matrix \mathbf{C} to

$$C_{ij}^{\text{cal}} = 4\xi_i \xi_j \sigma_m^2 + C_{ij}. \quad (12)$$

[The factor 4 in the first term of equation (12) is due to the ξ_{\pm} scaling with f^2 , which has standard deviation $\sim 2\sigma_m$.]

We use the data to determine the additive calibration term, as described in Appendix D4, where the uncertainty on this correction is $\delta c \sim 2 \times 10^{-4}$ per tomographic bin. On the angular scales used in this analysis, the error $(\delta c)^2$ on the additive correction to ξ_+ is negligible and is therefore not included in our error budget. No additive correction is made to ξ_- .

6 RESULTS

We measure the two-point shear-correlation functions ξ_{\pm} with the public ATHENA code,¹¹ which implements the estimator from equation (2). The measured ellipticities are corrected for the multiplicative and additive biases described in Appendices D3 and D4. In order to be insensitive to residual uncertainties in the additive shear

¹¹ <http://www.cosmostat.org/software/athena/>

bias calibration, we limit our analysis to scales $\theta < 72$ arcmin for ξ_+ . The angular range for ξ_- is limited by the declination extent of the KiDS patches to $\theta < 5^\circ$. At small angular separations, the uncertainties in the model at non-linear scales as well as the low S/N lead us to impose lower limits of $\theta > 0.5$ arcmin for ξ_+ and $\theta > 4.2$ arcmin for ξ_- . Overall, we use nine logarithmically spaced bins spanning $0.5 < \theta < 300$ arcmin, of which the first seven are used for ξ_+ and the last six for ξ_- .

The resulting correlation functions for all possible combinations of the four tomographic bins are shown in Fig. 5. The errors correspond to the square root of the diagonal of the analytical covariance matrix (Section 5.3) and are highly correlated, as shown in Fig. 3. Overplotted is the best-fitting cosmic shear and intrinsic galaxy alignment model, as obtained from our primary analysis described in Section 6.2.

Besides the ξ_\pm correlation functions, we also estimate the derived quantities ξ_E and ξ_B (where the theoretical background and measurements are presented in Appendix D6). These statistics represent an approximate way to separate gradient modes (E) from curl modes (B) in the shear field. The ξ_B correlation function is often used as a null test for systematic errors. We find a small, but significant ξ_B signal at the smallest angular scales with $\theta < 4.2$ arcmin. In Section 6.5, we demonstrate that ξ_B has a negligible impact on the cosmological constraints.

Cosmic shear is the most sensitive to a degenerate combination of the cosmological parameters Ω_m and σ_8 with the amplitude of ξ_\pm roughly scaling with $S_8^{2.5}$, where $S_8 \equiv \sigma_8 \sqrt{\Omega_m / 0.3}$ (Jain & Seljak 1997). In the analysis presented in this section, we therefore concentrate on these two parameters and, in particular, their combination S_8 , by marginalizing over all other parameters within the framework of a flat Λ CDM universe. In Appendix F, we review our constraints within the full parameter space.

6.1 Parameters, priors, and information criterion

In order to arrive at meaningful cosmological constraints and to avoid non-physical solutions, we include top-hat priors on several cosmological parameters as well as the parameters that model the astrophysical systematic errors, the amplitude of the intrinsic alignment signal, A_{IA} , and the baryon feedback parameter B . We summarize the priors in Table 3. In several cases, we expect these to be informative (and this is borne out by the analysis), but the choice is justified because the majority of these parameters are poorly constrained by current weak-lensing surveys, with the notable exception of S_8 . We refer the reader to Joudaki et al. (2016a) for a detailed analysis of how the choice of prior impacts upon the resulting parameter constraints, showing that using progressively more informative priors on h , n_s , and A_s truncates the extremes of the $\sigma_8-\Omega_m$ degeneracy, but does not alter constraints on S_8 . When comparing different weak-lensing surveys, analysed using different priors, one should therefore be careful not to emphasize differences between the tails of the σ_8 and Ω_m distributions, which could be artificially truncated by the choice of prior.

In this analysis, we are interested in using KiDS-450 to explore the reported tension in cosmological parameter constraints between CFHTLenS and *Planck*. We therefore ensure that any informative priors that we use are motivated by non-CMB cosmological probes. For our prior on h , we use distance-ladder constraints from Riess et al. (2016), who find $h = 0.730 \pm 0.018$. We choose to adopt a top-hat prior with a conservative width $\pm 5\sigma$ such that $0.64 < h < 0.82$. This prior is also consistent with the values of h preferred by Planck Collaboration XIII (2016a), who find $h = 0.673 \pm 0.007$. Note that

h is completely degenerate with θ_{MC} . The CosmoMC code used here and described in Section 6.2 samples in θ_{MC} for technical reasons, and hence, h is a derived parameter in our analysis. However, we choose the θ_{MC} prior to be so wide as to be effectively irrelevant and add in any prior information through h . This is necessary as non-CMB analyses usually report constraints in terms of h instead of θ_{MC} .

For our top-hat prior on $\Omega_b h^2$, we use big bang nucleosynthesis constraints from Olive et al. (2014), again adopting a conservative width of $\pm 5\sigma$ such that $0.019 < \Omega_b h^2 < 0.026$. Our other prior choices are broad.

The best-fitting effective χ^2 is defined as $\chi_{\text{eff}}^2(\hat{\theta}) = -2 \ln \mathcal{L}_{\max}$, where $\hat{\theta}$ is the vector of the model parameters that yields the maximum likelihood \mathcal{L}_{\max} . For purposes of model selection, we use the DIC (Spiegelhalter et al. 2002, also see Joudaki et al. 2016a for further details):

$$\text{DIC} \equiv \overline{\chi_{\text{eff}}^2(\theta)} + 2p_D, \quad (13)$$

where $p_D = \overline{\chi_{\text{eff}}^2(\theta)} - \overline{\chi_{\text{eff}}^2(\hat{\theta})}$ is the Bayesian complexity, which acts to penalize more complex models, where $\overline{\chi_{\text{eff}}^2(\theta)}$ represents χ^2 averaged over the posterior distribution. The difference in DIC values between two competing models is computationally less expensive to calculate than the Bayes factor (e.g. Trotta 2008), an alternative measure given by the evidence ratio of the two models. Furthermore, calculating the evidence is non-trivial due to our particular approach for propagating the photometric redshift uncertainties into the analysis. We take a DIC difference between two models in excess of 10 to constitute a strong preference in favour of the model with the lower DIC (corresponding to odds of 1 in 148 for two models with the same complexity).

6.2 Cosmological parameter constraints

We obtain cosmological parameter estimates from a Bayesian likelihood analysis using the CosmoMC software, including CAMB (Lewis, Challinor & Lasenby 2000; Lewis & Bridle 2002). Our extended version uses a halo model recipe based on HMcode (Mead et al. 2015) to calculate the effect of baryons on the total matter power spectrum and closely follows the Joudaki et al. (2016a) re-analysis of the CFHTLenS data, with the exception of the handling of photo-z errors. Our primary KiDS-450 analysis includes the full modelling for intrinsic galaxy alignments (see Section 4.2) and baryon feedback (see Section 4.3), the weighted direct calibration (DIR) of the photometric redshift distribution with an error estimate (see Section 3.2), and the analytic estimate of the covariance matrix (see Section 5.3). Fig. 6 shows the confidence contours of the cosmologically most relevant parameters constrained, Ω_m and σ_8 (and their combination S_8), in comparison to the CFHTLenS results, as well as pre-*Planck* CMB measurements (Calabrese et al. 2013), and *Planck* (Planck Collaboration XIII 2016a). Note that the CFHTLenS constraints use a somewhat more informative prior on A_s , which artificially decreases the extent of the confidence contours along the degeneracy direction in comparison to the KiDS-450 constraints. The measurements for S_8 and the comparison to CMB measurements are, however, unaffected by this informative prior. The confidence contours for all pairwise combinations of the model parameters are presented in Fig. F1.

While the two lensing analyses (KiDS-450, CFHTLenS) and the pre-*Planck* CMB results are consistent with each other, with overlapping 1σ contours, there is tension between the KiDS-450 and *Planck* results, similar to that found for CFHTLenS. The tension

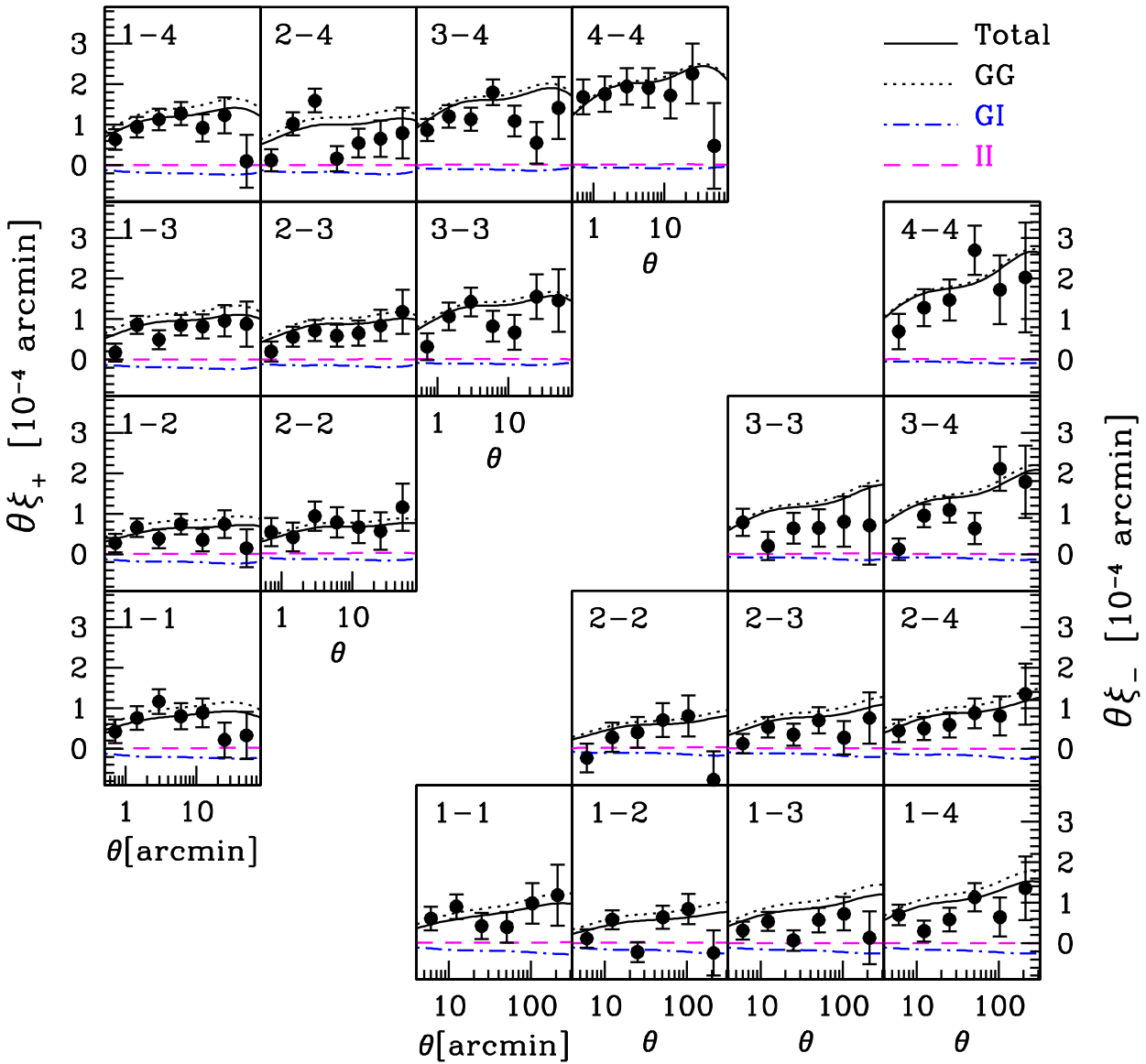


Figure 5. Tomographic measurements of ξ_+ (upper left-hand panels) and ξ_- (lower right-hand panels) from the full KiDS-450 data set. The errors shown here correspond to the diagonal of the analytical covariance matrix (Section 5.3). The theoretical model using the best-fitting cosmological parameters from Table F1 is shown (solid), which is composed of a cosmic shear term (GG, dotted) and two intrinsic alignment terms (GI, dot-dashed, and II, dashed).

Table 3. Cosmological priors on $\{\Omega_c h^2, \Omega_b h^2, \theta_{\text{MC}}, A_s, n_s, h, k_{\text{pivot}}, \Sigma m_\nu\}$ and astrophysical systematic priors on $\{A_{\text{IA}}, B\}$. θ_s denotes the angular size of the sound horizon at the redshift of last scattering and k_{pivot} corresponds to the scale where the scalar spectrum has the amplitude A_s . Note that h is closely tied to θ_{MC} , and we choose to add an informative prior on h only.

Parameter	Symbol	Prior
CDM density	$\Omega_c h^2$	[0.01, 0.99]
Baryon density	$\Omega_b h^2$	[0.019, 0.026]
100 × approximation to θ_s	$100 \theta_{\text{MC}}$	[0.5, 10]
Scalar spectrum amplitude	$\ln(10^{10} A_s)$	[1.7, 5.0]
Scalar spectral index	n_s	[0.7, 1.3]
Hubble parameter	h	[0.64, 0.82]
Pivot scale (Mpc^{-1})	k_{pivot}	0.05
Neutrino mass (eV)	Σm_ν	0.00
IA amplitude	A_{IA}	[-6, 6]
Feedback amplitude	B	[2, 4]

with respect to *Planck* is significant at the 2.3σ level. We explore concordance in the full parameter space in Section 6.9. Note that a recent reanalysis of the *Planck* data (Planck Collaboration 2016) finds slightly different values for σ_8 and Ω_m but essentially the same S_8 . Hence, the tension with respect to this KiDS-450 study is not affected.

We find that the KiDS-450 cosmic shear analysis is not particularly sensitive to the Hubble parameter so that constraints on this parameter are relatively loose and dominated by the prior employed in the analysis. The choice of the prior on h does not change the results for S_8 : A change in h moves the constraints along the curved degeneracy direction in the $\Omega_m-\sigma_8$ plane, effectively keeping S_8 and its error constant (see Fig. F2).

We chose to adopt the DIR method as our primary calibration of the redshift distributions for the four tomographic bins because arguably it gives the smallest systematic uncertainties (see Appendix C for a detailed discussion). We use bootstrap realizations to

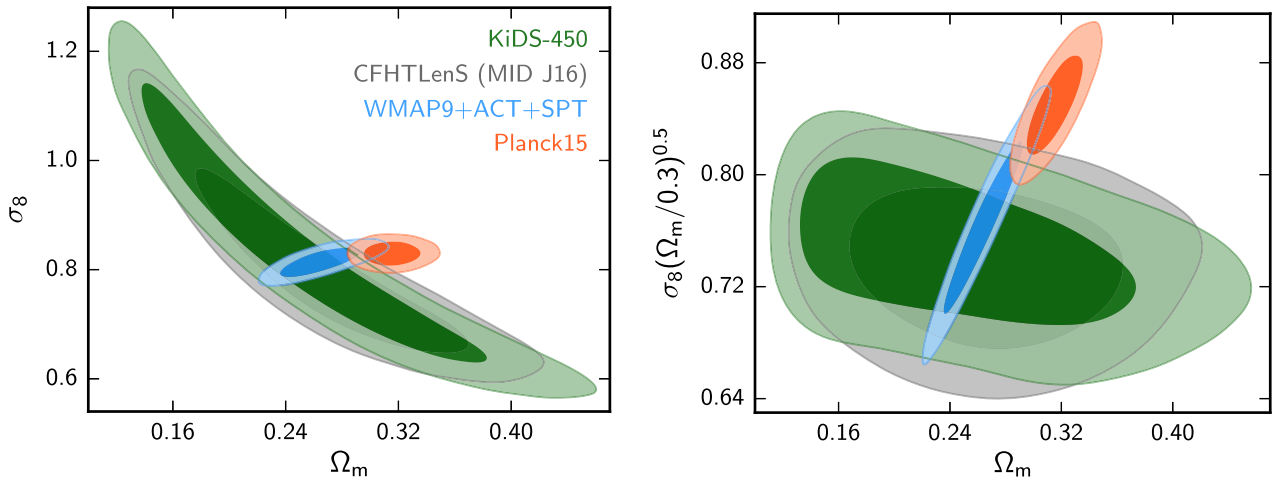


Figure 6. Marginalized posterior contours [inner 68 per cent confidence level (CL), outer 95 per cent CL] in the Ω_m – σ_8 plane (left-hand panel) and Ω_m – S_8 plane (right-hand panel) from the present work (green), CFHTLenS (grey), pre-*Planck* CMB measurements (blue), and *Planck* 2015 (orange). Note that the horizontal extent of the confidence contours of the lensing measurements is sensitive to the choice of the prior on the scalar spectrum amplitude A_s . The CFHTLenS results are based on a more informative prior on A_s artificially shortening the contour along the degeneracy direction.

Table 4. Setups for the different MCMC runs. The first column gives a short descriptive name to the setup, and the second and third columns refer the reader to the section and figure in which the setup is discussed. Columns 4–6 indicate which astrophysical systematics are marginalized over in each run. Columns 7 and 8 report the choices for the redshift distribution and the covariance matrix, respectively. Columns 8, 9, and 10 indicate whether the equation-of-state parameter w is varied, the KiDS results are combined with *Planck* (TT + lowP), and $2 \times \xi_B$ is subtracted from ξ_+ . The last column gives the angular scales used for ξ_+ . For ξ_- we use scales of 4.2–300 arcmin for all setups.

Setup	Section	Figure	Baryons	IA	Photo- z error	$n(z)$	Covariance	w	Combined with <i>Planck</i>	B-mode subtraction	scales ξ_+
KiDS-450	6.2	6	✓	✓	✓	DIR	Analytical	–	–	–	0'5 – 72'
DIR	6.3	7	–	✓	✓	DIR	Analytical	–	–	–	0'5 – 72'
CC	6.3	7	–	✓	✓	CC	Analytical	–	–	–	0'5 – 72'
BOR	6.3	7	–	✓	–	BOR	Analytical	–	–	–	0'5 – 72'
BPZ	6.3	7	–	✓	–	BPZ	Analytical	–	–	–	0'5 – 72'
No systematics	6.4	–	–	–	–	DIR	Analytical	–	–	–	0'5 – 72'
<i>N</i> -body	6.4	–	–	–	–	DIR	<i>N</i> -body	–	–	–	0'5 – 72'
DIR-no-error	6.5	8	–	✓	–	DIR	Analytical	–	–	–	0'5 – 72'
B mode	6.5	8	–	✓	–	DIR	Analytical	–	–	✓	0'5 – 72'
ξ_+ large scale	6.5	8	–	✓	–	DIR	Analytical	–	–	–	4'2 – 72'
wCDM	6.7	9	✓	✓	✓	DIR	Analytical	✓	–	–	0'5 – 72'
+ <i>Planck</i>	7	–	✓	✓	✓	DIR	Analytical	–	✓	–	0'5 – 72'

model the uncertainties and to capture the correlations between the different tomographic bins (we build the bootstrap sample from the spec- z catalogue and run the whole DIR process for each sample). We run $N = 750$ Monte Carlo Markov chains (MCMCs) varying the input set of tomographic redshift distributions each time by picking one bootstrap realization at a time. By combining all N chains, we accurately marginalize over our full uncertainty on the photometric redshift distribution without having to resort to modelling the photometric redshift error as an uncorrelated shift in the mean, as in Joudaki et al. (2016a) and Abbott et al. (2016). The value of $N = 750$ was determined through convergence tests on the final combined chain. We use a conservative criterion of $(R - 1) < 2 \times 10^{-2}$, where R is defined as the variance of chain means divided by the mean of chain variances (Gelman & Rubin 1992). We have verified that our results are stable to further exploration in the tails of the distribution.

In the following sections, we explore a series of restricted models that allow us to test the impact of different effects on the resulting cosmological parameters. The setups for the different analyses are

summarized in Table 4, and the results are described in Sections 6.3–6.7. A one-dimensional (1D) comparison of the constraints on the combined cosmological parameter S_8 for different setups of our KiDS-450 analysis and different external data sets can be found in Section 6.8.

6.3 Impact of photometric redshift uncertainty

In this section, we explore the sensitivity of the cosmological parameter constraints to the method with which the photometric redshift distributions are determined. We consider the three cases discussed in Section 3: the weighted direct calibration (DIR, Section 3.2), the cross-correlation analysis (CC, Section 3.3), and the recalibration of the photometric $P(z)$ (BOR, Section 3.4). We compare those three recalibrations to the uncalibrated redshift distributions that are based directly on the stacked $P(z)$ from BPZ.

We use the same model and priors as for the primary analysis in Section 6.2, with the exception of the baryon feedback amplitude, which we set to zero. As discussed in Section 6.8, this astrophysical

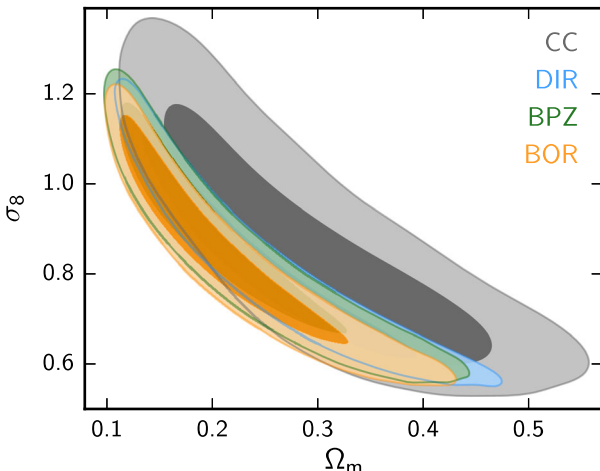


Figure 7. Marginalized posterior contours (inner 68 per cent CL, outer 95 per cent CL) in the Ω_m – σ_8 plane, examining the impact of photometric redshift uncertainty and calibration methods. Shown are the constraints in the Ω_m – σ_8 plane for the weighted direct calibration with errors (DIR, blue), the calibration with cross-correlations with errors (CC, grey), the original stacked $P(z)$ from BPZ (green), and their recalibrated version (BOR, yellow).

systematic has only a small impact on the overall result, and since for a sensitivity test we are more interested in parameter changes than in actual values, we revert to a dark-matter-only power spectrum in this comparison. This choice also enables us to switch from HM**CODE** to the faster Takahashi et al. (2012) model for the non-linear power spectrum.

For each of the three calibration methods (DIR, CC, BOR), we estimate statistical errors from a bootstrap resampling of the spectroscopic calibration sample (see Section 6.2 for details of the implementation). Including those uncertainties will broaden the contours. As can be seen in Fig. 2, these bootstrap errors are very small for the BOR method. This is due to the fact that a lot of information in that technique is based on the photometric $P(z)$ and the recalibration is more stable under bootstrap resampling of the spectroscopic calibration sample than for the other two methods. Hence, to further speed up the MCMC runs, we neglect the BOR errors in the following with no visible impact on the results. The uncertainties on the DIR method – while larger than the BOR errors – are also negligible compared to the shot noise in the shear correlation function (see Appendix C2). We nevertheless include these errors here (as before) since DIR is our primary calibration method. The statistical errors on the CC method are larger than for the two other methods, owing to the as yet small area covered by the spectroscopic surveys that we can cross-correlate with. More importantly, we estimate that the limited available area also gives rise to a larger systematic uncertainty on the CC method compared to the DIR technique. All major requirements for the DIR technique are met in this analysis, whereas the CC method will only realize its full potential when larger deep spec- z surveys become available.

The resulting confidence contours in the Ω_m – σ_8 plane for the four cases are shown in Fig. 7. All four cases give fully consistent results, although there are some shifts in the contours with respect to each other. However, with $\Delta\chi^2_{\text{eff}} \simeq -10$, we find that the DIR and CC methods provide a better fit to the data as compared to the BPZ and BOR methods. For future cosmic shear surveys, with considerably larger data sets, it will be essential to reduce the statistical uncertainty in the redshift calibration in order to not compromise the statistical power of the shear measurement. For KiDS-450, the

uncertainty for our favoured DIR calibration scheme is still sub-dominant.

In summary, we find that the four possible choices for the photometric redshift calibration technique yield consistent cosmological parameters.

6.4 Impact of analytical and numerical covariance matrices

For our primary analysis, we choose to adopt the analytical estimate of the covariance matrix described in Section 5.3, as it yields the most reliable estimate of large-scale sample variance (including super-sample contributions), is free from noise, and is broadly consistent with the N -body covariance (see Section 5.4). In this section, we compare the cosmological parameter constraints obtained with the analytical covariance matrix with the alternative numerical estimate, as described in Section 5.2. For this test, we set all astrophysical and data-related systematics to zero: this applies to the intrinsic alignment amplitude, the baryon feedback amplitude, the errors on the shear calibration, and the errors on the redshift distributions. Fixing these parameters allows us to focus on the effect of the different covariance matrices on the cosmological parameters.

We correct for noise bias in the inverse of the numerical covariance matrix estimate using the method proposed by Sellentin & Heavens (2016). As we have a significant number of N -body simulations, however, we note that the constraints derived using our numerical covariance matrix are unchanged if we use the less precise but alternative Hartlap et al. (2007) bias correction scheme.

We find consistency between the results for the different covariance matrices, given the statistical errors of KiDS-450. There is, however, a shift in the central values of the best-fitting parameters; the S_8 constraint for the numerical covariance is 0.04 lower than the constraint for the analytical covariance. This shift is equivalent to the size of the 1σ error on S_8 when all systematic effects are included in the analysis. We attribute these shifts to SSC terms that are correctly included only in the analytical estimate (which is also the reason why we adopt it as our preferred covariance). The SSC reduces the significance of the large angular ξ_{\pm} measurements (see Fig. 4) where our measured signal is rather low in comparison to the best-fitting model (see Fig. 5). The numerical covariance incorrectly gives too much weight to the large-scale results, resulting in a shift to lower S_8 values when the numerical covariance is used.

In this case, where we have neglected all systematic uncertainties, the reduced χ^2 when using the numerical covariance ($\chi^2_{\text{red}} = 1.2$) is lower than the analytic covariance analysis ($\chi^2_{\text{red}} = 1.5$). This difference can be understood from Fig. 4, where the numerical covariance predicts slightly larger errors for the angular scales which carry the most information. This is particularly true for the ξ_- statistic.

6.5 Impact of B modes

As detailed in Appendix D6, we find small but significant B modes in the KiDS-450 data on angular scales $\theta < 4.2$ arcmin. In order to assess their importance, we tested two mitigation strategies: excluding the small-scale measurements and subtracting $2 \times \xi_B$ from our ξ_+ measurements. The latter correction is valid if the origin of the systematic creates E modes with the same amplitude as the B mode. Note that ξ_- is not modified under this assumption, as explained in Appendix D6. Fig. 8 shows the effect of these two B-mode correction schemes on the constraints in the Ω_m – σ_8 plane. The contours shift somewhat when the correction is applied, and

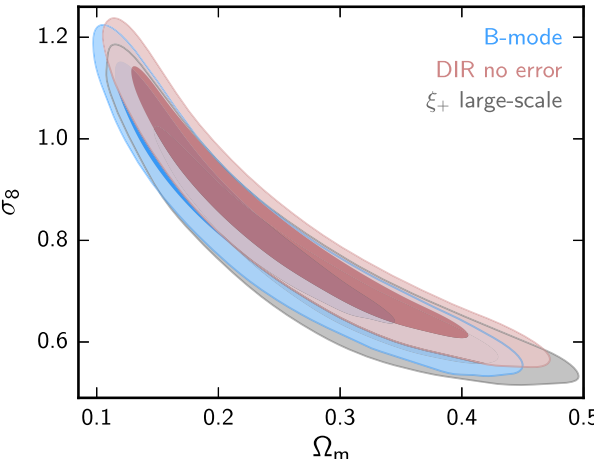


Figure 8. Marginalized posterior contours (inner 68 per cent CL, outer 95 per cent CL) in the Ω_m – σ_8 plane, examining the impact of different ways of handling the B modes. Shown are the primary constraints in the Ω_m – σ_8 plane but neglecting baryon feedback and photo- z errors (red), an analysis that subtracts $2 \times \xi_B$ from ξ_+ (B mode; blue), and an analysis that uses only large scales in ξ_+ (grey).

grow when only large scales are used, but the changes are well within the 1σ confidence region. It therefore appears that our analysis is not significantly affected by B modes: In particular, the B modes are not sufficient to explain the tension with respect to the *Planck* results. If anything, the B-mode correction increases the tension. Applying the B-mode correction does, however, result in an improvement in the goodness-of-fit, with the χ^2_{red} reducing from 1.3 to 1.1.

6.6 Impact of intrinsic galaxy alignment and baryon feedback modelling

In our primary analysis, we constrain the amplitude of the intrinsic alignments to $A_{\text{IA}} = 1.10 \pm 0.64$. This is in contrast to the different CFHTLenS analyses: From a combined analysis with *WMAP7*, Heymans et al. (2013) find an overall negative amplitude with $A_{\text{IA}} = -1.18^{+0.96}_{-1.17}$, and Joudaki et al. (2016a) find $A_{\text{IA}} = -3.6 \pm 1.6$ from lensing alone. Interestingly, if we switch from our preferred $n(z)$ (DIR, determined from the weighted direct calibration) to the stacked $P(z)$ estimated by the photo- z code BPZ (see Section 6.3), i.e. the redshift distribution methodology used for CFHTLenS, we also find a negative A_{IA} for KiDS and a considerably worse χ^2 (for details, see Appendix F and, in particular, Table F1). Since the $n(z)$ for these two different cases differ significantly in the first tomographic bin, where the relative influence of intrinsic alignments is greatest, we conclude that the BPZ distributions are particularly biased in this bin, which is properly calibrated by our now favoured DIR approach from Section 3.2. The inclusion of the IA parameter gives $\Delta\text{DIC} = -2.7$, such that it is slightly preferred by the data.

The KiDS-450 data do not strongly constrain the baryon feedback amplitude B , reflecting that this astrophysical effect is relatively unimportant for our study. Only future cosmic shear surveys with higher S/N measurements and finer binning in angle and redshift or cross-correlations between lensing and baryonic probes will allow B to be constrained to reasonable levels. Moreover, the inclusion of baryon feedback improves the DIC by only 1.0, such that it is neither favoured nor disfavoured by the data.

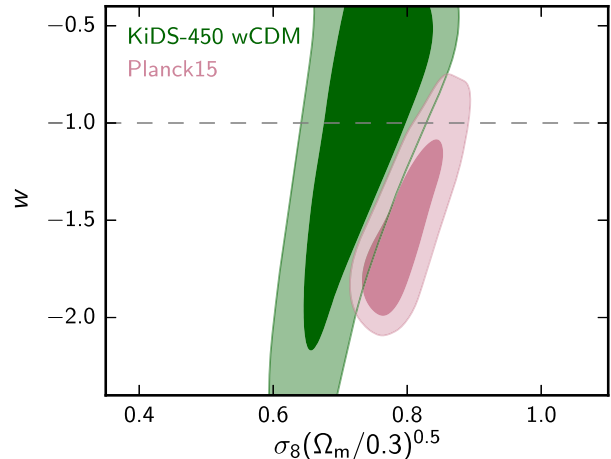


Figure 9. Marginalized posterior contours (inner 68 per cent CL, outer 95 per cent CL) in the S_8 – w plane from KiDS-450 (green) and *Planck* 2015 (pink).

6.7 wCDM cosmology

While a comprehensive analysis of KiDS-450 constraints on extensions to the standard model of cosmology is beyond the scope of this paper, we include one test of the effect of allowing the equation-of-state parameter w of the dark energy to vary. Unlike the other systematics tests described above, we allow all astrophysical parameters to vary for this test. These constraints and their dependence on Ω_m are shown in Fig. 9 in comparison to the *Planck* results.

We find that the cosmic shear result of KiDS-450 by itself is not able to yield constraints on w , as evidenced by the extended contours in Fig. 9. Within these large uncertainties on w , there is no discrepancy with previous measurements, and no indication for a deviation from a cosmological constant.

6.8 Comparison of S_8 values

In Fig. 10, we compare the constraints on S_8 for the different setups listed in Table 4 with our primary result, and also compare with measurements from the literature.

We find that the different setups yield results consistent with the primary analysis. Neglecting all systematic uncertainties shifts the S_8 value by one standard deviation and shrinks the error bars by 30 per cent. The impact of the joint inclusion of the systematic uncertainties on the central value of S_8 is small because the separate shifts partially cancel each other. The small, subdominant effect of baryon feedback can be seen by comparing the ‘KiDS-450’ setup with the ‘DIR (no baryons)’ setup. If, additionally, the photo- z errors on the weighted direct calibration are ignored, the constraints labelled ‘DIR-no-error’ are obtained. Comparing those two models hence gives an indication of the importance of the statistical error of the photo- z calibration for the total error budget. Since the S_8 errors for those two cases are almost identical, this confirms what was already found above, namely that statistical photo- z errors are subdominant in the KiDS-450 analysis.

Switching from the weighted direct calibration to the alternative $n(z)$ estimates yields consistency with the primary results, in agreement with the findings of Section 6.3. Extending the model by allowing for a free equation-of-state parameter w increases the error on S_8 by about a factor of 2. The central value is still fully consistent with the primary setup. The two different schemes for

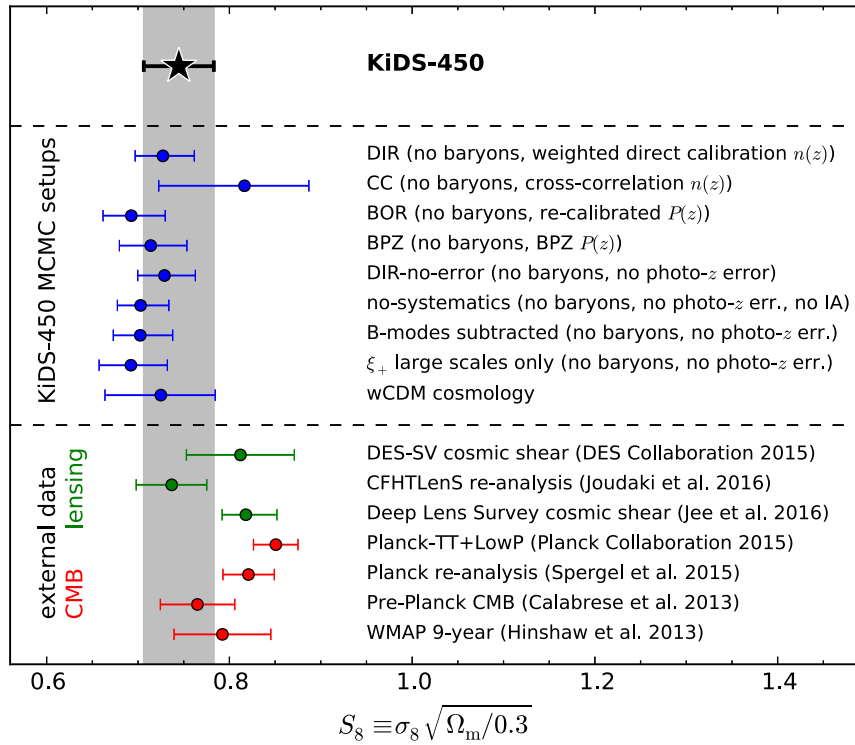


Figure 10. Constraints on S_8 for the different runs considered in the KiDS-450 analysis as well as several literature measurements. The grey band indicates the 1σ constraints from our primary analysis. Note that most of the runs which test for systematic errors (blue data points) switch off some of the astrophysical or redshift systematics. Hence, not all data points shown here are fully comparable. For numerical values of the plotted data points, see Table F1.

correcting for the B modes are consistent with the ‘no baryons, no photo- z err.’ case, as already seen in Section 6.5.

Comparing the KiDS-450 constraints with external data sets, we find consistency with the reanalysis of CFHTLenS by Joudaki et al. (2016a) and pre-*Planck* CMB constraints by Calabrese et al. (2013). The DES-SV tomographic cosmic shear constraints (Abbott et al. 2016) and the *WMAP* nine-year results (Hinshaw et al. 2013) have wider error bars that are also consistent with KiDS-450 but tend towards higher S_8 values. A mild discrepancy of $\sim 1.5\sigma$ is found with the most recent cosmic shear results from the Deep Lens Survey (Jee et al. 2016), which are based on deeper, and hence harder to calibrate, data. For a full overview of the constraints obtained from older cosmic shear measurements, see Kilbinger (2015), and references therein.

The greatest tension, at 2.3σ , is found when comparing with the 2015 *Planck* results (Planck Collaboration XIII 2016a), though the tension is diminished in the Spergel et al. (2015) reanalysis of the *Planck* data. The uncertainty on the KiDS-450 result for S_8 is about a factor of 2 larger than the uncertainty from *Planck* and almost identical to the uncertainty from the best pre-*Planck* analyses and CFHTLenS. Understanding the cause of the discordance between the latest CMB and cosmic shear data sets is an important challenge for observational cosmology.

It is interesting to compare with recent results based on alternative measurements that also constrain σ_8 and Ω_m . For instance, the number density of massive clusters of galaxies as a function of redshift is a sensitive probe of the large-scale structure growth rate. New wide-area millimetre surveys that detect large numbers of galaxy clusters with relatively well-defined selection functions through the thermal Sunyaev–Zel’dovich effect (e.g. Hasselfield

et al. 2013; Bleem et al. 2015; Planck Collaboration et al. 2016c), and improvements in the calibration of cluster masses (Applegate et al. 2014; Hoekstra et al. 2015), have resulted in constraints on cosmological parameters of comparable power to the KiDS-450 cosmic shear results. Planck Collaboration XXIV (2016b) use a sample of 439 clusters. Although the accuracy is still affected by uncertainties in the mass calibration, they report values for σ_8 that are lower than the best-fitting values from the primary CMB but agree well with our results. Similarly, de Haan et al. (2016) used 377 cluster candidates from the South Pole Telescope and found $\sigma_8 = 0.772 \pm 0.029$ (for $\Omega_m = 0.3$) in excellent agreement with our results. Similar low values for σ_8 are found in recent studies that make use of a combination of galaxy–galaxy lensing (GGL) and galaxy clustering (Cacciato et al. 2013; Mandelbaum et al. 2013; More et al. 2015). This complementary approach does not trace the matter power spectrum directly but instead measures the mass associated with galaxies as well as their linear density bias.

Measurements of redshift-space distortions, using large spectroscopic surveys, provide another interesting avenue to study the growth rate. Planck Collaboration XIII (2016a) present a compilation of constraints from redshift-space distortions as a function of redshift, again indicating a preference for lower growth rates compared to the predictions from the best-fitting Λ CDM model to the CMB. For instance, Beutler et al. (2014) use the Baryon Oscillation Spectroscopic Survey (BOSS) CMASS DR11 sample, and conversion of their results at $z_{\text{eff}} = 0.57$ implies $\sigma_8 = 0.73 \pm 0.05$, while Samushia et al. (2014) use the same data to find $\sigma_8 = 0.77 \pm 0.05$. More recent analyses of the BOSS CMASS DR12 sample (Gil-Marín et al. 2016a,b) confirm these results with tighter error bars. Generally, most redshift-space distortion results seem to be

in agreement with our measurements, even if the degree of tension with the *Planck* results varies from study to study.

6.9 Assessing concordance with *Planck*

In Section 6.8, we compare measurements of S_8 , but this does not necessarily capture the overall level of dis/concordance between *Planck* and KiDS-450. In assessing the concordance between CFHTLenS and *Planck*, Joudaki et al. (2016a) found that concordance tests grounded in the DIC (Section 6.1) and Bayesian evidence largely agreed, with the former enjoying the benefit of being more readily obtained from existing MCMC chains. We therefore follow this approach and assess the level of concordance between the two data sets D_1 and D_2 by computing

$$\mathcal{I}(D_1, D_2) \equiv \exp\{-\mathcal{G}(D_1, D_2)/2\}, \quad (14)$$

where

$$\mathcal{G}(D_1, D_2) = \text{DIC}(D_1 \cup D_2) - \text{DIC}(D_1) - \text{DIC}(D_2), \quad (15)$$

where $\text{DIC}(D_1 \cup D_2)$ is the DIC of the combined data set. Thus, $\log \mathcal{I}$ is constructed to be positive when the data sets are concordant and negative when the data sets are discordant. The significance of the concordance test follows Jeffreys' scale (Jeffreys 1961), such that $\log \mathcal{I}$ values in excess of $\pm 1/2$ are ‘substantial’, in excess of ± 1 are ‘strong’, and in excess of ± 2 are ‘decisive’.

For our primary analysis, we find that $\log \mathcal{I} = -0.79$, which translates into substantial discordance between KiDS-450 and *Planck*. This is consistent with the level of discordance inferred from the respective S_8 constraints. Note that we use only the *Planck* ‘TT + lowP’ data for these comparisons. If we included *Planck* polarization data as well (‘TT + TE + EE + lowP’), the discordance would be even more pronounced.

7 DISCUSSION

The KiDS-450 data set analysed here represents one of the most powerful cosmic shear surveys to date. Its combination of area, depth, and image quality is unprecedented, and this results in one of the most accurate and precise cosmological constraints from cosmic shear to date. In view of this precision, understanding systematic uncertainties becomes more important than in any previous such analysis. The treatment of systematic errors in the shear and photo-z measurements of KiDS-450 is based on the most advanced methods described in the literature. After accounting for residual uncertainties in these calibrations, KiDS-450 yields a constraining power on cosmological parameters similar to CFHTLenS.

The results presented in Section 6 reveal a tension between *Planck* and KiDS-450 constraints on the matter density and the normalization of the matter power spectrum. While the 2.3σ level tension in the combined parameter S_8 is similar compared with previous analyses like CFHTLenS, there is now less room for explaining this tension with photometric redshift errors that were either unaccounted for or not considered as rigorously in the past. The reduced χ^2 value of $\chi_{\text{eff}}^2/\text{dof} = 1.3$ for our primary analysis indicates that our model is a reasonable fit. Traditionally, weak-lensing analyses have focused on possible systematic errors in the shear measurements, and there are now a number of techniques that are able to achieve calibration uncertainties of the order of a per cent (see Mandelbaum et al. 2015 for a recent compilation). This level of accuracy is adequate for ground-based surveys like KiDS. Attention is therefore shifting to the other main observable, the photometric redshifts.

The calibration of the source redshift distribution remains one of the main uncertainties in the analysis. In this work, we compared three different calibration techniques and we found consistent cosmological results. Our primary method (DIR) is conceptually straightforward and statistically sufficiently powerful for present purposes but relies on available deep spectroscopic surveys that span the full range of colours and magnitudes of KiDS galaxies – something that is only beginning to be the case with current data. For the alternative galaxy clustering based method (CC), the errors on the calibration are so large that the tension with *Planck* disappears. However, we believe that this calibration technique is currently the most problematic, both in terms of statistical power and in terms of systematic errors. Hence, this apparent consistency should not be overstressed. Estimating the cross-correlations from a much larger area in the future will not only yield better statistics, but also alleviate some of the systematic problems discussed in Appendix C3.2. Interestingly, the best-fitting χ_{eff}^2 increases by ~ 10 when switching from either the DIR or CC redshift distributions to the BOR or BPZ distributions (see Table F2). This could be an indication that indeed the two recalibrated $n(z)$ (DIR, CC) are a better representation of the data compared with the two sets of stacked $P(z)$ (BOR, BPZ). All three recalibration approaches suffer from sample variance in the spec-z calibration sample due to its finite size, which we do not explicitly take into account. For KiDS-450, we estimate that this sample variance is subdominant to other sources of error on the cosmological parameters though.

We have found a small but significant B-mode signal at small angular scales. Its existence hints at some aspect of the data that is not well understood, but ironically only the statistical power of KiDS makes it possible to detect such a low-level B-mode signal. We assessed the impact of the measured B modes on our cosmological constraints by excluding the small angular scales from the analysis and by subtracting them from the E-mode signal under certain reasonable assumptions (Appendix D6). In both cases, we found no significant difference in the inferred cosmological parameters compared with our primary measurements. Given the small amplitude of the measured B modes, it seems unlikely that an improved understanding would lead to full consistency with all external data sets considered here.

It is interesting to compare our findings with several recent re-analyses of the *Planck* data and with results from earlier CMB measurements. The general picture is that those reanalyses and independent measurements are more consistent with our findings than the *Planck* 2015 results. As for whether the main systematic problems are on the side of the weak-lensing measurements or whether some aspect of the (much higher S/N) CMB measurements have to be revised remains a topic for further investigation. In order to make our results compatible with the *Planck* 2015 constraints, one would have to assume the unlikely scenario that strong systematic errors have been overlooked. In particular, one would require a multiplicative shear bias of $m \sim 0.16$ or a photo-z bias of $\Delta z \sim 0.14$, which have been left unaccounted for in this lensing analysis. These numbers are significantly larger than our estimated errors on the m correction and the DIR photo-z calibration. Even if we had underestimated these errors, the main conclusions of this paper would not significantly change. For example, adopting a three-fold increase in the error on our shear calibration correction σ_m would increase our error on S_8 only by ~ 15 per cent (see Section A4 and Fig. A2), still resulting in a $\sim 2\sigma$ tension with respect to *Planck*. A similar argument holds for the residual sample variance in the photo-z calibration.

8 SUMMARY AND OUTLOOK

In this paper, we present the first tomographic cosmic shear analysis of the KiDS using almost one-third of the final data volume ($\sim 450 \text{ deg}^2$). We make use of state-of-the-art data-analysis tools like the *THELI* pipeline for image reduction of the lensing data, the *ASTRO-WISE* system for multicolour reduction and measurements, a new self-calibrating version of *lensfit* for shear measurements, and three different photo- z calibration methods based on deep spectroscopic surveys. For the estimation of measurement errors and sample variance, we employ a redundant approach by estimating two independent covariance matrices for our data vector using an analytical and numerical approach. Our theoretical model mitigates the impact of astrophysical systematic effects related to intrinsic galaxy alignments and baryon feedback. The analysis was fully blinded with three different shear estimates in the catalogues. Unblinding occurred right before submission of this paper.

The high-level data products used in this paper are publicly available at <http://kids.strw.leidenuniv.nl/>. This release includes the shear correlation functions, the covariance matrices, redshift distributions from the weighted direct calibration and their bootstrap realizations, and the full MCMCs for the primary analysis.

Our findings are as follows:

(i) We find a best-fitting value for $S_8 \equiv \sigma_8 \sqrt{\Omega_m / 0.3} = 0.745 \pm 0.039$ assuming a flat ΛCDM model using weak external priors. The uncertainty on this parameter combination is within a factor of 2 of that derived from *Planck* alone, although constraints on σ_8 and Ω_m separately are much tighter for *Planck*. These findings are in tension with the *Planck* 2015 results at the 2.3σ level but consistent with previous cosmic shear analyses and a number of other literature measurements.

(ii) We use three different photo- z calibration methods, which yield slightly different redshift distributions. When the uncertainty in each calibration is included in the cosmological analysis, we find consistent cosmological constraints.

(iii) For our primary results, we use the photo- z calibration method which makes the fewest assumptions and hence is most likely to have the best control of systematic errors. This direct calibration technique has uncertainties that are subdominant compared to the measurement errors. As an independent cross-check, we also estimate cosmological constraints based on an alternative calibration technique that uses angular cross-correlations. The statistical uncertainties resulting from this technique dominate the error budget because of small areal coverage, resulting in weaker constraints that are, however, compatible with *Planck*, previous cosmic shear analyses, and other literature measurements. Further checks using the uncalibrated photo- z probability distributions, or a recalibrated version, give results that do not differ significantly from the primary analysis.

(iv) The multiplicative shear calibration estimated from a suite of dedicated end-to-end image simulations is of the order of 1 per cent with a statistical error of 0.3 per cent and a systematic uncertainty of 1 per cent. This calibration is a factor of 4 smaller than the one applied to the CFHTLenS shear measurements, thanks to the new self-calibrating version of *lensfit*.

(v) The additive shear calibration estimated empirically from the data by averaging galaxy ellipticities in the different KiDS patches and redshift bins is, on average, a factor of 2 smaller than the one derived for the CFHTLenS analysis. We calibrate each $\sim 100 \text{ deg}^2$ patch and each tomographic bin separately for this effect.

(vi) We use two independent covariance matrices, one estimated analytically and the other one from N -body simulations, and find

that they agree on small scales. On large scales, the N -body method underestimates the covariance due to missing SSC terms. Thus, we use the analytical estimate for the final results. This is the first time that the full SSC contribution is calculated and used in an observational cosmic shear analysis.

(vii) We measure significant but low-level shear B modes on the smallest angular scales used in our analysis. This hints at some as yet uncorrected systematic error in the data. Making reasonable assumptions about the behaviour of these B modes or restricting the analysis to large scales with $\theta \geq 4.2 \text{ arcmin}$, we show that the cosmological conclusions, in particular the tension found with *Planck*, are not affected.

(viii) We constrain the amplitude of the intrinsic alignments to $A_{IA} = 1.10 \pm 0.64$ assuming no luminosity or redshift dependence. The tension with the previously reported negative amplitude $A_{IA} = -1.18^{+0.96}_{-1.17}$ from a joint analysis of CFHTLenS with *WMAP7* (see Heymans et al. 2013) can be fully understood in terms of our improved knowledge of the true redshift distribution for low photometric redshift galaxies.

(ix) We extend our analysis to $w\text{CDM}$ models, varying the equation-of-state parameter w . We find full consistency with a cosmological constant.

Data acquisition for the KiDS is ongoing, and we will revisit this cosmic shear measurement with future data releases. The European VIKING (VISTA Kilo-Degree Infrared Galaxy; Edge et al. 2013) survey complements KiDS in five near-infrared bands. Inclusion of VIKING data will lead to better photo- z and allow us to efficiently use redshifts $z > 1$. These better photo- z will also make it possible to divide the source sample into more tomographic bins giving a better resolution along the line of sight. The redshift calibration will benefit as well since the mapping from 9D magnitude space ($ugriZYJHK_s$) to redshift is better defined, with fewer colour-redshift degeneracies than in the 4D case presented here.

As the survey grows and the statistical precision increases further, it will become crucial to obtain a better understanding of the small-scale B modes and derive a correction scheme. We are currently investigating different hypotheses, but as the presence of small-scale B modes does not impact the conclusions that we can draw from this KiDS-450 analysis, we leave a detailed investigation of the source of the B modes to a subsequent analysis.

Future progress in cosmic shear measurements will rely heavily on external data sets, in particular deep spectroscopic calibration fields. Ideally, the weighted direct calibration used here should be carried out in a redundant way by using multiple independent spectroscopic surveys from different instruments and telescopes as well as from many different lines of sight. Filling up gaps in high-dimensional magnitude space by using a technique as described in Masters et al. (2015) will greatly help to reach the full potential of cosmic shear measurements. In general, shallower and wider surveys are easier to calibrate with this technique compared with deeper, narrower surveys, which is an important constraint for future observation plans.

If the tension between cosmological probes persists in the future, despite increasingly accurate corrections for systematic errors, modification of the current concordance model will become necessary (see e.g. Riess et al. 2016). It is still too early to make the case for such extended models based on the KiDS-450 data alone, but in this cosmic shear study, we see no evidence that this

tension can be attributed to systematic errors in the weak-lensing results.

ACKNOWLEDGEMENTS

We thank Matthias Bartelmann for being our external blinder, revealing which of the three catalogues analysed was the true unblinded catalogue at the end of this study. We thank Martin Kilbinger for the ATHENA correlation function measurement software and the NICAEA theoretical modelling software, and Antony Lewis for the CAMB and COSMOMC codes. We thank members of the KiDS *i*-band eyeballing team Margot Brouwer, Marcello Cacciato, Martin Eriksen, and Cristobal Sifón, for all their ground work in road-testing the data verification checks that were subsequently used for the *r*-band analysis presented in this paper. We thank Maciek Bilicki and Marcello Cacciato for useful comments that improved the manuscript, Marika Asgari for useful discussions, Aku Venhola and Reynier Peletier, who kindly took the VST observations of the DEEP2 fields, and Peter Capak for providing additional spectroscopy of galaxies to test our direct calibration analysis in the COSMOS field. We thank Erminia Calabrese and Renee Hlozek for providing likelihood chains from the Calabrese et al. (2013) and Spergel et al. (2015) CMB analyses. We thank the zCOSMOS team for making their full, non-public redshift catalogue available for photo-*z* tests.

This work was financially supported by the DFG (Emmy Noether grants Hi 1495/2-1 and Si 1769/1-1; TR33 ‘The Dark Universe’), the BMWi (via DLR, project 50QE1103), the Alexander von Humboldt Foundation, the ERC (grants 240185, 279396, 647112, and 670193), the Seventh Framework Programme of the European Commission (Marie Skłodowska Curie Fellowship grant 656869 and People Programme grant 627288), the ERDF (project ERDF-080), the STFC (Ernest Rutherford Research Grant ST/L00285X/1 and Ernest Rutherford Fellowship ST/J004421/1), NWO (grants 614.001.103, 614.061.610, 022.003.013, and 614.001.451), NOVA, the Target program (which is supported by the Samenwerkingsverband Noord Nederland, European fund for regional development, Dutch Ministry of economic affairs, Pieken in de Delta, Provinces of Groningen and Drenthe), NSERC, CIFAR, and the ARC. We acknowledge the use of ASTAC time on Swinburne’s gSTAR and SwinSTAR computing clusters. We are grateful to the Lorentz Center for hosting our workshops.

Based on data products from observations made with ESO Telescopes at the La Silla Paranal Observatory under programme IDs 177.A-3016, 177.A-3017, and 177.A-3018, and on data products produced by Target/OmegaCEN, INAF-OACN, INAF-OAPD, and the KiDS production team, on behalf of the KiDS consortium.

Author Contributions: All authors contributed to the development and writing of this paper. The authorship list is given in three groups: the lead authors (HH, MV, CH, SJ, KK), followed by two alphabetical groups. The first alphabetical group includes those who are key contributors to both the scientific analysis and the data products. The second group covers those who have made a significant contribution either to the data products or to the scientific analysis.

REFERENCES

- Abbott T. et al., 2016, Phys. Rev. D, 94, 022001
 Addison G. E., Huang Y., Watts D. J., Bennett C. L., Halpern M., Hinshaw G., Weiland J. L., 2016, ApJ, 818, 132
 Ahn C. P. et al., 2012, ApJS, 203, 21
 Alam S. et al., 2015, ApJS, 219, 12
 Albrecht A. et al., 2006, preprint ([astro-ph/0609591](#))
 Alsing J., Heavens A., Jaffe A. H., Kiessling A., Wandelt B., Hoffmann T., 2016, MNRAS, 455, 4452
 Anderson L. et al., 2014, MNRAS, 441, 24
 Applegate D. E. et al., 2014, MNRAS, 439, 48
 Asgari M., Heymans C., Blake C., Harnois-Deraps J., Schneider P., Van Waerbeke L., 2017, MNRAS, 464, 1676
 Audren B., Lesgourgues J., Benabed K., Prunet S., 2013, J. Cosmology Astropart. Phys., 2, 001
 Bacon D. J., Massey R. J., Refregier A. R., Ellis R. S., 2003, MNRAS, 344, 673
 Bartelmann M., Schneider P., 2001, Phys. Rep., 340, 291
 Becker M. R. et al., 2016, Phys. Rev. D, 94, 022002
 Begeman K., Belikov A. N., Boxhoorn D. R., Valentijn E. A., 2013, Exp. Astron., 35, 1
 Benítez N., 2000, ApJ, 536, 571
 Benjamin J. et al., 2007, MNRAS, 381, 702
 Bertin E., 2010, Astrophysics Source Code Library, record ascl:1010.068
 Bertin E., Arnouts S., 1996, A&AS, 117, 393
 Betoule M. et al., 2014, A&A, 568, A22
 Beutler F. et al., 2014, MNRAS, 443, 1065
 Blake C. et al., 2016, MNRAS, 462, 4240
 Blas D., Lesgourgues J., Tram T., 2011, J. Cosmology Astropart. Phys., 7, 034
 Bleem L. E. et al., 2015, ApJS, 216, 27
 Bonnett C. et al., 2016, Phys. Rev. D, 94, 042005
 Bordoloi R., Lilly S. J., Amara A., 2010, MNRAS, 406, 881
 Bordoloi R. et al., 2012, MNRAS, 421, 1671
 Bridle S., King L., 2007, New J. Phys., 9, 444
 Brouwer M. M. et al., 2016, MNRAS, 462, 4451
 Bruderer C., Chang C., Refregier A., Amara A., Bergé J., Gamper L., 2016, ApJ, 817, 25
 Cacciato M., van den Bosch F. C., More S., Mo H., Yang X., 2013, MNRAS, 430, 767
 Calabrese E. et al., 2013, Phys. Rev. D, 87, 103012
 Chang C. et al., 2013, MNRAS, 434, 2121
 Choi A. et al., 2016, MNRAS, 463, 3737
 Crittenden R. G., Natarajan P., Pen U.-L., Theuns T., 2002, ApJ, 568, 20
 Cunha C. E., Huterer D., Busha M. T., Wechsler R. H., 2012, MNRAS, 423, 909
 Czekaj M. A., Robin A. C., Figueras F., Luri X., Haywood M., 2014, A&A, 564, A102
 de Haan T. et al., 2016, preprint ([arXiv:1603.06522](#))
 de Jong J. T. A. et al., 2015, A&A, 582, A62
 Driver S. P. et al., 2011, MNRAS, 413, 971
 Duffy A. R., Schaye J., Kay S. T., Dalla Vecchia C., 2008, MNRAS, 390, L64
 Duncan C. A. J., Joachimi B., Heavens A. F., Heymans C., Hildebrandt H., 2014, MNRAS, 437, 2471
 Edge A., Sutherland W., Kuijken K., Driver S., McMahon R., Eales S., Emerson J. P., 2013, The Messenger, 154, 32
 Eifler T., Schneider P., Hartlap J., 2009, A&A, 502, 721
 Eifler T., Krause E., Dodelson S., Zentner A. R., Hearin A. P., Gnedin N. Y., 2015, MNRAS, 454, 2451
 Eisenstein D. J., Hu W., 1998, ApJ, 496, 605
 Erben T. et al., 2005, Astron. Nachr., 326, 432
 Erben T. et al., 2009, A&A, 493, 1197
 Erben T. et al., 2013, MNRAS, 433, 2545
 Fenech Conti I., Herbonnet R., Hoekstra H., Merten J., Miller L., Viola M., 2016, preprint ([arXiv:1606.05337](#))
 Fields B. D., Olive K. A., 2006, Nucl. Phys. A, 777, 208
 Friedrich O., Seitz S., Eifler T. F., Gruen D., 2016, MNRAS, 456, 2662
 Fu L. et al., 2008, A&A, 479, 9
 Gelman A., Rubin D., 1992, Stat. Sci., 7, 457
 Giahi-Saravani A., Schäfer B. M., 2014, MNRAS, 437, 1847
 Gil-Marín H. et al., 2016a, MNRAS
 Gil-Marín H., Percival W. J., Verde L., Brownstein J. R., Chuang C.-H., Kitaura F.-S., Rodríguez-Torres S. A., Olmstead M. D., 2016b, preprint ([arXiv:1606.00439](#))

- Górski K. M., Hivon E., Banday A. J., Wandelt B. D., Hansen F. K., Reinecke M., Bartelmann M., 2005, *ApJ*, 622, 759
- Harnois-Déraps J., van Waerbeke L., 2015, *MNRAS*, 450, 2857
- Harnois-Déraps J., van Waerbeke L., Viola M., Heymans C., 2015, *MNRAS*, 450, 1212
- Hartlap J., Simon P., Schneider P., 2007, *A&A*, 464, 399
- Hasselfield M. et al., 2013, *J. Cosmology Astropart. Phys.*, 7, 008
- Heitmann K., Lawrence E., Kwan J., Habib S., Higdon D., 2014, *ApJ*, 780, 111
- Heymans C. et al., 2005, *MNRAS*, 361, 160
- Heymans C. et al., 2006a, *MNRAS*, 368, 1323
- Heymans C., White M., Heavens A., Vale C., van Waerbeke L., 2006b, *MNRAS*, 371, 750
- Heymans C. et al., 2012, *MNRAS*, 427, 146
- Heymans C. et al., 2013, *MNRAS*, 432, 2433
- High F. W., Stubbs C. W., Rest A., Stalder B., Challis P., 2009, *AJ*, 138, 110
- Hilbert S., Hartlap J., Schneider P., 2011, *A&A*, 536, A85
- Hildebrandt H. et al., 2010, *A&A*, 523, A31
- Hildebrandt H. et al., 2012, *MNRAS*, 421, 2355
- Hildebrandt H. et al., 2016, *MNRAS*, 463, 635
- Hinshaw G. et al., 2013, *ApJS*, 208, 19
- Hirata C., Seljak U., 2003, *MNRAS*, 343, 459
- Hirata C. M., Seljak U., 2004, *Phys. Rev. D*, 70, 063526
- Hoekstra H., 2004, *MNRAS*, 347, 1337
- Hoekstra H., Herbonnet R., Muzzin A., Babul A., Mahdavi A., Viola M., Cacciato M., 2015, *MNRAS*, 449, 685
- Hu W., 2002, *Phys. Rev. D*, 66, 083515
- Huterer D., Takada M., Bernstein G., Jain B., 2006, *MNRAS*, 366, 101
- Ivezić Ž. et al., 2004, *Astron. Nachr.*, 325, 583
- Jain B., Seljak U., 1997, *ApJ*, 484, 560
- Jain B., Taylor A., 2003, *Phys. Rev. Lett.*, 91, 141302
- Jarvis M., 2015, Astrophysics Source Code Library, record ascl:1508.007
- Jarvis M. et al., 2016, *MNRAS*, 460, 2245
- Jee M. J., Tyson J. A., Schneider M. D., Wittman D., Schmidt S., Hilbert S., 2013, *ApJ*, 765, 74
- Jee M. J., Tyson J. A., Hilbert S., Schneider M. D., Schmidt S., Wittman D., 2016, *ApJ*, 824, 77
- Jeffreys H., 1961, Theory of Probability, 3rd edn. Oxford Univ. Press, Oxford
- Joachimi B., Schneider P., Eifler T., 2008, *A&A*, 477, 43
- Joachimi B., Mandelbaum R., Abdalla F. B., Bridle S. L., 2011, *A&A*, 527, A26
- Joachimi B. et al., 2015, *Space Sci. Rev.*, 193, 1
- Joudaki S. et al., 2016a, preprint ([arXiv:1601.05786](https://arxiv.org/abs/1601.05786))
- Joudaki S. et al., 2016b, preprint ([arXiv:1610.04606](https://arxiv.org/abs/1610.04606))
- Kacprzak T., Bridle S., Rowe B., Voigt L., Zuntz J., Hirsch M., MacCrann N., 2014, *MNRAS*, 441, 2528
- Kaiser N., 1992, *ApJ*, 388, 272
- Kaiser N., 2000, *ApJ*, 537, 555
- Kazin E. A. et al., 2014, *MNRAS*, 441, 3524
- Kilbinger M., 2015, *Rep. Prog. Phys.*, 78, 086901
- Kilbinger M. et al., 2009, *A&A*, 497, 677
- Kilbinger M. et al., 2013, *MNRAS*, 430, 2200
- Kilbinger M., Bonnett C., Coupon J., 2014, Astrophysics Source Code Library, record ascl:1402.026
- Kirk D., Bridle S., Schneider M., 2010, *MNRAS*, 408, 1502
- Kitching T. D., Miller L., Heymans C. E., van Waerbeke L., Heavens A. F., 2008, *MNRAS*, 390, 149
- Kitching T. D. et al., 2014, *MNRAS*, 442, 1326
- Kitching T. D. et al., 2015, preprint ([arXiv:1512.03627](https://arxiv.org/abs/1512.03627))
- Kitching T. D., Verde L., Heavens A. F., Jimenez R., 2016, *MNRAS*, 459, 971
- Köhlinger F., Viola M., Valkenburg W., Joachimi B., Hoekstra H., Kuijken K., 2016, *MNRAS*, 456, 1508
- Komatsu E. et al., 2009, *ApJS*, 180, 330
- Kuijken K., 2008, *A&A*, 482, 1053
- Kuijken K. et al., 2015, *MNRAS*, 454, 3500
- Laigle C. et al., 2016, *ApJS*, 224, 24
- Landy S. D., Szalay A. S., 1993, *ApJ*, 412, 64
- Laureijs R. et al., 2011, preprint ([arXiv:1110.3193](https://arxiv.org/abs/1110.3193))
- Lewis A., Bridle S., 2002, *Phys. Rev. D*, 66, 103511
- Lewis A., Challinor A., Lasenby A., 2000, *ApJ*, 538, 473
- Li Y., Hu W., Takada M., 2014, *Phys. Rev. D*, 89, 083519
- Lilly S. J. et al., 2009, *ApJS*, 184, 218
- Lima M., Cunha C. E., Oyaizu H., Frieman J., Lin H., Sheldon E. S., 2008, *MNRAS*, 390, 118
- MacCrann N., Zuntz J., Bridle S., Jain B., Becker M. R., 2015, *MNRAS*, 451, 2877
- Mandelbaum R., Slosar A., Baldauf T., Seljak U., Hirata C. M., Nakajima R., Reyes R., Smith R. E., 2013, *MNRAS*, 432, 1544
- Mandelbaum R. et al., 2015, *MNRAS*, 450, 2963
- Massey R. et al., 2007, *ApJS*, 172, 239
- Masters D. et al., 2015, *ApJ*, 813, 53
- Matthews D. J., Newman J. A., 2010, *ApJ*, 721, 456
- Mead A., 2015, Astrophysics Source Code Library, record ascl:1508.001
- Mead A. J., Peacock J. A., Heymans C., Joudaki S., Heavens A. F., 2015, *MNRAS*, 454, 1958
- Mead A. J., Heymans C., Lombriser L., Peacock J. A., Steele O. I., Winther H. A., 2016, *MNRAS*, 459, 1468
- Melchior P., Viola M., 2012, *MNRAS*, 424, 2757
- Ménard B., Scranton R., Schmidt S., Morrison C., Jeong D., Budavári T., Rahman M., 2013, preprint ([arXiv:1303.4722](https://arxiv.org/abs/1303.4722))
- Miller L., Kitching T. D., Heymans C., Heavens A. F., van Waerbeke L., 2007, *MNRAS*, 382, 315
- Miller L. et al., 2013, *MNRAS*, 429, 2858
- More S., Miyatake H., Mandelbaum R., Takada M., Spergel D. N., Bernstein J. R., Schneider D. P., 2015, *ApJ*, 806, 2
- Morrison C. B., Hildebrandt H., 2015, *MNRAS*, 454, 3121
- Navarro J. F., Frenk C. S., White S. D. M., 1996, *ApJ*, 462, 563
- Newman J. A., 2008, *ApJ*, 684, 88
- Newman J. A. et al., 2013, *ApJS*, 208, 5
- Newman J. A. et al., 2015, *Astropart. Phys.*, 63, 81
- Olive K. A. et al. (Particle Data Group), 2014, *Chin. Phys.*, C38, 090001 [and 2015 update]
- Peacock J. A. et al., 2001, *Nature*, 410, 169
- Planck Collaboration XLVI, 2016, preprint ([arXiv:1605.02985](https://arxiv.org/abs/1605.02985))
- Planck Collaboration XIII, 2016a, *A&A*, 594, A13
- Planck Collaboration XXIV, 2016b, *A&A*, 594, A24
- Planck Collaboration XXVII, 2016c, *A&A*, 594, A27
- Rafelski M. et al., 2015, *AJ*, 150, 31
- Rahman M., Ménard B., Scranton R., Schmidt S. J., Morrison C. B., 2015, *MNRAS*, 447, 3500
- Rahman M., Mendez A. J., Ménard B., Scranton R., Schmidt S. J., Morrison C. B., Budavári T., 2016, *MNRAS*,
- Refregier A., 2003, *MNRAS*, 338, 35
- Refregier A., Kacprzak T., Amara A., Bridle S., Rowe B., 2012, *MNRAS*, 425, 1951
- Riess A. G. et al., 2016, *ApJ*, 826, 56
- Rix H.-W. et al., 2004, *ApJS*, 152, 163
- Robin A. C., Reylé C., Derrière S., Picaud S., 2003, *A&A*, 409, 523
- Ross A. J., Samushia L., Howlett C., Percival W. J., Burden A., Manera M., 2015, *MNRAS*, 449, 835
- Rowe B. T. P. et al., 2015, *Astron. Comput.*, 10, 121
- Samushia L. et al., 2014, *MNRAS*, 439, 3504
- Sato M., Takada M., Hamana T., Matsubara T., 2011, *ApJ*, 734, 76
- Schirmer M., 2013, *ApJS*, 209, 21
- Schlegel D. J., Finkbeiner D. P., Davis M., 1998, *ApJ*, 500, 525
- Schmidt S. J., Ménard B., Scranton R., Morrison C., McBride C. K., 2013, *MNRAS*, 431, 3307
- Schneider P., 2016, *A&A*, 592, L6
- Schneider P., van Waerbeke L., Mellier Y., 2002a, *A&A*, 389, 729
- Schneider P., van Waerbeke L., Kilbinger M., Mellier Y., 2002b, *A&A*, 396, 1
- Schneider P., Eifler T., Krause E., 2010, *A&A*, 520, A116
- Scoccimarro R., Sheth R. K., Hui L., Jain B., 2001, *ApJ*, 546, 20
- Scoville N. et al., 2007, *ApJS*, 172, 1
- Scranton R. et al., 2002, *ApJ*, 579, 48

- Sellentin E., Heavens A. F., 2016, MNRAS, 456, L132
 Semboloni E., Hoekstra H., Schaye J., van Daalen M. P., McCarthy I. G., 2011, MNRAS, 417, 2020
 Shanks T. et al., 2015, MNRAS, 451, 4238
 Sifón C. et al., 2015, MNRAS, 454, 3938
 Singh S., Mandelbaum R., More S., 2015, MNRAS, 450, 2195
 Skrutskie M. F. et al., 2006, AJ, 131, 1163
 Smith R. E. et al., 2003, MNRAS, 341, 1311
 Spergel D. N., Flauger R., Hložek R., 2015, Phys. Rev. D, 91, 023518
 Spiegelhalter D. J., Best N. G., Carlin B. P., Van Der Linde A., 2002, J. R. Stat. Soc. B, 64, 583
 Takada M., Hu W., 2013, Phys. Rev. D, 87, 123504
 Takahashi R., Sato M., Nishimichi T., Taruya A., Oguri M., 2012, ApJ, 761, 152
 Taylor A., Joachimi B., 2014, MNRAS, 442, 2728
 Taylor A. N., Kitching T. D., Bacon D. J., Heavens A. F., 2007, MNRAS, 374, 1377
 Tinker J. L., Robertson B. E., Kravtsov A. V., Klypin A., Warren M. S.,Yepes G., Gottlöber S., 2010, ApJ, 724, 878
 Trotta R., 2008, Contemp. Phys., 49, 71
 Troxel M. A., Ishak M., 2015, Phys. Rep., 558, 1
 Vaccari M. et al., 2012, Science from the Next Generation Imaging and Spectroscopic Surveys. ESO, Garching
 Vale C., Hoekstra H., van Waerbeke L., White M., 2004, ApJ, 613, L1
 Valentijn E. A. et al., 2007, in Shaw R. A., Hill F., Bell D. J., eds, ASP Conf. Ser. Vol. 376, Astronomical Data Analysis Software and Systems XVI. Astron. Soc. Pac., San Francisco, p. 491
 van Daalen M. P., Schaye J., Booth C. M., Dalla Vecchia C., 2011, MNRAS, 415, 3649
 van Uitert E., Schneider P., 2016, A&A, 595, A39
 van Uitert E. et al., 2016, MNRAS, 459, 3251
 Van Waerbeke L., White M., Hoekstra H., Heymans C., 2006, Astropart. Phys., 26, 91
 Viola M., Kitching T. D., Joachimi B., 2014, MNRAS, 439, 1909
 Viola M. et al., 2015, MNRAS, 452, 3529
 Voigt L. M., Bridle S. L., 2010, MNRAS, 404, 458
 Wall J. V., Jenkins C. R., 2012, Practical Statistics for Astronomers. Cambridge Univ. Press, Cambridge
 Zehavi I. et al., 2002, ApJ, 571, 172

APPENDIX A: REQUIREMENTS ON THE SHEAR AND PHOTO- z CALIBRATIONS

Given the statistical power of KiDS-450, it is important to ask the question how well we need to calibrate the shear and photo- z estimates. We use a Fisher matrix formalism to get such an estimate of the required calibration. As a fiducial model, the following analysis adopts a standard Λ CDM cosmology with parameters $\Omega_m = 0.2905$, $\Omega_b = 0.0473$, $\sigma_8 = 0.826$, $h = 0.69$, $n_s = 0.969$, and $\Omega_\Lambda = 1 - \Omega_m$ from Hinshaw et al. (2013).

A1 Fisher matrix

As a general approach to the problem, we imagine a vector \mathbf{x} of random data points which is fitted by a model with parameters $\mathbf{p} = (p_1, p_2, \dots, p_{N_p})$. Here we employ two fitting parameters $\mathbf{p} = (\Omega_m, S_8)$. The data are subject to random noise \mathbf{n} as defined by

$$\mathbf{x} = \mathbf{m}(\mathbf{p}) + \mathbf{n}(\mathbf{p}), \quad (\text{A1})$$

where \mathbf{m} is the predicted model vector. The random noise vanishes on average, $\langle \mathbf{n}(\mathbf{p}) \rangle = 0$, and the covariance of noise is $\mathbf{C}(\mathbf{p}) \equiv \langle \mathbf{n}(\mathbf{p})\mathbf{n}(\mathbf{p})^T \rangle$. Thus, for a Gaussian noise model, the covariance \mathbf{C} fully defines the noise properties. A perfect, non-degenerate model reproduces the noise-free data vector for one particular set

of parameters \mathbf{p}_{true} , such that $\langle \mathbf{x} \rangle = \mathbf{m}(\mathbf{p}_{\text{true}})$. In the following, \mathbf{p}_{true} denotes our fiducial cosmology.

From noisy data, we infer the parameters \mathbf{p} up to a statistical uncertainty $\Delta \mathbf{p}$ determined by the data likelihood $\mathcal{L}(\mathbf{x}|\mathbf{p})$. The Cramér–Rao lower bound provides a lower limit for the parameter uncertainty,

$$\left\langle (\Delta p_i)^2 \right\rangle \geq [\mathbf{F}^{-1}]_{ii} \quad (\text{A2})$$

through the Fisher matrix \mathbf{F} , which for a Gaussian likelihood is given by

$$F_{ij} := - \left\langle \frac{\partial^2 \ln \mathcal{L}(\mathbf{x}|\mathbf{p})}{\partial p_i \partial p_j} \right\rangle \Big|_{\mathbf{p}=\mathbf{p}_{\text{true}}} = \frac{1}{2} \text{tr} \left(\mathbf{C}^{-1} \mathbf{C}_{,i} \mathbf{C}^{-1} \mathbf{C}_{,j} + \mathbf{C}^{-1} [\mathbf{m}_{,i} \mathbf{m}_{,j}^T + \mathbf{m}_{,j} \mathbf{m}_{,i}^T] \right) \quad (\text{A3})$$

for the matrix components of \mathbf{F} , where

$$\mathbf{C}_{,i} := \frac{\partial \mathbf{C}(\mathbf{p})}{\partial p_i} \Big|_{\mathbf{p}=\mathbf{p}_{\text{true}}} ; \mathbf{m}_{,i} := \frac{\partial \mathbf{m}(\mathbf{p})}{\partial p_i} \Big|_{\mathbf{p}=\mathbf{p}_{\text{true}}} \quad (\text{A4})$$

(Taylor et al. 2007). The diagonal elements $[\mathbf{F}^{-1}]_{ii}$ are the square of the Fisher error of p_i , $\sigma(p_i)$, whereas the off-diagonals $[\mathbf{F}^{-1}]_{ij}$ quantify the covariance between p_i and p_j .

For KiDS-450, we express \mathbf{m} by a tomography of shear power spectra, similar to Hu (2002), with 30 logarithmic bins covering angular wavenumbers ℓ between 280 and 5000. For a model of the noise covariance \mathbf{C} , we apply Joachimi et al. (2008) using the effective number density and ellipticity dispersion as listed in Table 1. With this setup, we obtain Fisher errors of $\sigma(\Omega_m) = 0.104$ and $\sigma(S_8) = 0.033$, as well as a Pearson correlation of $r = -0.91$ between them. Note that these errors are in good agreement with those obtained from our ‘no-systematics’ MCMC analysis but, predictably, are slightly smaller than what we find once we allow for other uncertainties (see Table F2).

A2 Bias due to calibration errors

We imagine a model $\mathbf{m}(\mathbf{p})$ which has a set of additional nuisance or calibration parameters $\mathbf{q} = (q_1, q_2, \dots, q_{N_q})$ which are constrained by external information rather than by the data \mathbf{x} . With nuisance parameters included, both the model and the noise covariance are also functions of \mathbf{q} , henceforth denoted by $\mathbf{m}(\mathbf{p}|\mathbf{q})$ and $\mathbf{C}(\mathbf{p}|\mathbf{q})$, respectively. By \mathbf{q}_{true} we denote the values of nuisance parameters in the fiducial model.

If \mathbf{q}_{true} is known, nothing changes in comparison to the foregoing Fisher formalism; we just set $\mathbf{m}(\mathbf{p}) = \mathbf{m}(\mathbf{p}|\mathbf{q}_{\text{true}})$ and $\mathbf{C}(\mathbf{p}) = \mathbf{C}(\mathbf{p}|\mathbf{q}_{\text{true}})$. If, on the other hand, we adopt biased calibration parameters $\mathbf{q} = \mathbf{q}_{\text{true}} + \delta \mathbf{q}$, then the (average) likelihood function will, to linear order, be shifted by

$$\delta \mathbf{p} = -\mathbf{F}^{-1}(\mathbf{p}_{\text{true}}) \mathbf{G} \delta \mathbf{q} \quad (\text{A5})$$

(cf. the appendix of Taylor et al. 2007). Here, we have introduced the pseudo-Fisher matrix \mathbf{G} , whose elements G_{ij} are defined as in equation (A3) but where the partial derivatives are with respect to the nuisance parameters q_i ,

$$\mathbf{C}_{,i} := \frac{\partial \mathbf{C}(\mathbf{p}_{\text{true}}|\mathbf{q})}{\partial q_i} \Big|_{\mathbf{q}=\mathbf{q}_{\text{true}}} ; \mathbf{m}_{,i} := \frac{\partial \mathbf{m}(\mathbf{p}_{\text{true}}|\mathbf{q})}{\partial q_i} \Big|_{\mathbf{q}=\mathbf{q}_{\text{true}}} . \quad (\text{A6})$$

A3 Tolerance limits

For an accurate model fit, we require the typical bias $\delta \mathbf{p} = -\mathbf{F}^{-1} \mathbf{G} \delta \mathbf{q}$ to be small in comparison to the expected statistical error $\Delta \mathbf{p}$. For the following assessment, we assume for $\Delta \mathbf{p}$ a multivariate Gaussian probability density with covariance \mathbf{F}^{-1} and zero mean. The probability density function (PDF) of $\delta \mathbf{q}$ shall also obey Gaussian statistics, now with a variance of σ_i^2 for each component δq_i . As test statistics for the significance of a $\delta \mathbf{p}$ relative to the typical distribution of statistical errors $\Delta \mathbf{p}$, we use

$$\Delta \chi^2(\delta \mathbf{q}) := \delta \mathbf{p}^T \mathbf{F}(\mathbf{p}_{\text{true}}) \delta \mathbf{p} \quad (\text{A7})$$

$$= \delta \mathbf{q}^T (\mathbf{G}^T \mathbf{F}^{-1}(\mathbf{p}_{\text{true}}) \mathbf{G}) \delta \mathbf{q}. \quad (\text{A8})$$

Given a PDF model for $\delta \mathbf{q}$, the statistics $\Delta \chi^2(\delta \mathbf{q})$ follow a distribution for which the 68th percentile $\Delta \chi_{68}^2$, given by

$$P(\Delta \chi^2(\delta \mathbf{q}) \leq \Delta \chi_{68}^2) = 0.68, \quad (\text{A9})$$

quantifies the spread of values. We compute the values of $\Delta \chi_{68}^2$ for a range of models for $\delta \mathbf{q}$ which differ in σ_i^2 . For each model, we then consider the impact of a bias $\delta \mathbf{q}$ negligible relative to statistical errors $\Delta \mathbf{p}$ if the corresponding value of $\Delta \chi_{68}^2$ is small compared to the distribution $\Delta \chi_0^2 := \Delta \mathbf{p}^T \mathbf{F}(\mathbf{p}_{\text{true}}) \Delta \mathbf{p}$, or if the probability of $\Delta \chi_0^2 \geq \Delta \chi_{68}^2$ is large. We assess this by computing numerically the *p*-value

$$p_{68} = P(\Delta \chi_0^2 \geq \Delta \chi_{68}^2) \quad (\text{A10})$$

by doing MC realizations of $\Delta \chi_0^2$ based on random values of $\Delta \mathbf{p}$. A large value of p_{68} thus indicates that statistical errors $\Delta \mathbf{p}$ are large in comparison to systematic errors $\delta \mathbf{p}$: The bias is negligible.

For KiDS-450, we consider two types of calibration errors $\delta \mathbf{q}$ in each of the four tomographic bins: a systematic shift of the redshift distribution, $z = z_{\text{true}}(1 + \delta z)$, and a systematic error of shear values, $\gamma = \gamma_{\text{true}}(1 + m)$. The photo-z errors are slightly correlated between the tomographic bins i and j according to the correlation matrix

$$[\mathbf{r}]_{ij} = \begin{pmatrix} 1 & +0.03 & -0.02 & +0.04 \\ +0.03 & 1 & -0.03 & +0.01 \\ -0.02 & -0.03 & 1 & +0.08 \\ +0.04 & +0.01 & +0.08 & 1 \end{pmatrix}, \quad (\text{A11})$$

which we determined by bootstrapping the data. The systematic errors of shear, however, are strongly correlated. We adopt a correlation coefficient of $r = 0.99$ between all bins throughout. This represents a worst case scenario in terms of deriving requirements for the shear bias calibration uncertainty. We indeed expect a strong correlation between the multiplicative biases in the four tomographic bins, as they share very similar distributions in terms of S/N and galaxy size, which are the main parameters used to characterize the shear bias (see Appendix D). The resulting *p*-values as a function of uncertainty of calibration errors are shown in the top panel of Fig. A1. Here we assume the photo-z error to be the same in each bin as given by the value on the *y*-axis. The *p*-value drops below 95 per cent for photo-z and shear calibration errors with rms uncertainties $\sigma_{\delta z}, \sigma_m \sim 1.5$ per cent for all four bins.

In addition, we consider uncertainties which mimic our calibration precision in KiDS-450, wherein the uncertainties differ across the tomographic bins. The correlations of errors are as before. The systematic redshift error (taking the relative error of the mean from column 8 in Table 1) is $\{\sigma_{\delta z, i}\} = \{4.8, 2.8, 1.4, 0.7\}$ per cent, and the shear bias is calibrated to a precision of either $\sigma_m = 0.5$ per cent (optimistic) or $\sigma_m = 1$ per cent (pessimistic) in all bins. We find p_{68}

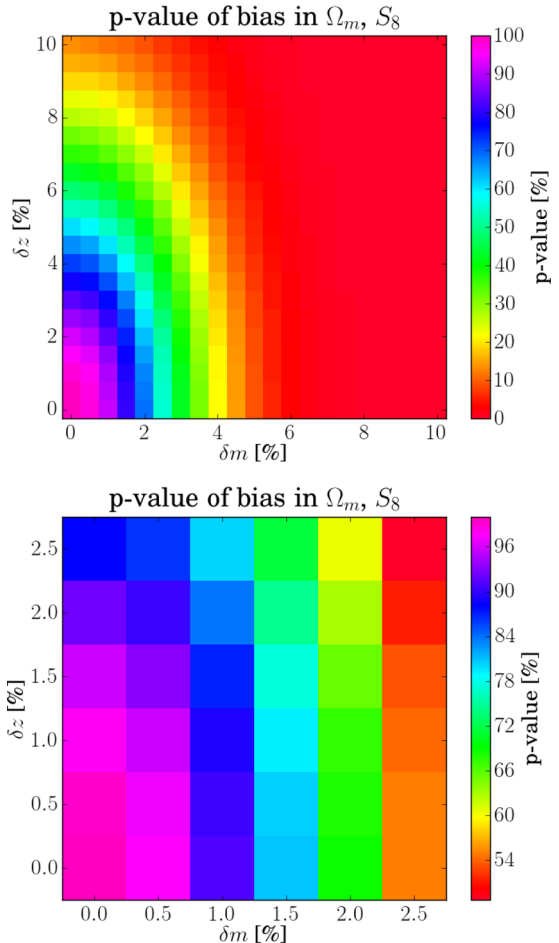


Figure A1. The value of p_{68} , the bias in the cosmological parameters Ω_m and S_8 if the error in the multiplicative shear calibration δm and the error in the mean redshift of the tomographic bins δz are not corrected. The lower panel zooms in on the relevant region of parameter space.

= 0.66(0.71) in the pessimistic (optimistic) scenario. This implies that the low-level systematics which we have identified and calibrated could bias our results such that we need to also marginalize over our uncertainty in the measured calibration.

A4 Marginalizing calibration errors

We consider the possibility that the uncertainty of $\delta \mathbf{q}$ is directly accounted for in the statistical errors of model parameters \mathbf{p} . Thus, we do not set the calibration parameters to a specific value but, instead, marginalize over the uncertainty in \mathbf{q} . For this discussion, we assume that the PDF of \mathbf{p} is well approximated by a Gaussian density: $\mathcal{N}(\mathbf{p}_{\text{true}}, \mathbf{F}^{-1})$; it has the mean \mathbf{p}_{true} and the covariance $\mathbf{F}^{-1}(\mathbf{p}_{\text{true}})$. In addition, we define a Gaussian prior PDF of the calibration error $\delta \mathbf{q}$, namely $\mathcal{N}(0, \mathbf{C}_q)$, with zero mean and covariance $\mathbf{C}_q = \langle \delta \mathbf{q} \delta \mathbf{q}^T \rangle$. The calibration uncertainty corresponds to the systematic error in \mathbf{p} space which has the covariance

$$\mathbf{C}_p = \langle \delta \mathbf{p} \delta \mathbf{p}^T \rangle = \mathbf{F}^{-1} \mathbf{G} \mathbf{C}_q \mathbf{G}^T \mathbf{F}^{-1} \quad (\text{A12})$$

because $\delta \mathbf{p} = -\mathbf{F}^{-1} \mathbf{G} \delta \mathbf{q}$. Marginalizing with respect to $\delta \mathbf{p}$ hence adds extra uncertainty to $\mathcal{N}(\mathbf{p}_{\text{true}}, \mathbf{F}^{-1})$, which we obtain by convolving this PDF with the kernel $\mathcal{N}(0, \mathbf{C}_q)$. This results in the Gaussian $\mathcal{N}(\mathbf{p}_{\text{true}}, \mathbf{F}_m^{-1})$ with broadened covariance

$$\mathbf{F}_m^{-1} = \mathbf{C}_p + \mathbf{F}^{-1} = \mathbf{F}^{-1} (\mathbf{G} \mathbf{C}_q \mathbf{G}^T + \mathbf{F}) \mathbf{F}^{-1}. \quad (\text{A13})$$

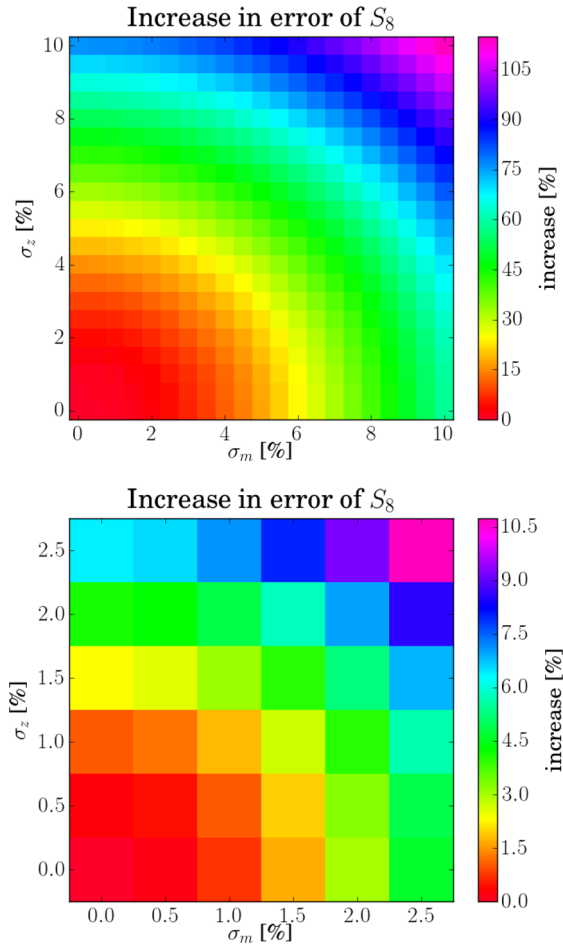


Figure A2. The percentage increase in the errors of the composite parameter S_8 if the uncertainties in the multiplicative shear calibration, σ_m , and the mean redshifts, σ_z , are marginalized over. The lower panel zooms in on the relevant region of parameter space.

We utilize the marginal Fisher matrix \mathbf{F}_m to assess the relative growth of the Fisher error of the composite parameter S_8 due to marginalization. For this, we plot the fractional increase $\sigma(S_8)/\sigma_0 - 1$ of $\sigma(S_8) = \sqrt{[\mathbf{F}_m^{-1}]_{22}}$ relative to $\sigma_0 = \sqrt{[\mathbf{F}^{-1}]_{22}}$.

The situation for KiDS-450 is shown in Fig. A2. It can be seen that the errors on the relevant cosmological parameters increase by ~ 2 per cent for shear and photo-z calibrations which are known to ~ 1 per cent if those uncertainties are marginalized over. Again it is assumed that the photo-z errors are the same in all bins.

For the calibration precision of KiDS-450, i.e. photo-z errors of $\{\sigma_{\delta z, i}\} = \{4.8, 2.8, 1.4, 0.7\}$ per cent in the four bins and a shear calibration error of $\sigma_m = 0.5$ per cent (optimistic) or $\sigma_m = 1$ per cent (pessimistic), we find the corresponding values of ~ 8.1 and ~ 8.7 per cent in the optimistic and pessimistic scenarios, respectively. This error is dominated by the uncertainty of the photo-z calibration in the first tomographic bin. The actual increase in the error on S_8 , which we find when switching from the ‘DIR-no-error’ case to the ‘DIR’ case (see Table 4), is of the order of ~ 3 per cent. This suggests that the linear model we are using here in this Fisher analysis by shifting the redshift distribution coherently around is too pessimistic compared to the complex changes in the shape of the redshift distributions, especially for the first tomographic bin. The results in this section can hence be understood as upper limits

on how much systematic errors in the shear and photo-z calibration compromise the statistical power of KiDS-450.

APPENDIX B: PHOTOMETRIC CALIBRATION WITH STELLAR LOCUS REGRESSION

Photometric homogeneity is an important requirement for a large imaging survey such as KiDS. It is difficult to attain because the observations consist of many separate tiles observed over a time span of years, and in conditions which are not always fully photometric. For this reason, KiDS tiles overlap slightly with their neighbours, so that sources common to adjacent tiles can be used to cross-calibrate the individual tiles’ photometric zero-points. However, as Fig. 1 shows, the KiDS-450 data are still quite fragmented, especially outside the main contiguous areas in G9, G12, G15, G23, and GS, and therefore tile overlaps are inadequate to obtain homogeneous photometry across the full data set. The results of the tile-by-tile KiDS photometric calibration described in Section 2.2 and de Jong et al. (2015) are reported in Table B1, finding a scatter in the $(u - r, g - r, r - i)$ colours of $(0.04, 0.04, 0.06)$ with respect to the SDSS DR9 photometry, as well as an average offset of $(0.005, 0.005, 0.015)$ mag. In addition, we find that some outlier tiles can display magnitude residuals up to 0.1 in g , r , and i and up to 0.2 in u (de Jong et al. 2015).

In order to improve the photometric calibration, particularly in KiDS-S, wherein there is no overlap with SDSS photometry, we make use of the fact that the majority of stars display a well-defined photometric ‘stellar locus’: a tight relation in colour–colour space which varies little across the sky outside the Galactic plane (Ivezić et al. 2004; High et al. 2009). Matching the observed loci to the fiducial intrinsic locus therefore offers the possibility to achieve colour homogeneity for the KiDS-450 tiles without using the photometry of objects in the overlap regions of different exposures. We follow the usual nomenclature and refer to this approach as stellar locus regression (SLR).

B1 Implementation and results

We apply the SLR to the KiDS GAAP (Gaussian Aperture and Photometry; Kuijken 2008) photometry. The first step is to determine ‘principal colours’: linear combinations of $u - g$, $g - r$, and $r - i$ which align with the characteristic straight regions of each stellar locus in colour–colour space. Following the approach of Ivezić et al. (2004), we define four principal colours (see Table B2 for the fitting coefficients which are taken from Ivezić et al. 2004):

- (i) s (straight region in $u - g, g - r$);
- (ii) x (straight red region in $g - r, r - i$);
- (iii) w (straight blue region in $g - r, r - i$);
- (iv) k (straight region in $u - r, r - i$).

For each principal colour c , $P1c$ and $P2c$ denote the colour projected along/perpendicular to the stellar locus, respectively. Any deviation from the fiducial stellar locus reveals itself as a non-zero $P2$ colour. Since there are only three independent colours in the data set, we choose to line up the stellar loci by perturbing only the $u - r, g - r$, and $r - i$ colours in each tile, and to leave the r -band zero-points unchanged. Indeed, analysis of the per-tile calibration residuals shows the r band to be the most homogeneous (de Jong et al. 2015).

Given the small differences between the KiDS and SDSS photometric systems (de Jong et al. 2015), we use the same intrinsic

Table B1. Main results from the SLR applied to the KiDS GAAP photometry. Comparisons to SDSS use its DR9 PSF photometry (Ahn et al. 2012). Column 2: indicator of achieved colour homogeneity prior to applying SLR. Listed are the mean and standard deviation of the colour residual per tile when subtracting the SDSS and KiDS stellar photometry. Column 3: derived SLR corrections. Column 4: same as Column 2 but now after SLR has been applied. For comparison and to judge the intrinsic scatter of the method, we also apply SLR to the SDSS photometry and then compare with the original SDSS photometry in Column 5.

Colour	KiDS – SDSS before SLR (mmag)	SLR offset (mmag)	KiDS–SDSS after SLR (mmag)	(SDSS+SLR) – SDSS (mmag)
$d(u - r)$	4 ± 42	71 ± 87	80 ± 64	26 ± 38
$d(g - r)$	6 ± 38	14 ± 75	9 ± 12	11 ± 10
dr	11 ± 28	—	11 ± 28	NA
$d(r - i)$	-16 ± 56	-21 ± 60	-6 ± 11	4 ± 6

Table B2. Coefficients from Ivezić et al. (2004) which define the principal colours s, x, w , and k . Listed are the coefficients defining the principal colour perpendicular to the straight locus. For example, $P2s = -0.249 u + 0.794 g - 0.555 r + 0.234$.

Principal colour	u	g	r	i	Constant
$P2s$	-0.249	0.794	-0.555		0.234
$P2x$		0.707	-0.707		-0.988
$P2w$			-0.227	0.792	0.050
$P2k$	0.114			-1.107	0.994
					-0.0420

locations for s, x , and w as Ivezić et al. (2004). The fourth, redundant principal colour k is used as an additional guard for fitting robustness.

In each tile, we select bright point sources with $r < 19.0$ on the Gaussianized co-adds using the following criteria:

- (i) $2 < \text{FWHM} < 4$ pixels
- (ii) $\text{Flag_r} = 0$
- (iii) $\text{IMAFLAGS_ISO_r} = 0$

The first criterion selects point-like objects, and the second and third remove sources with compromised photometry (see de Jong et al. 2015 for precise definitions). For each point source, the GAAP magnitude is corrected for Galactic extinction using the $E(B - V)$ colour excess from Schlegel et al. (1998) in combination with a standard $R_V = 3.1$ Galactic extinction curve. This assumes that most of the stars used for calibration are outside the dust disc of the Milky Way. For each principal colour, we then compute the $P1$ and $P2$ components of these sources, as shown in Fig. B1. We identify sources near the straight region of the stellar locus by setting a fixed range around the median $P1$ and requiring $|P2 - \text{median}(P2)| \lesssim 200$ mmag. Per tile the median $P2$ values of these sources are finally converted into three colour offsets $d(u - r)$, $d(g - r)$, and $d(r - i)$, and applied to the KiDS GAAP magnitudes before they are fed to the photo- z code. Column 3 of Table B1 lists the distribution of the resulting offsets, which are also shown in Fig. B2. For comparison and to judge the intrinsic scatter of the method, we also apply SLR to the SDSS photometry and then compare with the original photometry. Those findings are reported in the last column of Table B1.

We find that SLR on KiDS GAAP photometry significantly improves the photometric stability over the survey area in the $g - r$ and $r - i$ colours. The fluctuations with respect to SDSS decrease from ~ 0.04 and ~ 0.06 mag in $g - r$ and $r - i$, respectively, to roughly 0.01 mag in both colours. The calibration of the $u - r$ colour, however, does not improve: the scatter after SLR (~ 0.06 mag) is slightly larger than before SLR (~ 0.04 mag). Also a significant offset of

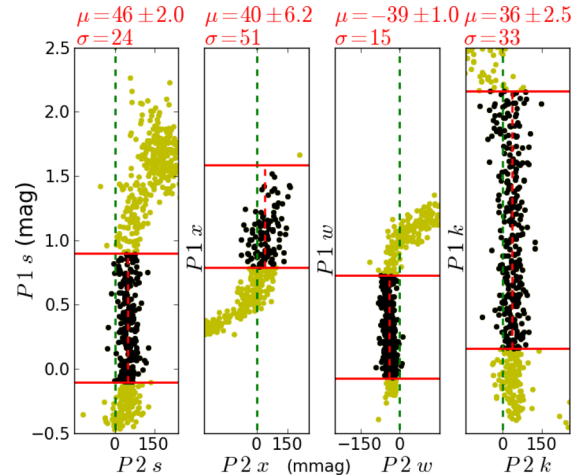


Figure B1. Principal colours s, w, x , and k for the pointing KiDS_3.6_-34.1. The initial selection of stars (all points) is identical for s, w, x , and k . From this parent sample, the stars on the locus are selected (black). The inferred median $P2$ offsets, its formal error and the standard deviation of the locus point sources are shown above each panel.

~ 0.08 mag is introduced. We attribute these problems to metallicity variations in the stellar sample, which results in a variable stellar locus, making this technique fundamentally problematic for near-ultraviolet data (similar findings are reported by High et al. 2009). In the final column of Table B1, we see that applying SLR to the actual SDSS data also degrades the calibration of the $u - r$ colour.

We argue that the photo- z calibration (Section 3) is in no way compromised by the offset in the $u - r$ calibration since the spectroscopic calibration fields are also calibrated with SLR and hence share this offset. The ~ 0.06 mag fluctuation of the $u - r$ photometry leads to a tile-to-tile difference in the photo- z bias, and hence in the redshift distribution. The redshift distributions estimated from the four calibration deep spec- z fields are still applicable, on average,

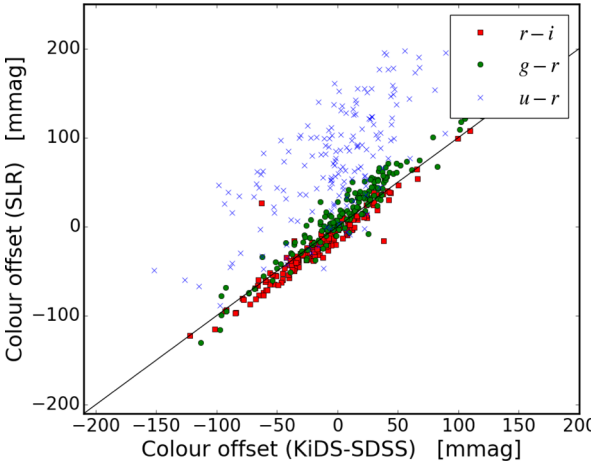


Figure B2. The offsets in the $u - r$, $g - r$, and $r - i$ colours predicted by SLR versus the predictions from a direct comparison with SDSS. The mean and standard deviation of the distributions are listed in Table B1.

if the fluctuations between those four fields are comparable to the full survey. Also given the relatively large errors of the individual u -band measurements, we do not expect this 0.06 mag fluctuation in $u - r$ to have any major consequences for the applicability of the redshift calibration.

APPENDIX C: PHOTO- z CALIBRATION ANALYSIS

C1 VST imaging of deep spec- z fields

We calibrate the KiDS-450 tomographic redshift distributions through the analysis of deep spectroscopic data sets from the literature. In order to extend our spectroscopic overlap, we incorporate VST observations of a number of deep spectroscopic fields which fall outside the main KiDS survey footprint (Table C1). The DIR calibration procedure described in Section 3.2 reweights the spec- z catalogue such that it represents the colour and magnitude properties of the photometric catalogue. Magnitude errors will inevitably be affected by noise variations across the survey area caused by variations in seeing, exposure time, atmospheric extinction, moon phase, and distance, among others. It is therefore important that the observing setup and conditions of the imaging observations in the deep spectroscopic fields are representative of the main KiDS survey observations such that the reweighting scheme, determined from the spec- z fields, is valid in its application to the full KiDS-450 area.

Table C1 summarizes the observing conditions in the four fields, in comparison to the mean observing conditions in KiDS-450. It demonstrates that these data are indeed typical in terms of exposure time and seeing. The PSF ellipticity and size variations between the observations are taken care of by our galaxy photometry pipeline.

C2 Statistical errors in DIR and CC calibrations

Given the importance of the photometric redshifts for the interpretation of the tomographic cosmic shear measurements, we present an assessment of how the uncertainty in the $n(z)$ which we estimate from the KiDS-450 data propagates into errors on our theoretical model of the shear correlation function ξ_{\pm} . Statistical errors on both the weighted direct photo- z calibration and the cross-correlation

Table C1. Observing conditions in the spec- z fields compared to the main KiDS-450 survey. Central coordinates of the 1-deg² VST observations for each field are listed under the names of the fields.

Field	Band	Seeing FWHM (arcsec)	Exposure time (s)
KiDS-450 mean	u	1.01	1000
	g	0.87	900
	r	0.70	1800
	i	0.83	1200
COSMOS ^a (150.08, 2.20)	u	0.74	1000
	g	1.05	900
	r	0.57	1800
	i	1.04	1200
CDFS ^b (53.40, -27.56)	u	1.09	1200
	g	0.56	1080
	r	0.55	1800
	i	0.93	1200
	u	0.92	1000
DEEP2-2h ^c (37.16, 0.50)	g	0.91	900
	r	0.72	1800
	i	0.70	1200
	u	1.08	1000
DEEP2-23h ^c (352.00, 0.00)	g	0.96	900
	r	0.64	1800
	i	0.73	1200

Notes. ^aThe COSMOS field is observed as part of the KiDS survey.

^bData from the VOICE project (Vaccari et al. 2012).

^cData taken during OmegaCAM guaranteed time (2015 November).

photo- z calibration are estimated using 1000 bootstrap samples created from the full spec- z catalogue of 23 088 objects. For each bootstrap realization of the tomographic redshift distributions, we calculate a theoretical model for ξ_{\pm} for a fixed fiducial cosmology. The variance between the resulting models provides an estimate of the uncertainty on ξ_{\pm} , denoted by σ_{nz} , which arises purely from our uncertainty in the $n(z)$. Fig. C1 shows the S/N of ξ_{\pm} , with the noise given by σ_{nz} , for a selection of 6 out of the 10 tomographic bin combinations used in our analysis. The statistical noise from the weighted direct calibration estimate (DIR, solid line) is significantly lower than the statistical noise from the cross-correlation calibration (CC, dotted line), reflecting the lower precision of the latter technique, given the small-area spectroscopic surveys which we can cross-correlate with.

Fig. C1 can be compared with the actual S/N of measurements of ξ_{\pm} , presented in Fig. 4 for the same sample of tomographic bins. For the DIR calibration, we see that the σ_{nz} statistical errors are subdominant to the noise in the shear correlation function measurements on all scales. For the CC calibration, however, the σ_{nz} statistical errors are greater than the shot noise and sample variance in the data. The uncertainty on the CC calibrated $n(z)$ therefore significantly limits the cosmological information which can be extracted from the cosmic shear analysis, as shown in Fig. 7. We note that the spec- z catalogues used here are amongst the deepest and most complete surveys which are currently available. In the absence of new deeper spectroscopic surveys, Fig. C1 represents a limit on the precision of all lensing surveys, not just KiDS-450.

C3 Systematic error analysis

C3.1 Weighted direct calibration (DIR)

In principle, the weighted direct calibration method should be relatively free from systematic errors, provided the magnitude

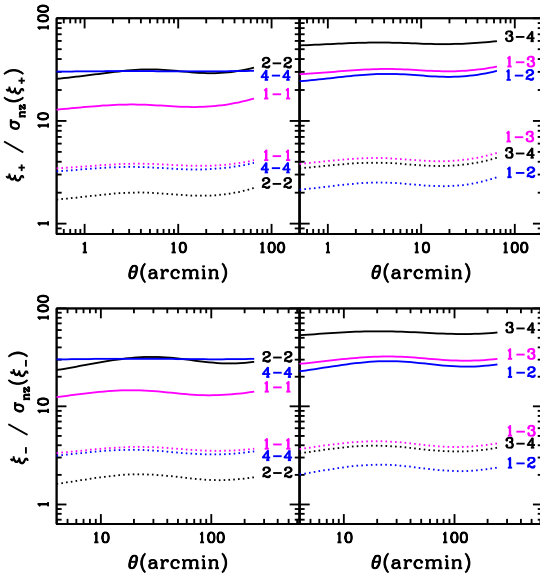


Figure C1. Redshift distribution uncertainty: S/N estimates of ξ_+ (upper panel) and ξ_- (lower panel) considering only the statistical noise σ_{nz} that arises from the uncertainty in the $n(z)$ as measured by the weighted direct calibration (DIR, solid line) and by the cross-correlation calibration (CC, dotted line). This can be compared with the actual S/N on measurements of ξ_\pm in the KiDS-450 data that are presented in Fig. 4 for the same sample of tomographic bins, labelled ‘ $i-j$ ’, where $i, j = 1, \dots, 4$.

measurements and spectroscopic redshifts are accurate. The only requirement is that the spec- z sample spans the full extent of the magnitude space which is covered by the photometric sample, and that the mapping from magnitude space to redshift is unique. In the following, we describe the tests which we have undertaken to verify that we have met these requirements.

In KiDS-450, we work in 4D (u, g, r, i) magnitude space. Fig. C2 shows the distribution of photometric and spectroscopic objects in different projections of this colour space. The spec- z sample is shown before and after reweighting. Any significant mismatch between the reweighted distribution of spec- z objects and the photometric objects would indicate a violation of the first requirement that the spec- z sample must span the extent of the phot- z sample. No obvious deviations are found if the full spec- z sample is used. Interestingly, if we run the reweighting algorithm with the COSMOS spec- z catalogue only, there is a very significant mismatch at faint magnitudes. This suggests that there are not enough faint high- z galaxies in the z-COSMOS catalogue which could be upweighted to match the distribution of the photometric catalogue. Including the DEEP2 and CDF-S catalogues cures this problem and leads to the distributions shown in Fig. C2. We rerun the same test for the four tomographic bins individually, finding a good match for all bins in all bands.

The requirement of a unique mapping from magnitude space to redshift cannot be tested easily. Given that we are working with four bands only, there is certainly some concern that this requirement is not completely fulfilled. If this was the case, there would be regions in magnitude space which correspond to several very different redshift ranges. These phenomena are also called colour-redshift degeneracies (see e.g. Benítez 2000). This is one of the reasons why we limit the cosmic shear analysis to photometric redshifts in the range of $0.1 < z_B \leq 0.9$. As indicated in fig. 12 of Kuijken et al. (2015), the outlier rate of our photo- z is very low in this photometric redshift range. While this could also be caused by

spectroscopic incompleteness, this result is confirmed by analysing simulated mock KiDS photometry catalogues. Given these results, we are confident that the combination of a highly complete spec- z sample (as indicated by Fig. C2), and a conservative photo- z range means that we meet the requirements for the weighted direct calibration.

Another possible source of systematic error in the DIR calibration is sample variance due to the finite size of the spectroscopic training sample. The $n(z)$ are clearly affected by this sample variance as can be seen from their non-smooth shape in Fig. 2. However, the relevant question is whether this sample variance in the photo- z calibration contributes significantly to the total error budget of the cosmological parameters of interest. Cunha et al. (2012) estimate the effect of sample variance in the redshift calibration for DES from simulations. Their results are not directly applicable to KiDS-450 as their simulated survey covers an area of 5000 deg^2 , goes deeper ($n_{\text{eff}} = 12 \text{ arcmin}^{-2}$), reaches out to $z = 1.35$, and employs 20 tomographic bins. They also concentrate on the equation-of-state parameter w instead of S_8 . They find that the uncertainty in w due to photo- z calibration is larger than their statistical error ($\sigma_w = 0.035$) by a factor of ~ 4 if they use the same magnitude weighting technique as our DIR method [called $p(z)_w$ in their paper] and train this technique with a spec- z survey covering a single square degree and $\sim 10^4$ training galaxies (see their table 2). The S_8 parameter is somewhat more sensitive (within a factor of ~ 2) to redshift errors than w (see Huterer et al. 2006). However, given the more modest statistical power of KiDS-450 (compare their $\sigma_w = 0.035$ with our $\sigma_w \sim 1$) and our larger spec- z calibration sample which originates from four widely separated fields, we estimate that any leakage from the spec- z sample variance into our photo- z calibration is subdominant to our statistical uncertainties.

Similar conclusions can be reached by looking at the results of Van Waerbeke et al. (2006). They look at the more pessimistic case of direct photo- z calibration with spec- z but without magnitude weighting. For a cosmic shear survey of area 200 deg^2 , $n_{\text{eff}} = 20$, $z_{\text{max}} \approx 2$, and a spec- z calibration sample from 4 deg^2 , they find that for angular scales $\theta > 10 \text{ arcmin}$, the errors on the shear measurement (from shape noise and survey sample variance) dominate over the errors from the redshift calibration.

In order to further reduce sample variance in the redshift calibration, we plan to observe additional calibration fields which are covered by deep, public spectroscopic surveys. This will be necessary to keep pace with the growing KiDS survey and the shrinking statistical uncertainties.

C3.2 Calibration from cross-correlations (CC)

Calibrating the redshift distributions in the different tomographic bins with the help of angular cross-correlations has the great benefit that it does not require a representative sample of objects with spectroscopic redshifts. However, there are several systematic errors which can affect such a clustering redshift recovery. The cross-correlations are relatively robust against an angular selection function in one of the two samples (i.e. the photometric and spectroscopic samples) as long as the angular selection functions of both samples are not correlated themselves, e.g. because both mask out true structures like stars. The autocorrelation functions, which are needed to calibrate the typically unknown galaxy bias, are, however, heavily affected. One can therefore use only samples where

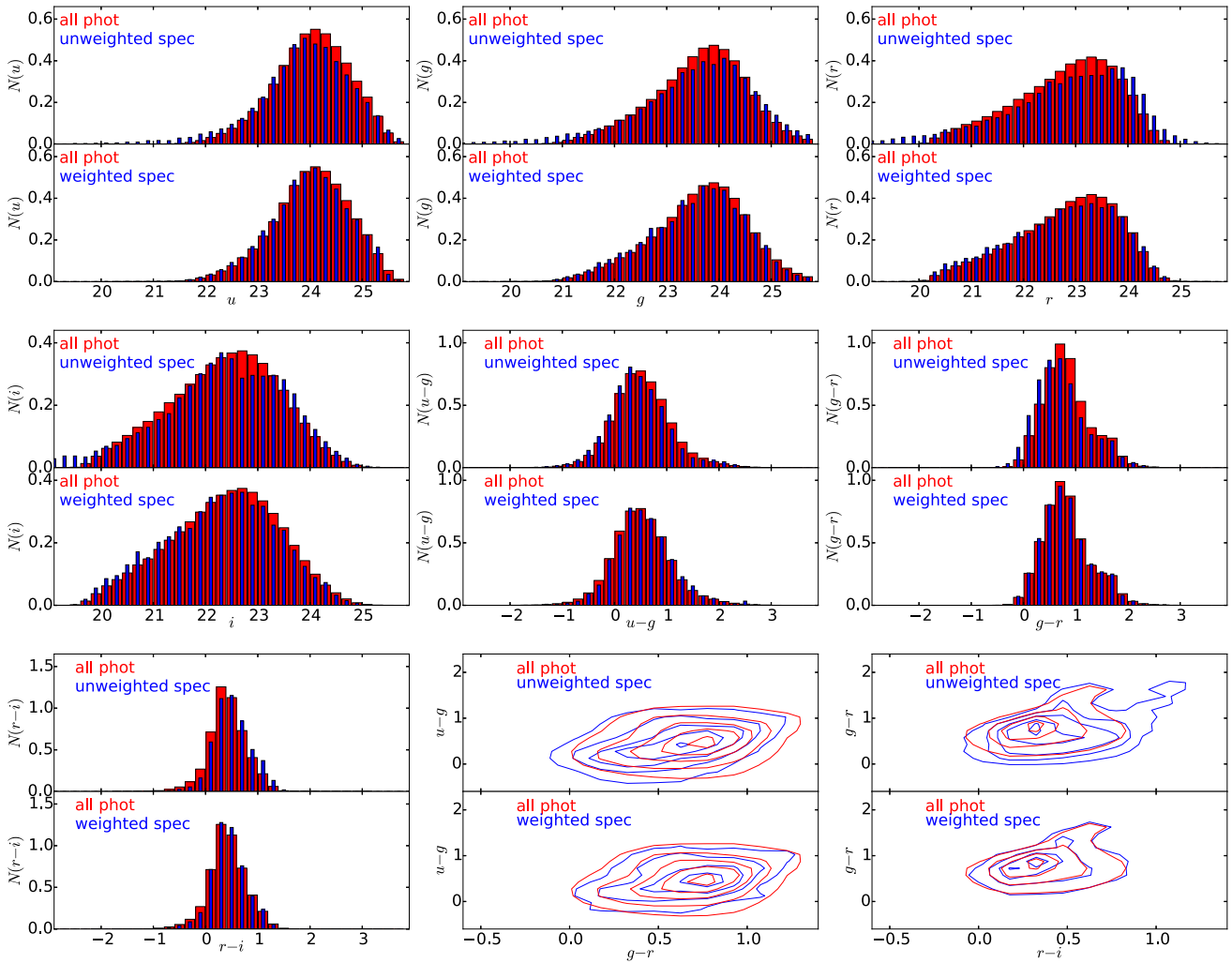


Figure C2. Magnitude and colour distributions of the photometric sample (red) and the spectroscopic sample (blue) before (upper panels) and after reweighting (lower panels). The first four panels show the magnitude distributions in the $ugri$ bands, the next three panels show the 1D colour distributions in the three independent colours $u - g$, $g - r$, and $r - i$, and the last two panels show 2D colour distributions in $u - g$ versus $g - r$ and $g - r$ versus $r - i$. While the match between the photometric and spectroscopic distributions is fairly good even without reweighting the spec- z sample, the match improves significantly after reweighting.

this angular selection function (or weighted footprint) is precisely known. Depending on colour/photo- z selections and noise properties, this can become highly non-trivial (see e.g. Morrison & Hildebrandt 2015 for an analysis of angular selection effects in CFHTLenS). In our particular case, this means that we can use only DEEP2 and – with some caveats – zCOSMOS in this analysis. Here all correlation functions are estimated with the publicly available STOMP library (Scranton et al. 2002).¹²

The other major systematic uncertainty in this method is related to the correction for the galaxy bias. For the spec- z sample, the galaxy bias can be estimated robustly as a function of redshift if the angular selection function is known. However, the fine bins which are typically used for the cross-correlations contain too few galaxies to yield a robust estimate of the autocorrelation function and hence the galaxy bias. We are therefore forced to use wider redshift bins for the autocorrelation, and interpolate the results. For the spectroscopic sample, we estimate the projected autocorrelation

function, $w_p(r_p)$, as defined in equation (9) of Matthews & Newman (2010). Following their method, we fit a power law to this projected autocorrelation:

$$w_p(r_p) \propto \left(\frac{r_p}{r_0}\right)^{-\gamma}, \quad (C1)$$

and interpolate the fitted parameters r_0 and γ to the redshift of each cross-correlation bin. For these projected autocorrelation function measurements, we choose redshift bins of constant comoving width so that we do not have to measure the clustering scalelength r_0 in absolute terms but just relatively between the different bins.

For the photometric sample, we estimate the angular autocorrelation function with the estimator of Landy & Szalay (1993) and also fit a power law:

$$w(\theta) = A \theta^{1-\gamma} - C, \quad (C2)$$

with A being the amplitude and C being the integral constraint. The relative clustering strengths are then adjusted with the method laid out in Matthews & Newman (2010, see their equation 13).

¹² <https://github.com/ryanscranton/astro-stomp>

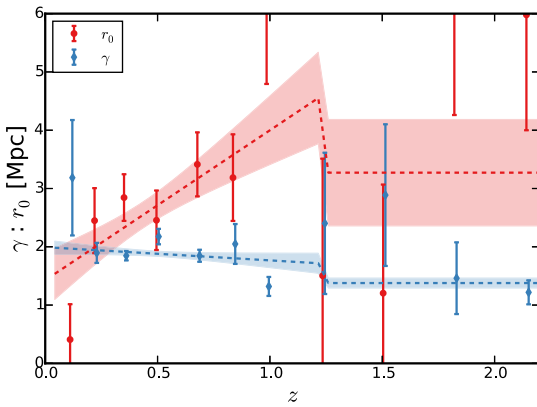


Figure C3. Relative clustering scalelength r_0 (red) and slope γ (blue) of power-law fits to the autocorrelation functions as a function of redshift in the COSMOS spec- z catalogue. The dashed lines show parametric fits to the data, consisting of a linear function for $0 < z < 1.2$ and a constant at $z > 1.2$.

Due to observational effects, a spec- z sample might show sudden breaks in its properties at certain redshifts. For example, the zCOSMOS sample changes abruptly at a redshift of $z \sim 1.2$, where the main features which are used for redshift measurement leave the optical window, and only certain types of galaxies can still be detected. This makes the interpolation harder and requires a judicious choice of model to describe the redshift dependence of the galaxy bias, which we capture through the free variables r_0 and γ . After some experimentation, we adopt a two-part model for the redshift dependence of these parameters (Fig. C3) in the COSMOS field: a linear dependence from $0 < z < 1.2$ and a constant at $z > 1.2$. For DEEP2, we use a linear relation for both parameters in the range of $0.5 < z < 1.5$.

The estimation of the autocorrelation function for the photometric sample is even more problematic. If the photometric selection yields a single-peaked true redshift distribution, the galaxy bias can be corrected for following the same methodology as the spec- z analysis (Schmidt et al. 2013). However, photo- z selections tend to yield highly non-Gaussian true redshift distributions with multiple peaks. Measuring the angular autocorrelation function of such a sample yields a projected mix of multiple autocorrelation functions of galaxies at different redshifts. Unfortunately, the galaxies in the multiple peaks of the true redshift distribution are typically of different types, with different biases. This mix of galaxy populations in photo- z tomographic bins is an inherent problem of the clustering redshift recovery method.

The importance of correcting for the galaxy bias is shown in Fig. C4, where the raw redshift recovery (i.e. just the amplitude of the cross-correlation function) is compared with the final bias-corrected redshift distribution for COSMOS. The correction for the galaxy bias, proposed by Newman (2008), essentially tilts the redshift distribution around some pivot redshift. We find that the amplitude of the high- z outlier populations – and hence also the amplitude of the resulting shear correlation function – is sensitive to this correction.

We do not further quantify the systematic error in the CC distributions from the effects discussed above since the weighted direct calibration (DIR) has a significantly higher precision (see Fig. C1). In the future when the overlapping area with deep spectroscopic surveys will increase, cross-correlation techniques will become competitive with other approaches of photo- z calibration, and it will become mandatory to model, estimate, and correct for these

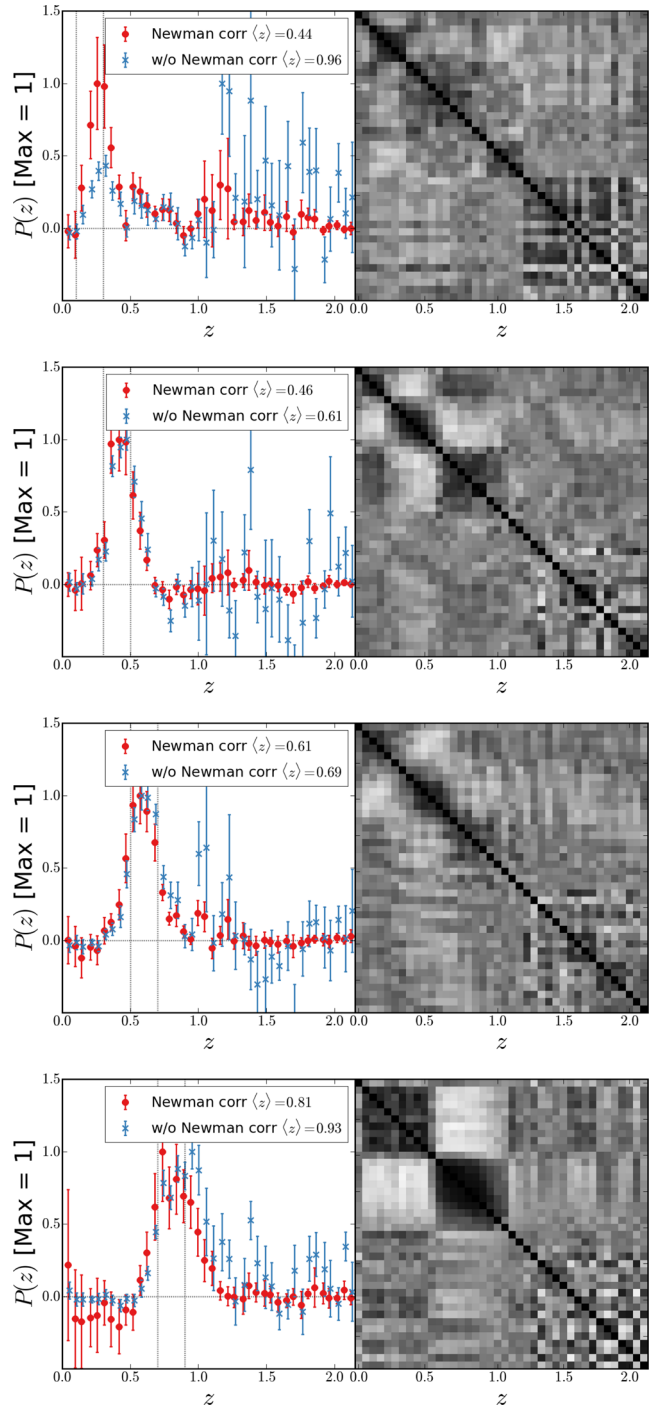


Figure C4. Redshift distribution recovery as determined by the cross-correlation technique in the COSMOS field. Left-hand panels: recovered redshift distributions of the four tomographic bins before (blue crosses) and after (red circles) correction for the galaxy bias. The z_B limits of each tomographic bin are indicated by vertical lines. Right-hand panels: correlation matrices of the red data points with white corresponding to a value of $\text{corr}_{ij} = -1$ and black to $\text{corr}_{ij} = 1$. Significant correlations are introduced by the bias correction. Note that these are not the final redshift distributions from this method: To generate those, we combine similar estimates from DEEP2 with COSMOS in an optimally weighted way.

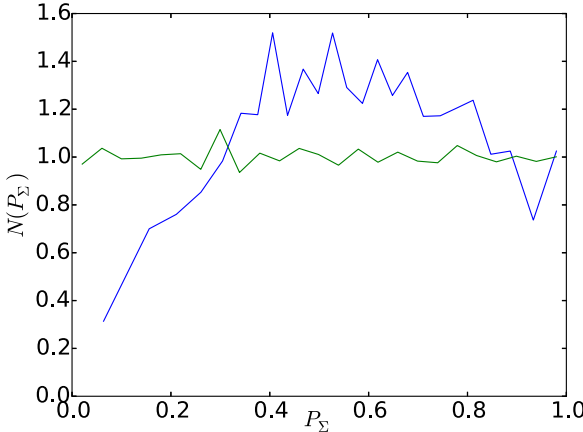


Figure C5. Distribution of P_Σ before (blue) and after (green) recalibration with the method by Bordoloi et al. (2010).

uncertainties. The unknown bias of an outlier population might be the ultimate limit to the accuracy of this method. The required measurement of precise selection functions for the spectroscopic and photometric samples will also pose a formidable challenge.

C3.3 Recalibration of the photometric $P(z)$ (BOR)

The main criterion for quality control in the photo- z recalibration method by Bordoloi et al. (2010) is the shape of the $N(P_\Sigma)$ (equation 1), which should be flat after a successful recalibration. In Fig. C5, this distribution is shown before and after the application of the method. As can be seen, the distribution of P_Σ is indeed flat after recalibration of the $P(z)$. A more in-depth study of systematic effects of this technique can be found in Bordoloi et al. (2012). We do not explore this method further in the present analysis.

C4 Galaxy-galaxy-lensing shear-ratio test

Assuming a fixed cosmology, there is a clear prediction for the lensing signal around galaxies (GGL), where the amplitude depends on mass and cosmology, and the signal should scale for sources in the different tomographic bins, given their $n(z)$. Here we test this redshift scaling with lenses with spectroscopic redshifts from BOSS (Alam et al. 2015) and from GAMA (Driver et al. 2011). This ‘shear-ratio’ test (Jain & Taylor 2003; Kitching et al. 2015; Schneider 2016) is similar to the tests described in Heymans et al. (2012) (see section 6 and fig. 12 of that paper) and Kuijken et al. (2015) (see section 5.2 and fig. 18 of that paper). As the GGL signal is rather insensitive to the choice of cosmology, this analysis can be used to verify the redshift distributions and the redshift scaling of the shear calibration correction m (equation D3).

For three lens samples: BOSS LOWZ with $0.15 < z_l < 0.43$, BOSS CMASS with $0.43 < z_l < 0.7$, and GAMA selected with $z_l < 0.2$, we measure the azimuthally averaged tangential shear γ_t around the lenses, in bins of angular separation. We make four measurements for each lens sample, using the KiDS-450 source galaxies from each of the four tomographic bins used in our cosmic shear analysis (see Table 1). The measured GGL signal is presented in Fig. C6, where, as expected, we see γ_t increasing with the redshift of the source galaxies. Note that the SNR when using sources from the first tomographic bin with the CMASS lenses is higher than for sources in the second and third bins because of the high- z tail of the DIR redshift distribution for the first bin.

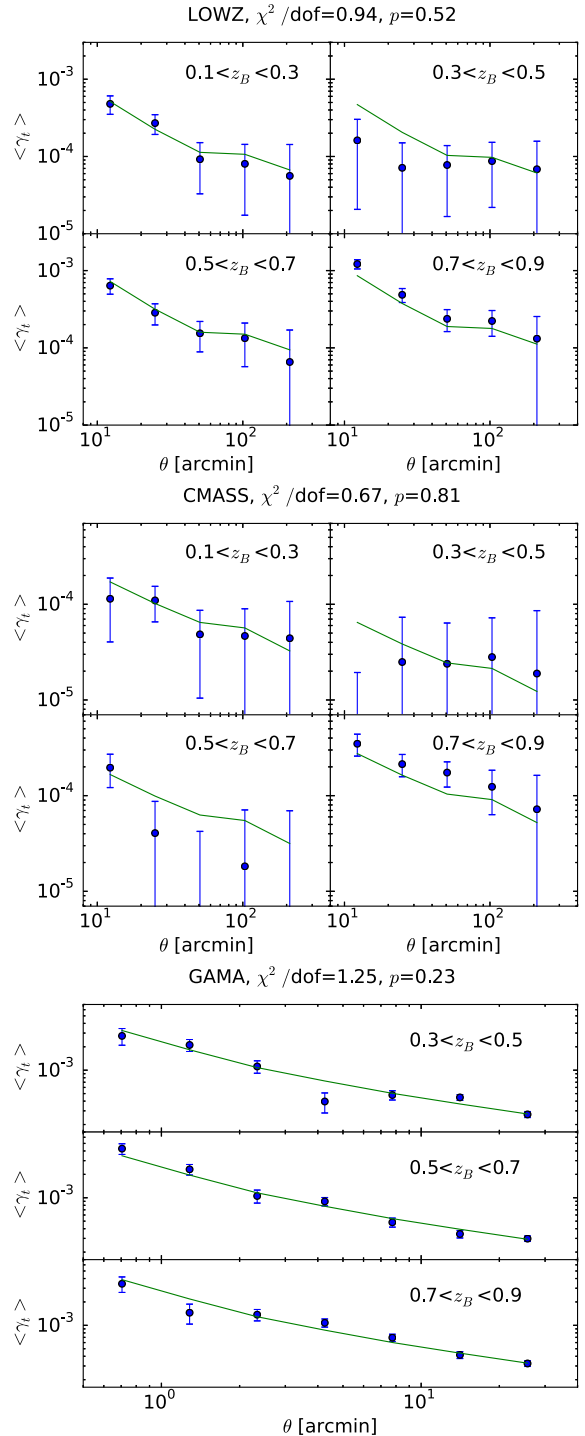


Figure C6. GGL signals using three lens samples: BOSS LOWZ (upper panel) and BOSS CMASS (middle panel) and GAMA galaxies with $z_l < 0.2$ (lower panel). The GGL signal is measured using sources in the different tomographic bins (as labelled). Shown is the measured tangential shear and a best-fitting lens model which leaves the amplitude at each angular scale free but constrained by the lensing efficiency β (see equation C3) for the different tomographic bins, given their DIR redshift distributions. For the BOSS samples which overlap with most tomographic bins in redshift, we only show the large scales where lens-source clustering is unimportant. For the GAMA sample with $z_l < 0.2$, we show the small-scale signal for the second, third, and fourth tomographic bins, which do not overlap significantly with the lenses in redshift. The goodness of fit is listed in each panel label.

We fit a maximally flexible lens model to all data points of one lens sample simultaneously, in which we leave the amplitudes at each angular scale free (five angular scales in the BOSS analyses and seven in the GAMA analysis). We compare the model with the data by multiplying by the appropriate predictions of the lensing efficiency β in each tomographic bin:

$$\beta = \int_0^\infty dz_l n_l(z_l) \int_{z_l}^\infty dz_s n_s(z_s) \frac{D(z_l, z_s)}{D(0, z_s)}, \quad (\text{C3})$$

where $D(z, z')$ is the angular diameter distance between redshifts z and z' , $n_l(z)$ is the redshift distribution of the lenses, and $n_s(z)$ is the redshift distribution of one of the source samples. This test is independent of any properties of the lens sample and hence represents a clean shear-ratio test. For BOSS, we use a covariance matrix for the correlated γ_t measurements estimated from the simulated mock catalogues described in Section 5.2. For GAMA, where we focus on small-scale correlations, we use an analytical covariance matrix, as described in Viola et al. (2015). The resulting best-fitting models give p -values of ca. 50 and 80 per cent for the LOWZ and CMASS samples, respectively, and ca. 20 per cent for GAMA, indicating that the scaling of the observed GGL signal is fully consistent with the expectations, given the redshift distributions estimated with the DIR technique.

Note that we choose different angular scales for the BOSS and GAMA measurements, and that for the GAMA analysis, we do not measure the GGL signal for the lowest tomographic bin. This is because for the BOSS lenses, there is significant redshift overlap between the lens samples and most of the tomographic bins. As these BOSS galaxies are strongly biased, we expect to find a significant dilution of the GGL signal at small scales; the galaxies at these close separations are more likely to be clustered with the lens such that the $n(z)$ for our source sample becomes θ dependent. This effect is similar to the dilution seen in cluster-lensing studies, where it is usually corrected for via a multiplicative boost factor (see e.g. Hoekstra et al. 2015). While, in principle, one could estimate a similar correction for the shear-ratio test shown here, such an analysis lies beyond the scope of this paper and would introduce new unknowns. Instead, we perform the GGL analysis for our BOSS sample only at large θ where the dilution effect is minimal because the multiplicative boost factor goes to unity (Hoekstra et al. 2015).

In order to take advantage of the high S/N at small angular scales to provide a more stringent test, and to avoid additive systematics which could, in principle, bias the large-scale results,¹³ we analyse the lowest GAMA redshift sample with $z_l < 0.2$ in order to reduce redshift overlap with the second, third, and fourth tomographic bins (see Fig. 2). With this GAMA selection, lens–source clustering should be negligible, given the DIR $n(z)$ allowing us to use the high-S/N small angular scales for a clean shear-ratio test.

In addition to the DIR analysis presented here, we also analysed the alternative redshift distributions described in Section 3 (BPZ, BOR, and CC), which we find to pass this test with similar p -values. Evidently, this test is not sensitive enough to discriminate between these different options.

In order to check the constraining power of our shear-ratio test, we deliberately swap the redshift distributions of the lenses and sources

¹³ We apply an empirical c -correction in our BOSS GGL analysis by subtracting the tangential shear signal around random points from the actual tangential shear around the lens galaxies (see e.g. van Uitert et al. 2016). This correction is not necessary for our GAMA measurements as we use small scales only.

in the modelling. While somewhat arbitrary, this should yield a model which is incompatible with the measurements. Indeed, we find extremely low p -values ($p \lesssim 10^{-4}$), allowing us to conclude that this shear-ratio test is meaningful.

APPENDIX D: GALAXY SELECTION, SHEAR CALIBRATION AND TESTS FOR SYSTEMATICS

In this appendix, we document the more technical aspects of the KiDS-450 shear measurement, including object selection, multiplicative and additive shear calibration corrections, and a range of systematic error analyses.

We create an object-detection catalogue using SExtractor with a low detection threshold (Bertin & Arnouts 1996). This catalogue contains ~ 30 objects arcmin $^{-2}$ and is used as the input catalogue for *lensfit*. In Sections D1 and D2, we discuss the object selection which reduces this object catalogue down to 11.5 galaxies arcmin $^{-2}$ with accurate shear measurements, and an effective number density of $n_{\text{eff}} = 8.53$ galaxies arcmin $^{-2}$. This level of reduction is similar to CFHTLenS (see e.g. fig. 3 of Duncan et al. 2014). It reflects our choice to use a very low source detection threshold in the original construction of the object catalogue, using a set of criteria measured by *lensfit* to decide which objects can then be used for accurate shear measurement. The alternative of imposing a higher S/N cut at the object-detection stage could result in a galaxy selection bias (see e.g. Fenech Conti et al. 2016).

D1 lens FIT selection

Apart from the ellipticity and associated weight, *lensfit* also returns a number of extra parameters (see table C1 of Kuijken et al. 2015), including an estimate of the galaxy scalelength, and a *fitclass* parameter, which encodes the quality of the fit. Using this information, we filter the *lensfit* output to remove sources with unreliable ellipticities, as follows.

Our initial selection requires a non-zero *lensfit* weight, which automatically removes the following:

- (i) objects identified as point-like stars (*fitclass* = 1);
- (ii) objects which are unmeasurable, usually because they are too faint (*fitclass* = -3);
- (iii) objects whose marginalized centroid from the model fit is farther from the SExtractor input centroid than the positional error tolerance of 4 pixels (*fitclass* = -7);
- (iv) objects for which insufficient data are found, for example, if they fall near the edge of an image, or a defect (*fitclass* = -1).

We further cut the following sources out of the catalogue:

- (v) objects for which the best-fitting galaxy model fit has a reduced $\chi^2 > 1.4$, indicating that they are poorly fitted by a bulge plus disc galaxy model (*fitclass* = -4), this cut removing 0.1 per cent of the objects outside the masked regions;
- (vi) objects that are brighter than the brightest magnitude in our image simulations (*catmag* ≤ 20);
- (vii) probable asteroids or binary stars (see Section D2);
- (viii) potentially blended sources, defined to have a neighbouring object within a contamination radius of 4.25 pixels from the galaxy's SExtractor centroid¹⁴;

¹⁴ Note that this selection is slightly stricter than the fiducial *fitclass* = -6, which keeps all objects with a contamination radius > 4 pixels. The

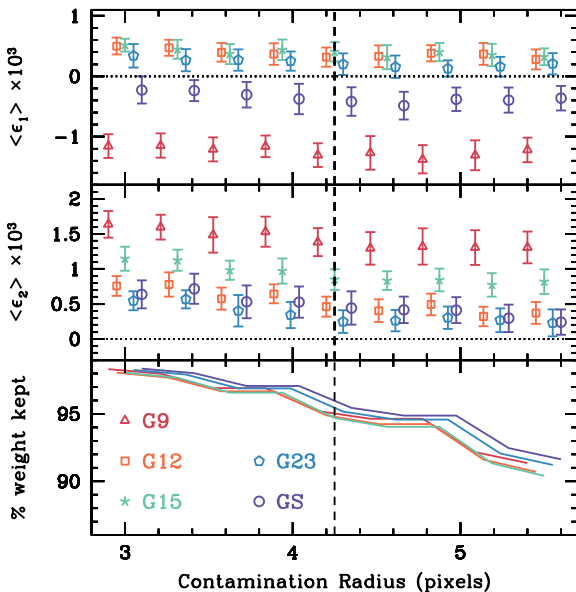


Figure D1. Criterion for masking of neighbours: the additive calibration bias as measured from the weighted average ellipticity ϵ_1 (upper panel) and ϵ_2 (middle panel), as a function of the minimum allowed contamination radius. The amplitude of the bias is shown for each of the five KiDS-450 patches (G9, G12, G15, G23, and GS), with points slightly offset along the horizontal axis for clarity. The lower panel shows the decreasing effective number density of objects as the contamination radius cut increases. Our chosen contamination radius cut of >4.25 pixels is shown in dashed.

(ix) objects classified as duplicates (`fitclass = -10`). These objects are identified during the de-blending analysis when `lensFIT` builds a dilated segmentation map that is used to mask out a target galaxy's neighbours. A very small fraction of targets has another input catalogue galaxy within its pixel region, owing to differing de-blending criteria being applied in the SExtractor catalogue generation stage and the `lensFIT` image analysis. In these cases `lensFIT` uses the same set of pixels to measure both input galaxies, which leads to the inclusion of two correlated, high-ellipticity values in the output catalogue. We therefore flag such cases and exclude them from subsequent analysis.

In contrast to earlier analyses, we retain objects which are large galaxies that overfill the postage stamp size of 48 pixels (`fitclass = -9`) in order to avoid ellipticity selection bias in the brightest galaxy sample: For a fixed major-axis scalelength, such a cut would have preferentially removed galaxies oriented in the $\pm\epsilon_1$ direction. Fenech Conti et al. (2016) also recommend removing objects which have a measured `lensFIT` `scalelength` smaller than 0.5 pixels. This selection represents only 0.01 per cent of the weighted galaxy population and we did not apply this cut for our main analysis. We have, however, verified that making this additional selection did not change our results in terms of the measured ξ_{\pm} in Section 6, the measured additive calibration terms in Section D4 or the measured small-scale B modes in Section D6.

The contamination radius deblending threshold was optimized to maximize the number density of galaxies whilst minimizing systematic errors. Fig. D1 shows the additive calibration bias, as measured from the weighted average ellipticity. The additive bias

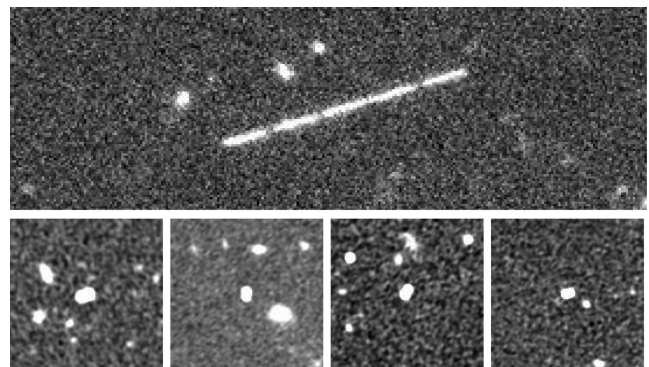


Figure D2. Examples of contaminating high-ellipticity objects which we filter out of the catalogues. Upper panel: an asteroid in one of the co-added images in patch G12. Lower panel: four examples of bright, blended binary stars. The lower images are PSF-Gaussianized, to highlight the compact nature of these point sources.

is found to slightly increase in amplitude as the minimum allowed contamination radius decreases below a contamination radius cut of 4.25 pixels. The lower panel shows the effect of varying the de-blending selection criterion on the weighted number density. For GGL studies, which are less sensitive to additive biases, a less conservative contamination radius cut could be used to increase the number density of source galaxies by ~ 5 per cent.

D2 Removing artefacts

D2.1 Asteroids

Because the source detection catalogue is produced from stacked images, some moving objects enter the catalogue. Some of our fields (particularly G12, but also G9 and G15) lie close to the ecliptic, and individual tiles can contain as many as 100 asteroids or more, which show up as a trail of dashes, one for each sub-exposure (Fig. D2). With typical proper motions of $30 \text{ arcsec } h^{-1}$, asteroids appear very elongated on our 6-min r -band sub-exposures, and so enter the catalogue of resolved sources with high-weight `lensFIT` shapes. Moreover, asteroids move predominantly along the ecliptic, making them a population of coherent, bright, and very elliptical sources which biases our ellipticity correlation function. When the segments of the trail due to the different sub-exposures are deblended, the same object may enter the catalogue up to five times, further increasing the impact of this contamination.

Eliminating the asteroids from the catalogue would ideally be done by comparing individual sub-exposures. For the present analysis, however, we instead use the fact that they show up in the multicolour catalogue with very characteristic colours: They are bright in the r -band detection image but essentially undetected in the other bands (because in those images they are no longer inside the photometric aperture at their detected position). The BPZ photometric redshift estimates of asteroids with such erroneous ' r -only' photometry are found to lie almost exclusively within the second tomographic bin with $0.3 < z_B < 0.5$.

To identify potential asteroids, we define an ' r -peakiness' colour, $r_{pk} = \min(g - r, i - r)$,

and determine an optimal cutoff value which maximizes the number density of galaxies whilst minimizing systematic errors. Fig. D3 shows the additive calibration bias, as measured from the weighted average galaxy ellipticity with a photometric redshift in the range of

method used to determine a contamination radius for each object is discussed in section 3.7 of Miller et al. (2013).

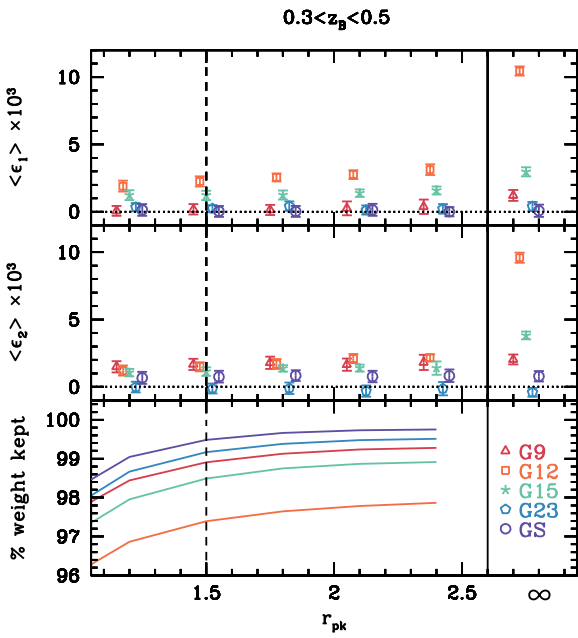


Figure D3. Asteroid selection criterion: the additive calibration bias for objects with $0.3 < z_B < 0.5$, measured from the weighted average ellipticity ϵ_1 (upper panel) and ϵ_2 (middle panel), as a function of the maximum allowed colour r_{pk} (equation D1). The amplitude of the bias is shown for each of the five KiDS-450 patches (G9, G12, G15, G23, and GS), with points slightly offset along the horizontal axis for clarity. The rightmost point in each panel shows the weighted average ellipticity measured for the full galaxy sample with no colour selection applied. The lower panel shows how the effective number density of objects increases with the colour threshold. Our chosen asteroid selection criterion removes galaxies with $r_{pk} > 1.5$, shown dashed.

$0.3 < z_B < 0.5$. The additive bias is found to increase in amplitude as the maximum allowed colour r_{pk} increases above 1.5. Including all objects without any asteroid de-selection can result in additive biases in the second tomographic bin as large as ~ 0.01 for the G12 patch, which lies closest to the ecliptic. This bias is reduced to ~ 0.001 after the objects with $r_{pk} > 1.5$ are removed from the sample. We apply this selection to all tomographic bins.

Fig. D4 shows the distribution of G12 objects with $r_{pk} > 1.5$ in polar ellipticity coordinates ($|e|, \arg(e)$). This distribution supports the theory that these artefacts are asteroids as the majority of objects excluded with this cut are highly elliptical, with a preferred orientation.

D2.2 Binary stars

Unresolved binary stars are another source of highly elliptical objects in our catalogues. To identify parts of parameter space where they dominate, we use the $(g - r, r - i)$ colour–colour diagrams. Any selection that predominantly picks out stars will show the characteristic stellar locus, whereas galaxy samples will not. For a very high ellipticity ($e > 0.8$), it turns out that objects with the measured scalelength

$$r_d < 0.5 \times 10^{(24.2-r)/3.5} \text{ pixels} \quad (\text{D2})$$

have stellar colours, whereas larger objects do not (Fig. D5). We therefore apply this cut to our source catalogues as well. The fraction of sources (*lensfit* weight) removed this way lies between 0.07 (0.05) and 0.33 (0.18) per cent, depending on the galactic latitude

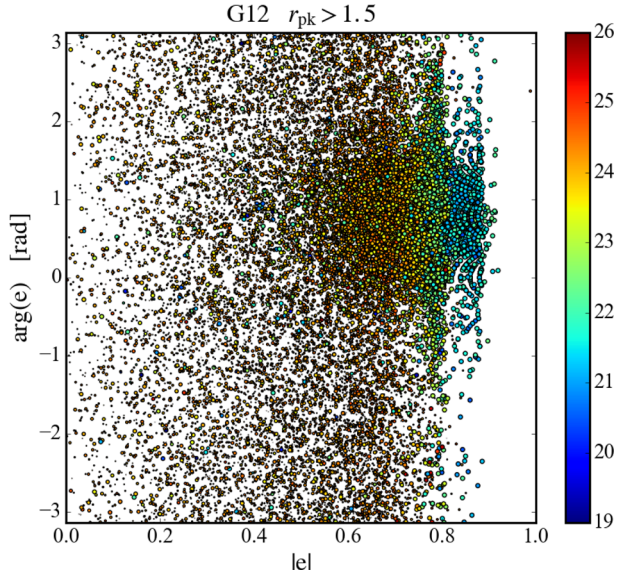


Figure D4. Sources from patch G12 which fail the asteroid cut, plotted in polar ellipticity coordinates $(|e|, \arg(e))$. These sources are at least 1.5 mag brighter in r than in g and in i . Each symbol is colour-coded by the catalogue r magnitude, and the symbol size is proportional to *lensfit* weight.

of the patches. Unlike asteroids, these binary stars do not have a preferred orientation, so their inclusion in the galaxy catalogue would generate a multiplicative and not an additive bias. A few examples of bright objects eliminated by this cut are shown in Fig. D2.

D3 Multiplicative shear calibration from image simulations

We use the ‘self-calibrating’ version of *lensfit* to measure galaxy shapes, quantifying any residual bias after self-calibration through the analysis of a suite of simulated images resembling the KiDS r -band images. We present a summary here and refer the reader to Fenech Conti et al. (2016) for a detailed description of the simulations and the analysis pipeline.

We use the publicly available GALSIM software (Rowe et al. 2015) to simulate 416 deg^2 of data, containing approximately 54 million galaxies, of which 16 million have a non-vanishing *lensfit* weight. This number of galaxies, in combination with a shape noise cancellation scheme, allows us to achieve a statistical precision on the measurement of the shear multiplicative bias of ~ 0.003 , which is more than a factor of 3 smaller than the requirements described in Appendix A. We simulate individual 1-deg^2 tiles with the same resolution, focal plane footprint and five-point dither strategy as the KiDS observations (see de Jong et al. 2015). The individual sub-exposures are co-added using SWARP (Bertin 2010). The r -band magnitude distribution of the galaxies is chosen such that it matches the number counts measured in KiDS-DR1/2, and we use deep *HST* observations from GEMS (Rix et al. 2004) and UVUDF (Rafelski et al. 2015) to extend the distribution to the 28th magnitude in order to account for the effect of undetected sources in the estimation of the shear bias (Hoekstra et al. 2015; Bruderer et al. 2016). The size distribution as a function of magnitude is described in Kuijken et al. (2015). Galaxies are modelled as a linear combination of a de Vaucouleurs profile for the bulge and an exponential profile for the disc. The bulge-to-total flux ratio, the fraction of bulge-dominated galaxies and the galaxy ellipticity distribution are matched to the *lensfit* prior (Miller et al. 2013).

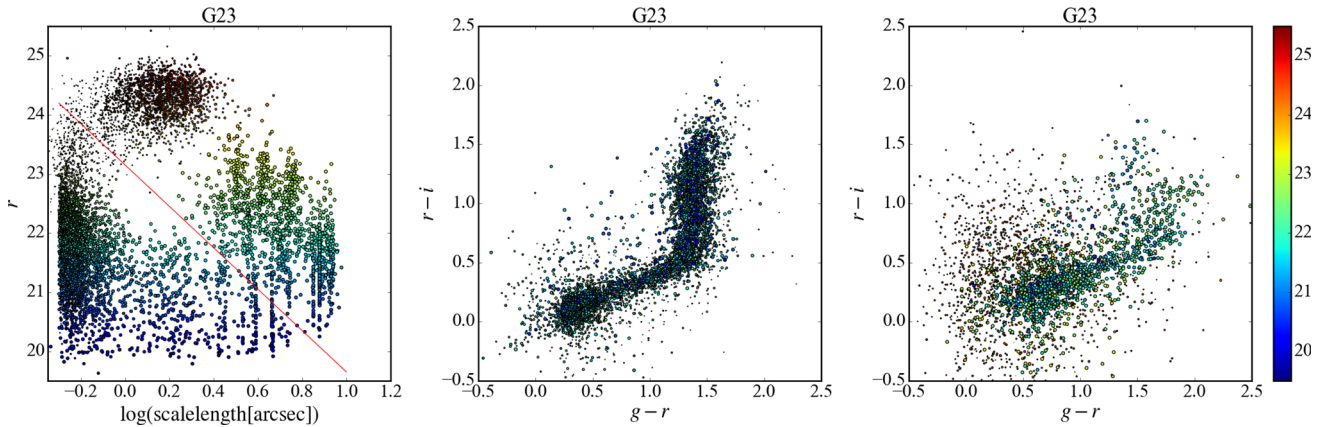


Figure D5. Illustration of the cuts on high-ellipticity ($e > 0.8$) objects to separate binary stars from galaxies, for one of the five patches (G23). Left-hand panel: scalelength versus r -magnitude diagram with the cut indicated. Middle panel: gri colour–colour diagram for objects below the cut. Right-hand panel: same, for objects above the cut. Each symbol is colour-coded by the catalogue r magnitude, and the symbol size is proportional to the *lensfit* weight.

The position of the galaxies is random, hence allowing us to assess the impact of blending on the shear measurements but not the impact of clustering. In order to reduce the impact of shape noise in the shear measurement, we created copies of each simulated tile, in which all galaxies are rotated by 45° , 90° , and 135° .

Each tile (and its three rotated copies) is simulated eight times with a different constant shear value applied to the galaxies. The shear values are chosen such that they have the same magnitude, $|g| = 0.04$, but they are rotated at eight evenly spaced position angles.

The galaxies are convolved with a PSF, described by a Moffat profile. The PSF is spatially constant in each simulated tile but different in each of the five sub-exposures. The parameters of the Moffat profile are chosen such that the PSF size and ellipticity distributions in the simulations are representative of the variations measured on KiDS-DR1/2. In total, we simulate 13 PSF sets. We include stars in the simulations, which are a perfect representation of the PSF. Their magnitude distribution is derived from the Besançon model (Robin et al. 2003; Czekaj et al. 2014) for stars in the range of $20 < r < 25$. Bright stars are not included in the simulations as they are masked in the real data.

We create an object-detection catalogue using SExtractor (Bertin & Arnouts 1996) to process the co-added simulated dithered exposures with the same configuration as used in the analysis of the real KiDS data. The resulting detection catalogue is used as the input to *lensfit*. For each PSF set and for each of the eight input shear values, we measure the shear components γ_j^{obs} by averaging the ellipticities of all simulated galaxies in the four rotated versions of each tile, using the recalibrated weights calculated by *lensfit*.

Following Heymans et al. (2006a), we parametrize the shear bias in terms of a multiplicative and an additive term:

$$\gamma_j^{\text{obs}} = (1 + m_j) \gamma_j^{\text{true}} + c_j. \quad (\text{D3})$$

We characterize the multiplicative and additive biases as a function of the galaxy S/N and ‘resolution’ (\mathcal{R}), defined as

$$\mathcal{R} := \frac{r_{\text{PSF}}^2}{(r_{ab}^2 + r_{\text{PSF}}^2)}, \quad (\text{D4})$$

where $r_{ab} = \sqrt{ab}$ is the circularized size of an object derived from the *lensfit* measured semi-major axis a and semi-minor axis b of each galaxy, and r_{PSF}^2 is the corresponding size of the PSF.

In order to derive the multiplicative bias in the four KiDS-450 tomographic bins, we resample the image simulations such that the

distributions of simulated galaxy properties match those of the real galaxy sample in each tomographic bin. We do this by means of a 2D k -nearest neighbour search of the simulated ($S/N, \mathcal{R}$) surface for all KiDS galaxies in each of the four tomographic bins used in this paper. As a result of the resampling, each simulated galaxy is assigned an additional weight, which is the number of times a real KiDS galaxy has been matched to it. This procedure is very similar to the DIR method used to calibrate the galaxy redshift distribution (see Section 3). We measure the shear from the resampled simulations as a weighted average of the measured galaxy ellipticities, where the weight is the product of the ‘resampling’ weight and the *lensfit* weight. This is done for all four tomographic bins. We finally compute the multiplicative and additive shear biases by means of a linear regression (see equation D3) between the measured shear and the true input shear used in the simulation.

The average multiplicative and additive biases measured in each of the four tomographic bins are very small and similar in amplitude for the two shear components. In particular, we find $m = [-0.0131, -0.0107, -0.0087, -0.0217] \pm 0.01$ and $c = [3.2, 1.2, 3.7, 7.7] \pm 0.6 \times 10^{-4}$. The error on the multiplicative bias accounts for systematic and statistical uncertainties ($\sigma_{\text{stat}} = 0.003$). This systematic uncertainty comes from differences between the data and the simulations and choices in the bias estimation. It also allows for additional sources of bias which might arise from the mismatch between the galaxy model assumed by *lensfit* and the true galaxy morphology. Known as ‘model bias’ (Voigt & Bridle 2010), this effect is not reflected in our image simulation analysis, which models and analyses galaxies with a two-component Sérsic profile. Model bias is expected to be negligible in comparison to the statistical noise of KiDS-450 (Kacprzak et al. 2014). Furthermore, in the GREAT3 challenge (Mandelbaum et al. 2015), the self-calibrating *lensfit* analysis of the image simulations created using true *HST* imaging suggests that the contribution from model bias is less than 0.01. The additive shear bias estimated from the simulations is not used to correct the shear measured from the data. An additive term is instead measured directly from the data, as described in Section D4. Hence, the error on the additive bias quoted above is only the statistical uncertainty set by the volume of the simulated data and does not include any systematic uncertainty.

As a way to validate our primary calibration strategy, we also adopt an alternative non-parametric approach in order to derive a multiplicative bias calibration which achieves the required level of accuracy given in Appendix A. This is similar to the method

employed in CFHTLenS (Miller et al. 2013). We compute the multiplicative and additive biases on a 20 by 20 grid in S/N and \mathcal{R} , with the bin limits chosen such that each grid cell has an equal *lensFIT* weight, and we assign the average bias calculated in each cell to all the real galaxies falling inside that cell. This is done for each tomographic bin. We refer the reader to section 4.5 in Fenech Conti et al. (2016) for further details. As the additive bias we measure in the simulations is very small compared to the bias measured in the data (see Section D4 for a discussion), we do not apply any additive bias correction measured from the simulations to the data.

We find consistent results between both approaches, with differences in m of at most 0.003 (1σ) in some tomographic bins. In both cases, the residual biases as a function of PSF properties (pseudo-Strehl ratio, size and ellipticity) are consistent with zero.

Following Jarvis et al. (2016), we also use the image simulations to explicitly look at the print-through of the PSF shape in the galaxy shape by modelling the bias as

$$\gamma_j^{\text{obs}} = (1 + m_j)\gamma_j^{\text{true}} + \alpha_j e_j^* + c_j. \quad (\text{D5})$$

We find the average $|\alpha_j|$ in the four tomographic bins to be less than 0.02 for both components. We explore the sensitivity of the recovered calibration to changes in the intrinsic ellipticity distribution used in the simulations. We find that for reasonable variations the changes in the calibration are smaller than the errors.

D4 Empirical additive shear calibration

We parametrize calibration corrections to our *lensFIT* shear measurements in terms of an additive c and a multiplicative term m (following equation D3). For a sufficiently large source sample, where the average shear γ and intrinsic ellipticity ϵ^{int} average to zero: $\langle \gamma_i + \epsilon_i^{\text{int}} \rangle = 0$, the additive term can be measured directly with $c_i = \langle \epsilon_i \rangle$.

In Section D3, we review the KiDS image simulation analysis, which finds these terms to be very small (see Fenech Conti et al. 2016, for further details). This suite of image simulations is certainly the most sophisticated test of *lensFIT* to date, but there are a number of steps in the data acquisition, processing and analysis which are not simulated, including the following:

- (i) There are no image artefacts present, such as cosmic rays, asteroids, and binary stars.
- (ii) No astrometric shear is applied, which in the data analysis is derived using stars and subsequently corrected for in the model-fitting analysis.
- (iii) The PSF model is determined from a set of known simulated stars, whereas the PSF model for the data derives from a stellar sample selected using the star–galaxy separation technique described in Kuijken et al. (2015).
- (iv) Galaxy morphology is limited to two-component bulge-plus-disc models.
- (v) The simulated CCDs have a linear response.

These higher level effects are not expected to significantly change our conclusions about the multiplicative calibration m from the image simulation analysis. They do, however, impact on the additive term c , as demonstrated, for example, in Appendix D2, where image artefacts from asteroids are shown to change the measured additive bias by an order of magnitude. It is therefore important to determine a robust empirical calibration scheme in order to correct for any sources of bias in the data which are not present in the image simulations. Previous calibration schemes provide a c correction per galaxy, by measuring the average ellipticity for samples of galaxies

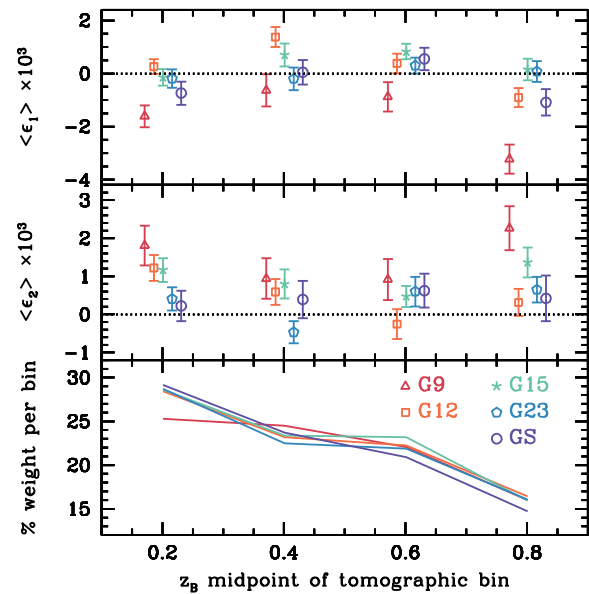


Figure D6. Empirical additive calibration: the average weighted ellipticity ϵ_1 (upper panel) and ϵ_2 (middle panel) for the four tomographic slices. The amplitude of the bias is shown for each of the five KiDS-450 patches; G9, G12, G15, G23, and GS, with points slightly offset on the horizontal axis for clarity. The lower panel shows the total weight of the galaxies in each tomographic slice as a fraction of the full survey weight. About 10 per cent of the effective weight in KiDS-450 lies outside the tomographic limits used in this analysis.

binned by their observed size, S/N, and the PSF Strehl ratio at the location of the galaxy (Heymans et al. 2012; Kuijken et al. 2015; Hildebrandt et al. 2016). We do not use this methodology for KiDS-450 because Fenech Conti et al. (2016) show that separating galaxies by their measured size and S/N introduces a significant selection bias which changes the distribution of ellipticities, which then impacts the shear deduced from the average ellipticity. The c -term measured by this method is therefore predominantly correcting for the selection bias introduced in its initial determination. Instead, we choose to determine an additive calibration correction c from the average weighted ellipticity of all galaxies per tomographic bin, and per KiDS-450 patch, as shown in Fig. D6. We find that the c -term is of the order of $\sim 10^{-3}$, differing between each tomographic bin and patch, with G9 showing the strongest bias. Errors are estimated from a bootstrap analysis.

Owing to the strong ellipticity selection biases which arise when binning the data by measurements of size and S/N (Fenech Conti et al. 2016), it is not possible to test whether the source of this additive bias derives from, for example, a population of small faint galaxies. We can, however, test the dependence of the additive bias on the observed position within the field of view and the number density of stars used to determine the PSF model (see e.g. van Uitert & Schneider 2016), in addition to testing the dependence on PSF size and ellipticity. We find no significant dependence of the additive bias with these quantities, which is consistent with the findings of the star–galaxy cross-correlation analysis presented in Section D5. We further explore the possibility of PSF contamination when the data are split into tomographic slices by fitting the following model to the data:

$$\epsilon_j = \gamma_j + \epsilon_j^{\text{int}} + \alpha_j e_j^* + c_j, \quad (\text{D6})$$

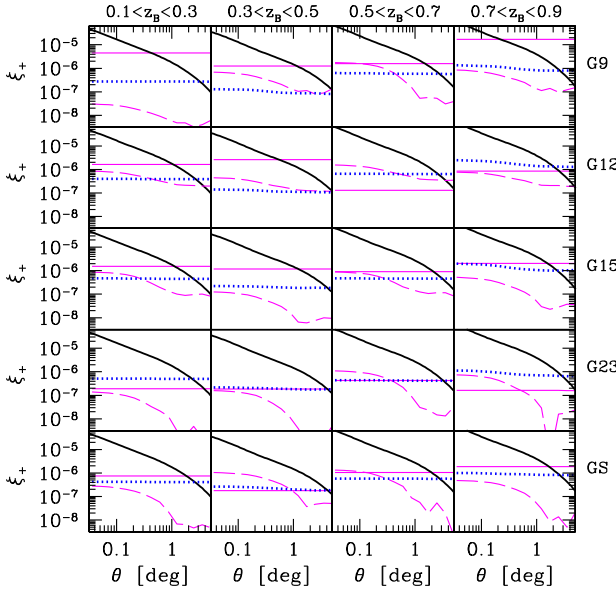


Figure D7. The systematic contribution to the two-point correlation function ξ_+ from the best-fitting α and c values, determined from each tomographic slice (increasing in redshift from the left-hand to right-hand side) and KiDS-450 patch (labelled from the top to bottom). The dashed line in each panel shows $\langle \alpha \epsilon^* \alpha \epsilon^* \rangle$ and the thin solid line shows $c_1^2 + c_2^2$, as determined from the data. This can be compared with the best-fitting cosmic shear signal from our primary analysis (thick solid line) and to the systematic contribution from the α and c predicted by the image simulation analysis of Fenech Conti et al. (2016) (dotted line).

where α_i and c_i are free parameters, with $i = 1, 2$, and ϵ^* is the measured PSF ellipticity. The fit is made to each tomographic slice and patch, assuming $\langle \gamma_i + \epsilon_i^{\text{int}} \rangle = 0$ in each sample. We find measurements of α to be uncorrelated with c , such that including or excluding the α term from our systematics model has little impact on our conclusions about c . We find that $\alpha_1 \simeq \alpha_2$ with the average α across the patches falling in the range of $-0.03 < \alpha < 0.02$ across the four different tomographic bins with an error ~ 0.01 . Fig. D7 shows the systematic contribution to the two-point correlation function ξ_+ from the best-fitting α and c values, determined from each tomographic slice and patch. The dashed line shows the PSF-dependent component of the systematics model¹⁵ ($\langle \alpha \epsilon^* \alpha \epsilon^* \rangle$). We find that it is more than an order of magnitude lower than the best-fitting cosmic shear signal (shown in thick solid). As α is found to be consistent with zero for the majority of tomographic slices and patches, we do not correct for this term in our analysis. In contrast, the purely additive $c_1^2 + c_2^2$ contribution to ξ_+ (shown thin solid) is significant, exceeding the expected cosmic shear signal on large scales. Therefore, we do correct for this term. For reference, the systematic contribution from the α and c determined from the image simulation analysis of Fenech Conti et al. (2016) is shown dotted and found to be similar to the measured systematics, with the exception of the G9 and G12 patches and the second tomographic bin in the G15 patch.

In GGL studies, it has become standard practice to measure the tangential shear around random positions, and subtract the measured ‘random signal’ from the GGL signal in order to remove additive

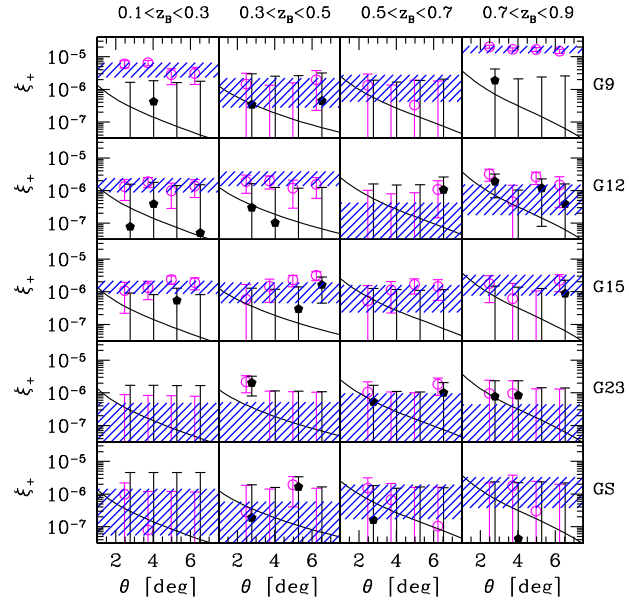


Figure D8. The large-scale two-point correlation function with $\theta > 2^\circ$ before (open symbols) and after (closed symbols) correcting each tomographic slice for the additive bias shown in Fig. D6. Each tomographic slice (increasing in redshift from the left-hand to right-hand side) and KiDS-450 patch (labelled from the top to bottom) is shown. The hashed region shows the amplitude of the correction and associated error. The cosmological signal (shown in solid) is expected to be consistent with zero on these scales.

systematic biases in the measurement. We seek a similar method for cosmic shear to validate our additive calibration strategy. There is no null signal, as such, but the cosmic shear signal on very large scales is expected to be consistent with zero within the statistical noise of KiDS-450. Fig. D8 shows the measured ξ_+ on angular scales $\theta > 2^\circ$, before (open symbols) and after (closed symbols) correcting each tomographic slice for the additive bias shown in Fig. D6. The hashed region shows the amplitude of that correction and associated error. After correction, the large-scale signal is consistent with zero, and with the best-fitting cosmological signal. This verifies the calibration correction. It also sets an upper limit on the angular scales which can be safely analysed for ξ_+ . We set this limit at 1° , where the measured amplitude of ξ_+ is more than an order of magnitude larger than the large-scale cosmic shear signal which is also subtracted when employing this empirical calibration strategy. On smaller scales of $\theta \sim 5$ arcmin, where the cosmic shear S/N peaks (see Fig. 3), this large-scale cosmic shear subtraction is completely negligible. Note that there is no equivalent upper θ limit for ξ_- . Additive terms do not typically contribute to the ξ_- statistic as for square geometries $\langle c_i c_j \rangle = \langle c_\times c_\times \rangle$.

D5 Star–galaxy cross-correlation

We measure the correlation between star and galaxy ellipticities to determine if any tiles exist in our sample with a significant residual contamination resulting from an imperfect correction for the PSF. We use the method described in Heymans et al. (2012) to assess the significance of galaxy–PSF shape correlations in order to identify problematic tiles. Previous surveys have used this strategy to flag and remove significant fractions of the data: 25 per cent (CFHTLenS; Heymans et al. 2012), 9 per cent (RCSLenS; Hildebrandt et al. 2016), and 4 per cent (KiDS-DR1/2; Kuijken et al. 2015).

¹⁵ We use the shorthand notation of Heymans et al. (2012), where $\langle ab \rangle$ indicates which two ellipticity measurements a and b are being correlated using the weighted data estimator in equation (2).

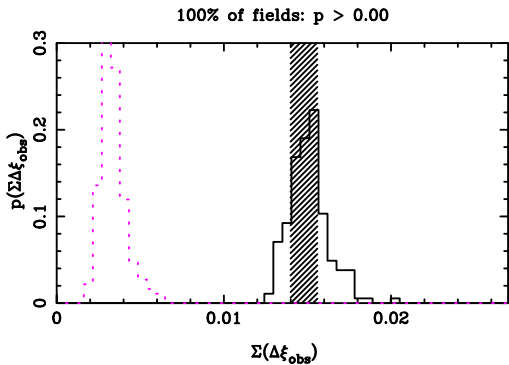


Figure D9. Amplitude of the star–galaxy shear cross-correlation statistic $\Delta\xi_{\text{obs}}$ summed over all KiDS-450 data tiles (hashed) and mock tiles (solid). The contribution from cosmic shear to this statistic is shown by the dashed histogram. In KiDS-450, we do not reject any tiles based on this test since the value of $\Sigma\Delta\xi_{\text{obs}}$ is fully consistent with the expectation from simulations which model chance alignments between galaxies and the PSF due to cosmic shear, shape noise, and shot noise.

Briefly, the method uses the fact that most galaxies in a tile have been observed in five different sub-exposures, with different PSFs. It assumes that intrinsic galaxy ellipticities average to zero, and uses the degree of shape correlation between the corrected galaxies and the PSF models in the different sub-exposures to estimate the amount of PSF print-through in the tile’s measured shear field. This PSF contamination is then cast in the form of a non-negative contamination, $\Delta\xi_{\text{obs}}$, to the two-point galaxy ellipticity correlation function in that tile (see equation 10 in Heymans et al. 2012). Mock shear maps with realistic noise properties are used to generate distributions of this statistic in the absence of systematic errors, in order to assess the significance of the measured values.

The hashed bar in Fig. D9 shows the value of the $\Delta\xi_{\text{obs}}$ statistic, measured in each 1-deg² tile, and then summed over the full KiDS-450 sample. For comparison, the histogram in Fig. D9 shows the distribution of $\Sigma\Delta\xi_{\text{obs}}$ measured for 184 systematic-free mock realizations of the KiDS-450 survey. We find that the star–galaxy cross-correlation measured in the data agrees well with the signal measured from our systematic-free mocks.

This agreement is further explored in Fig. D10. For each tile, we determine the probability $p(U = 0)$ which determines how likely it is that its measured $\Delta\xi_{\text{obs}}$ is consistent with zero systematics (see Heymans et al. 2012 for details). Fig. D10 shows how the measured cumulative probability distribution for the KiDS-450 tiles agrees well with a uniform distribution. As such, even the small handful of tiles with low $p(U = 0)$ are expected for a data set of this size. From this analysis, we conclude that, unlike previous surveys, we do not need to reject tiles. Evidently, the reduction in PSF-dependent noise bias achieved by the self-calibrating *lensfit*, combined with a benign PSF pattern, is of sufficiently high quality that there is no significant contamination by the PSF within the full KiDS-450 data set.

D6 E/B-mode decomposition

The main disadvantage of using the ξ_{\pm} statistic is the fact that it mixes curl-free gradient distortions (E mode) and curl distortions (B mode). The weak-lensing contribution to the B mode occurs only at small angular scales, $\theta < 1$ arcmin, mainly due to source redshift clustering (Schneider, van Waerbeke & Mellier 2002a). Separating the weak-lensing signal into E and B modes therefore provides a

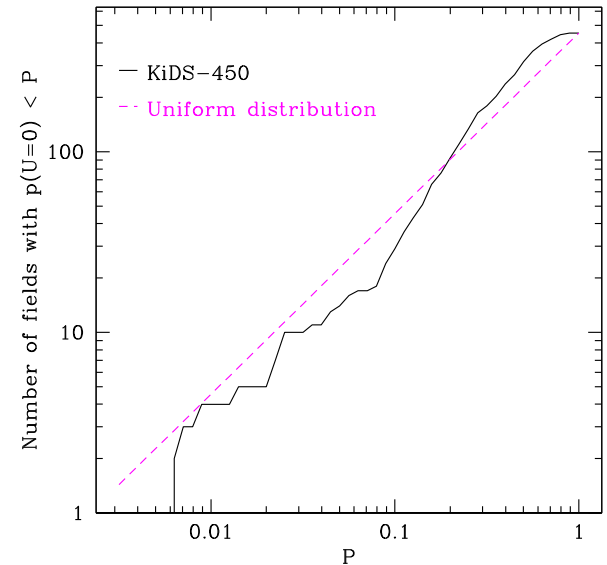


Figure D10. Cumulative probability distribution: the number of tiles with a probability $p(U = 0) < P$, where $p(U = 0)$ determines how likely it is that the measured $\Delta\xi_{\text{obs}}$ in each tile is consistent with zero systematics. The data agree well with the dashed line, which shows the cumulative probability for a uniform distribution.

stringent null-test. A non-zero B mode could arise from residual systematics in the shear measurement method, intrinsic ellipticity selection biases from the object detection stage or the photometric redshift selection, or from the intrinsic alignment of nearby galaxies (see e.g. Troxel & Ishak 2015; Joachimi et al. 2015, and references therein).

Schneider et al. (2010) derive a set of complete basis functions, called COSEBIs, which optimally combine different angular scales from the ξ_{\pm} measurement to produce a pure E/B separation. When applied to the CFHTLenS data, the COSEBIs analysis revealed significant high-order B modes when the data were separated into different tomographic bins (Asgari et al. 2017). As these tomographic B modes were not seen when using alternative E/B decomposition methods (Kitching et al. 2014), we consider COSEBIs to provide the most stringent B-mode null-test. A significant measurement of a COSEBIs B mode, however, reveals only the presence of a non-cosmological signal in the data. It does not inform us how, or indeed whether, that signal biases cosmological constraints from a ξ_{\pm} analysis, nor does it inform on the origin of the non-cosmological signal. For the purposes of this paper, we therefore investigate the E- and B-type correlators $\xi_{\text{E/B}}$ proposed by Crittenden et al. (2002), which are closely related to our chosen ξ_{\pm} statistic. These are given by

$$\xi_{\text{E}}(\theta) = \frac{\xi_{+}^{\text{obs}}(\theta) + \xi'(\theta)}{2} \quad \text{and} \quad \xi_{\text{B}}(\theta) = \frac{\xi_{+}^{\text{obs}}(\theta) - \xi'(\theta)}{2}, \quad (\text{D7})$$

where

$$\xi'(\theta) = \xi_{-}^{\text{obs}}(\theta) + 4 \int_{\theta}^{\infty} \frac{d\vartheta}{\vartheta} \xi_{-}^{\text{obs}}(\vartheta) - 12\theta^2 \int_{\theta}^{\infty} \frac{d\vartheta}{\vartheta^3} \xi_{-}^{\text{obs}}(\vartheta), \quad (\text{D8})$$

and ξ_{\pm}^{obs} is the observed two-point shear correlation function. In the absence of B-mode distortions, $\xi'(\theta) = \xi_{+}^{\text{obs}}(\theta)$ and $\xi_{+}^{\text{obs}}(\theta) = \xi_{\text{E}}$, that is, the observed shear correlation function is pure E mode.

Consider the toy model where any systematic contribution to the ellipticity measurement is uncorrelated with the true sheared

ellipticity ϵ^{true} , and adds linearly such that $\epsilon^{\text{obs}} = \epsilon^{\text{true}} + \epsilon^{\text{sys}}$. In the case where the contaminating systematic signal contributes equally to the tangential and cross distortions such that $\langle \epsilon_t^{\text{sys}} \epsilon_t^{\text{sys}} \rangle = \langle \epsilon_x^{\text{sys}} \epsilon_x^{\text{sys}} \rangle$, the systematics contribute only to the observed $\xi_+^{\text{obs}}(\theta)$ with

$$\xi_+^{\text{obs}}(\theta) = \xi_+^{\text{true}}(\theta) + \xi_+^{\text{sys}}(\theta) \quad \text{and} \quad \xi_-^{\text{obs}}(\theta) = \xi_-^{\text{true}}(\theta), \quad (\text{D9})$$

where $\xi_+^{\text{sys}} = \langle \epsilon_t^{\text{sys}} \epsilon_t^{\text{sys}} \rangle + \langle \epsilon_x^{\text{sys}} \epsilon_x^{\text{sys}} \rangle$. In this case, the observed $\xi_-^{\text{obs}}(\theta)$ is systematic-free such that $\xi'_-(\theta) = \xi_+^{\text{true}}(\theta)$ and

$$\xi_E(\theta) = \xi_+^{\text{true}}(\theta) + \frac{\xi_+^{\text{sys}}(\theta)}{2} \quad \text{and} \quad \xi_B(\theta) = \frac{\xi_+^{\text{sys}}(\theta)}{2}. \quad (\text{D10})$$

A measurement of a non-zero B mode could therefore be mitigated in the cosmological analysis as

$$\xi_+^{\text{true}}(\theta) = \xi_+^{\text{obs}}(\theta) - 2\xi_B(\theta), \quad (\text{D11})$$

but only if the originating systematic is thought to contribute equally to the tangential and cross distortions. This type of distortion would arise from random errors in the astrometry which are coherent over small scales, such that objects imaged in each exposure are not precisely aligned relative to one another. It is also typical of the KiDS-450 PSF distortion patterns, ϵ^* , where we find $\langle \epsilon_t^* \epsilon_t^* \rangle - \langle \epsilon_x^* \epsilon_x^* \rangle$ to be consistent with zero on all scales for both the PSF correlation and the PSF residual correlation function. Note that this is not necessarily the case for all camera PSFs (Hoekstra 2004).

If the B mode is thought to originate from small-scale random astrometric errors, or from KiDS-450 PSF distortions, then the mitigation strategy outlined above would be a reasonable approach to take. If the B mode is thought to originate from intrinsic galaxy alignments, however, this strategy would be ill-advised. The intrinsic galaxy alignment models and mocks which find significant B modes measure them to be less than $\sim 1/5$ th of the intrinsic alignment contribution to the E mode (Heymans et al. 2006b; Giahi-Saravani & Schäfer 2014). In contrast, the commonly used linear-alignment theory which we adopt to model the impact of intrinsic galaxy alignments (see Section 4.2) predicts B modes which contribute only to the sub-dominant ‘II’ term at roughly an order of magnitude lower than the ‘II’ E-mode signal (Hirata & Seljak 2004). Whichever intrinsic alignment model one chooses, mitigating its effects through equation (D10) would therefore fail. Our toy model also breaks down for systematics introduced through selection biases, where the systematic is likely to be correlated with the true sheared ellipticity ϵ . Selection biases could arise at the source extraction stage where, at the faintest limits, there is a preference to select galaxies oriented in the same direction as the PSF (Kaiser 2000) and galaxies which are correlated with the gravitational shear (Hirata & Seljak 2003). These selection biases can, however, be mitigated using a realistic suite of image simulations to calibrate the effect (see the discussion in Fenech Conti et al. 2016). Vale et al. (2004) show that non-equal E and B modes can be introduced where there is a variation in the source density across the survey, for example, from changes in seeing. The amplitude of this effect is, however, significantly smaller than the statistical noise in KiDS-450.

In previous cosmic shear analyses, significant detections of B modes were mitigated using different strategies. Benjamin et al. (2007) detected significant B modes and proposed to increase the uncertainty on the E-mode measurement by adding the measured B modes in quadrature. A similar strategy was used by Jee et al. (2013). An alternative method removes angular scales from the analysis where the B modes are found to be non-zero (Massey et al. 2007; Fu et al. 2008). This strategy requires that the systematic distortion has the same angular dependence for the E and B modes.

Becker et al. (2016) report zero B modes for the DES-SV data based on a Fourier band-power analysis. This conclusion relies on the assumption that small-scale systematics behave similarly to large-scale systematics as the B-mode band-power measurement does not probe the same angular scales as the primary ξ_{\pm} cosmic shear statistic which is then used for cosmological parameter estimation (Abbott et al. 2016). In the RCSLenS data, Hildebrandt et al. (2016) find a significant high-amplitude B mode which extends to large scales. They argue that the uncertainty in the origin of this B mode does not allow for a robust mitigation strategy such that, in the era of high-precision cosmology, the high-amplitude large-scale measured B mode currently disqualifies the use of this survey for cosmic shear studies.

D6.1 Measurements of ξ_E and ξ_B

In Fig. D11, we present measurements of ξ_B using the same angular and tomographic binning as our primary measurement of ξ_+ shown in Fig. 5. In practice, we measure ξ_{\pm} in 3500 equally log-spaced θ bins from 0.5 to 300 arcmin. In order to complete the integral in equation (D8) with $\theta \rightarrow \infty$, we need a theoretical model to extend measurements of ξ_- beyond $\theta = 300$ arcmin: Our results are insensitive to a change between a *Planck* or CFHTLens cosmology to model this large-scale signal (Heymans et al. 2013; Planck Collaboration XIII 2016a). The small-scale measurements with $\theta < 10$ arcmin are unchanged if we truncate the integral at $\theta = 300$ arcmin.

We calculate the errors on ξ_B analytically, as the error derives from shape-noise only, and find the B mode detected in Fig. D11 to be significant. The probability that ξ_B is consistent with zero over all angular scales and tomographic bins is measured to be $p(\chi^2|\nu) = 0.005$. The amplitude of the B mode is, however, small (note the different vertical axes between the B modes presented in the lower right-hand panels of Fig. D11, and the signal ξ_+ presented in the upper left-hand panels). One approach to mitigate the impact of these systematics is to limit the angular scales used in the cosmological analysis. We find that the B mode is consistent with zero, with a probability $p(\chi^2|\nu) = 0.88$, when we restrict the measurement to $\theta > 4.2$ arcmin (i.e. removing the first three angular bins in each ξ_+ tomographic bin combination). We draw similar conclusions when the survey is analysed in 2D, finding significant B modes, but only on small scales $\theta \leq 4.2$ arcmin. Results from a preliminary, non-tomographic power spectrum analysis (Köhlinger et al. 2016; Köhlinger et al., in preparation) find the B modes to be consistent with zero for $\ell \leq 3700$, thus supporting the conclusion that the origin of the systematic is on small angular scales.

In an attempt to isolate the origin of the detected B mode, the following tests were carried out. Unfortunately, none aided our understanding of the source of the measured small-scale B mode:

(i) *Lower quality data.* Any tiles which had been flagged as potentially problematic through the data reduction validation checks, either for issues with scattered light or a lower quality astrometric solution, were removed from the survey in a reanalysis. The results were unchanged.

(ii) *Edge effects.* The survey was reanalysed removing a 10-arcmin-width border around the outer edge of each pointing. The results were unchanged.

(iii) *Pointing-to-pointing astrometry errors.* The survey was reanalysed using only those galaxy pairs which were observed within the same pointing. The small-scale signal was unchanged.

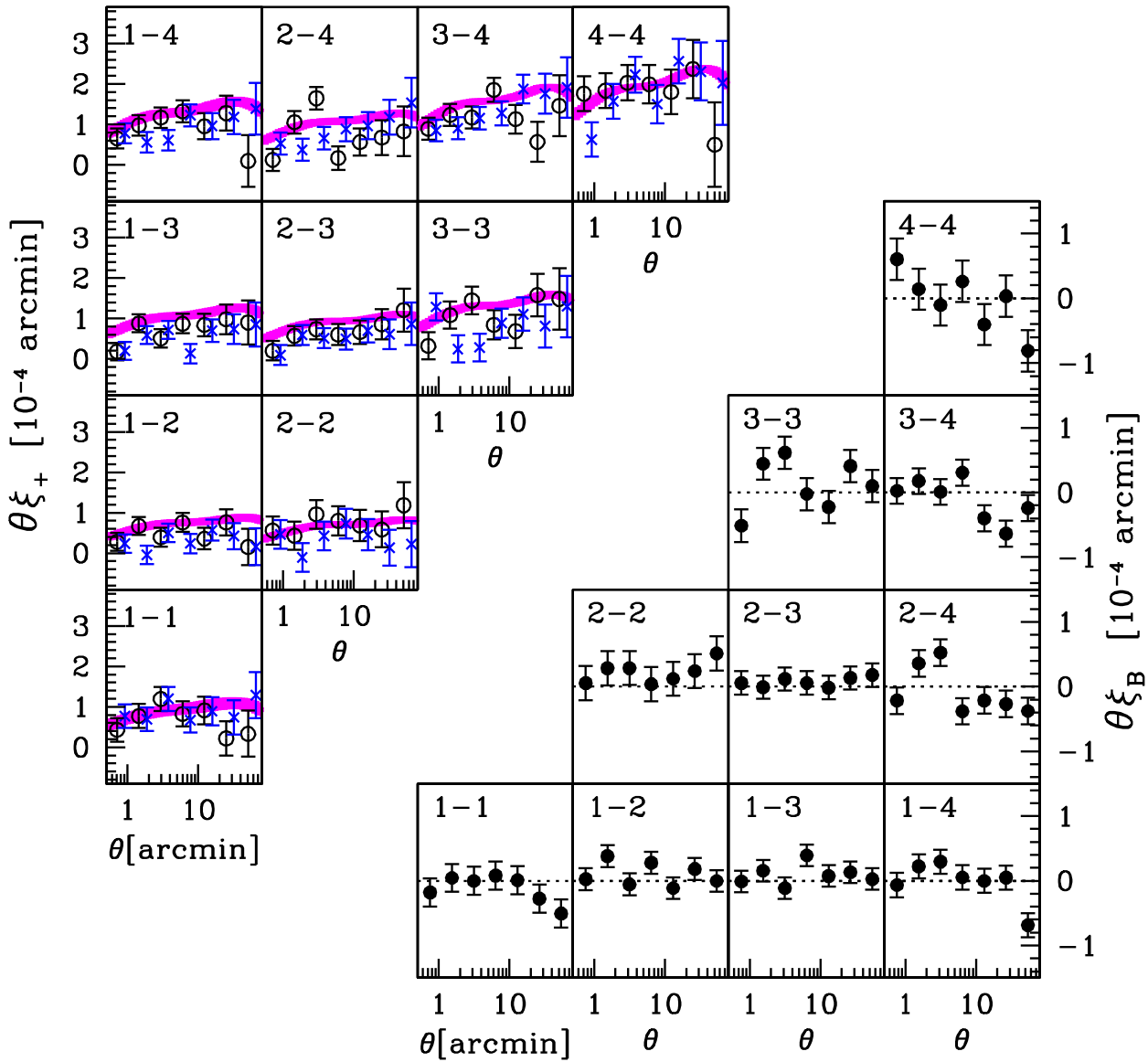


Figure D11. Tomography measurements using ξ_B for each redshift bin combination, as denoted in the caption inset in each panel. Lower right-hand panel: the measured B mode ξ_B (equation D7). Upper left-hand panel: Measurements of ξ_+^{obs} (open symbols) are corrected using the measured B mode (crosses, equation D11). The data with and without B-mode correction can be compared with the best-fitting cosmological model (solid) with its own error arising from uncertainty in the measured DIR redshift distribution.

(iv) *Quadrant errors.* The survey was split into four, based on which quadrant the galaxy was located within each pointing. The results from each quadrant were consistent.

(v) *PSF effects.* In Section D4, we argue that the PSF contamination to KiDS-450 is minimal with $|\alpha| < 0.03$, where α denotes the fractional PSF contamination to the shear measurement. In order to reproduce the amplitude of the measured small-scale B mode from PSF effects alone, we would require $\alpha = 0.15$. This PSF contribution would, however, also produce a significant large-scale B mode which we do not detect.

(vi) *PSF residuals.* The B mode and E mode of the residual PSF ellipticity correlation function were found to be consistent with zero, where the residual is measured as the difference between the measured stellar ellipticity and the PSF model at the

location of a star (see section 3.2.2 of Kuijken et al. 2015 for further details).

(vii) *PSF errors.* We apply a comprehensive method in order to isolate any pointings which have a significant PSF residual, finding no evidence for this type of contamination in Section D5. Nevertheless, we undertake a simple further test where we measure the B mode of the statistic $C^{\text{sys}} = \langle \epsilon \epsilon^* \rangle^2 / \langle \epsilon^* \epsilon^* \rangle$ (Bacon et al. 2003), finding it to be more than an order of magnitude smaller than the measured B mode and consistent with zero.

(viii) *Additive calibration correction.* We test the impact of the additive calibration correction detailed in Section D4. Applying no correction to the survey increases the B modes measured on large scales, but leaves the small-scale signal unchanged.

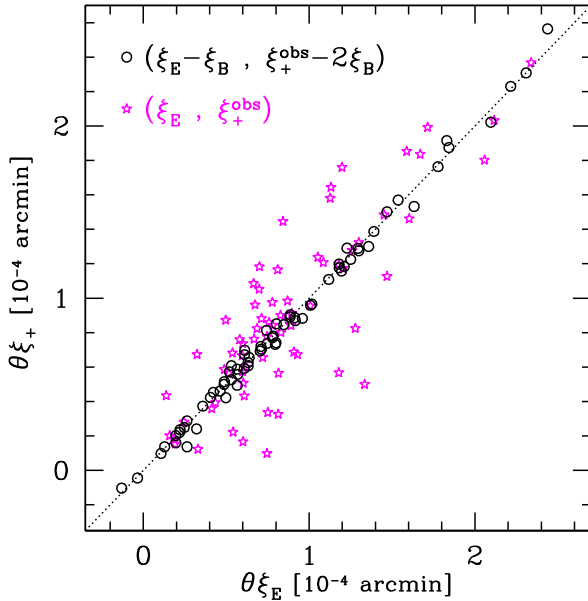


Figure D12. Comparison of estimators for ξ_+ where in the absence of systematics $\xi_E = \xi_+^{\text{obs}}$. Each data point is one of the 70 components of the tomographic ξ_+ data vector, comparing the E-mode measurement ξ_E with the measured two-point correlation function ξ_+^{obs} at the same θ scale in each tomographic combination of redshift bins (shown as stars). Under the assumption that the contaminating systematic contributes equally to the tangential and cross distortions, we can correct ξ_E and ξ_+^{obs} with equations (D9) and (D10) (shown as circles), respectively. After this correction has been applied, the agreement between the two estimators for ξ_+ is significantly improved.

(ix) *Chip-position-dependent errors.* In Section D4, we find no significant dependence on the amplitude of the additive bias c on galaxy position within the field of view. To further analyse this effect, we bin the data by position (x, y) within each pointing to construct a (noisy) map of $c(x, y)$. We then measure the contribution to ξ_B from a position-dependent additive bias modelled using the mean measured $c(x, y)$ across the full survey and also per patch. We find a small contribution to the measured small-scale B mode at the level of 10 per cent of the measured value. If we correct for a position-dependent c -term using the noisy $c(x, y)$ map, however, we find that the noise serves only to increase the overall B mode by 10 per cent rather than decreasing the signal. For a more detailed analysis of position-dependent additive bias within CFHTLenS and KiDS-DR2 data, see van Uitert & Schneider (2016).

(x) *Seeing and PSF variation.* We separate the pointings based on their measured seeing and PSF ellipticity, finding no significant difference in the resulting measured E and B modes.

(xi) *Astrometric errors.* We test whether random errors in the astrometric solution could cause B modes. Under the assumption that the VST OmegaCAM camera shear is relatively stable (as motivated by de Jong et al. 2015), we can estimate a spatially dependent astrometric error from the measured camera shear per pointing (see e.g. Erben et al. 2013). Defining astrometric errors in this way produced E- and B-mode measurements which were insignificant in comparison to the measured $\xi_{E/B}$.

Unfortunately, none of our tests were able to isolate the B mode or reveal its origin, but we can nevertheless proceed to test the assumption that whatever is the source of the B mode, the contam-

inating systematic contributes equally to the tangential and cross distortions. In Fig. D12, we compare the measured E-mode ξ_E with the measured ξ_+^{obs} across all 70 points in the ξ_+ data vector (7 angular bins in 10 different tomographic bin combinations). In the absence of systematics, $\xi_E = \xi_+^{\text{obs}}$, with some scatter in this relationship as the E-B decomposition method reduces the shot-noise variance on the measurement of ξ_+ by a factor of $\sqrt{2}$. We correct ξ_E and ξ_+^{obs} with equations (D10) and (D11), finding that the agreement between the two estimators for ξ_+ is significantly improved when this correction is applied. This comparison supports the assumption that the contaminating systematic contributes equally to the tangential and cross distortions: If that were not the case, the agreement between ξ_E and ξ_+^{obs} would deteriorate after the correction was applied. This analysis therefore provides an important consistency check and validates our approach of using the B mode to correct ξ_+^{obs} in Section 6.5.

APPENDIX E: PIPELINE REDUNDANCY: PIXELS TO COSMOLOGICAL PARAMETERS

This paper documents the primary pipeline analysis from raw pixels through to cosmological parameters. In this section, we record the cross-checks within the pipeline along with any redundancy, that is, the extra components which are not always strictly necessary but are used to ensure that the primary analysis is robust.

(i) *Data reduction.* The raw pixel data have been reduced using two independent pipelines, THELI and ASTRO-WISE, and there is a good level of agreement between the two reductions. The THELI reduction, which is optimized for weak-lensing analyses by including a global astrometric solution, is then used for the lensing image analysis. The ASTRO-WISE reduction, which is optimized for the large-volume multicolour data, is then used for the photometry analysis.

(ii) *Catalogue handling.* There are numerous steps in the catalogue pipeline analysis from reduced images through to the final catalogue product. The pipeline team used a central GIT repository, and major changes and upgrades to the scripts were verified by a second person within the team before they were committed to the master branch.

(iii) *Photometric redshifts.* As detailed in Section 3 and Appendix C, we investigate four different methods to determine the redshift distributions of our tomographic source samples. The derived cosmological parameters for all four methods are in agreement with each other.

(iv) *Shear correlation function measurement.* We use the ATHENA tree-code (Kilbinger, Bonnett & Coupon 2014) to measure the tomographic shear correlation function ξ_\pm . This was found to agree well with an alternative measurement using the TREECORR software (Jarvis 2015).

(v) *Covariance matrices.* As detailed in Section 5, we investigate three different methods to determine the covariance matrix, finding consistent results for the derived cosmological parameters from both our numerical and analytical estimates.

(vi) *Cosmological parameter estimates:* Our cosmological parameter likelihood analysis uses a modified version of COSMOMC (Lewis & Bridle 2002), as described in Joudaki et al. (2016a).¹⁶ This pipeline underwent a series of cross-checks, verifying the cosmic shear and intrinsic alignment theoretical modelling through comparison to the NICAIA software (Kilbinger et al. 2009) and private

¹⁶ https://github.com/sjoudaki/cfhtlens_revisited

Table F1. Mean and 68 per cent confidence intervals on the primary model parameters. Note that the parameters $\Omega_b h^2$, θ_{MC} , n_s , and B are heavily constrained by the priors rather than by the KiDS-450 data.

	$\Omega_b h^2 (10^{-2})$	$\Omega_c h^2$	$100\theta_{\text{MC}}$	$\ln(10^{10} A_s)$	n_s	A_{IA}	B
KiDS-450	$2.23^{+0.37}_{-0.33}$	$0.116^{+0.029}_{-0.056}$	$1.0472^{+0.0603}_{-0.0456}$	$3.09^{+0.57}_{-1.21}$	$1.09^{+0.20}_{-0.06}$	$1.10^{+0.68}_{-0.54}$	$2.88^{+0.30}_{-0.88}$
DIR	$2.23^{+0.37}_{-0.33}$	$0.119^{+0.031}_{-0.061}$	$1.0504^{+0.0642}_{-0.0459}$	$3.08^{+0.51}_{-1.26}$	$1.02^{+0.12}_{-0.14}$	$1.14^{+0.65}_{-0.55}$	–
CC	$2.24^{+0.36}_{-0.34}$	$0.143^{+0.047}_{-0.060}$	$1.0711^{+0.0645}_{-0.0362}$	$2.84^{+0.32}_{-1.14}$	$1.05^{+0.16}_{-0.13}$	$0.80^{+1.02}_{-0.96}$	–
BOR	$2.22^{+0.11}_{-0.32}$	$0.097^{+0.018}_{-0.052}$	$1.0248^{+0.0534}_{-0.0622}$	$3.44^{+1.21}_{-0.80}$	$1.03^{+0.12}_{-0.12}$	$-0.92^{+0.99}_{-0.71}$	–
BPZ	$2.22^{+0.38}_{-0.32}$	$0.099^{+0.017}_{-0.054}$	$1.0250^{+0.0538}_{-0.0674}$	$3.49^{+1.51}_{-0.48}$	$1.04^{+0.13}_{-0.13}$	$-1.10^{+0.96}_{-0.70}$	–
DIR-no-error	$2.23^{+0.37}_{-0.33}$	$0.120^{+0.031}_{-0.064}$	$1.0495^{+0.0661}_{-0.0513}$	$3.10^{+0.44}_{-1.40}$	$1.02^{+0.13}_{-0.13}$	$1.20^{+0.62}_{-0.52}$	–
B mode	$2.23^{+0.37}_{-0.33}$	$0.101^{+0.020}_{-0.055}$	$1.0251^{+0.0568}_{-0.0638}$	$3.43^{+1.57}_{-1.73}$	$0.97^{+0.12}_{-0.14}$	$1.11^{+0.67}_{-0.55}$	–
ξ_+ large scales	$2.24^{+0.36}_{-0.34}$	$0.132^{+0.050}_{-0.052}$	$1.0616^{+0.0666}_{-0.0355}$	$2.79^{+0.28}_{-1.09}$	$0.96^{+0.12}_{-0.16}$	$1.07^{+0.79}_{-0.59}$	–
No systematics	$2.22^{+0.38}_{-0.32}$	$0.106^{+0.022}_{-0.058}$	$1.0341^{+0.0610}_{-0.0614}$	$3.32^{+1.68}_{-1.62}$	$1.00^{+0.12}_{-0.12}$	–	–

Table F2. Mean and 68 per cent confidence intervals for certain derived cosmological parameters of interest. Note that the constraints on H_0 are dominated by the prior rather than the data. Further included are the best-fitting χ^2_{eff} values, number of degrees of freedom (dof), and DIC values for each setup.

	Ω_m	σ_8	$S_8 = \sigma_8 \times \sqrt{\Omega_m}/0.3$	$H_0 (\text{km s}^{-1} \text{Mpc}^{-1})$	χ^2_{eff}	dof	DIC
KiDS-450	$0.250^{+0.053}_{-0.103}$	$0.849^{+0.120}_{-0.204}$	$0.745^{+0.038}_{-0.038}$	$74.7^{+7.2}_{-2.5}$	162.5	122	178.6
DIR	$0.254^{+0.058}_{-0.109}$	$0.826^{+0.115}_{-0.199}$	$0.727^{+0.034}_{-0.030}$	$75.0^{+6.9}_{-2.5}$	163.5	123	178.5
CC	$0.304^{+0.086}_{-0.114}$	$0.847^{+0.107}_{-0.234}$	$0.816^{+0.070}_{-0.094}$	$74.2^{+7.5}_{-3.5}$	159.0	123	191.8
BOR	$0.213^{+0.035}_{-0.096}$	$0.860^{+0.170}_{-0.174}$	$0.693^{+0.037}_{-0.031}$	$75.3^{+6.7}_{-2.3}$	172.1	123	182.5
BPZ	$0.215^{+0.035}_{-0.098}$	$0.884^{+0.186}_{-0.164}$	$0.714^{+0.040}_{-0.034}$	$75.2^{+6.7}_{-2.3}$	173.5	123	184.2
DIR-no-error	$0.254^{+0.060}_{-0.114}$	$0.830^{+0.116}_{-0.211}$	$0.729^{+0.034}_{-0.029}$	$75.0^{+6.9}_{-2.8}$	166.4	123	174.7
B mode	$0.226^{+0.042}_{-0.105}$	$0.850^{+0.179}_{-0.183}$	$0.702^{+0.036}_{-0.029}$	$74.2^{+7.5}_{-3.0}$	142.0	123	151.8
ξ_+ large scales	$0.282^{+0.093}_{-0.099}$	$0.746^{+0.074}_{-0.187}$	$0.692^{+0.040}_{-0.035}$	$74.4^{+7.5}_{-3.5}$	133.7	93	141.2
No systematics	$0.228^{+0.044}_{-0.106}$	$0.846^{+0.145}_{-0.203}$	$0.703^{+0.031}_{-0.025}$	$75.1^{+6.8}_{-2.4}$	169.4	124	177.3

code within the team. In addition, we used MONTEPYTHON and CLASS (Blas, Lesgourgues & Tram 2011; Audren et al. 2013), as described in Köhlinger et al. (2016), to provide another consistency check with a completely independent likelihood code. The cosmological constraints from these two independent analyses are in good agreement.

(vii) ξ_+ versus ξ_- . We found consistent cosmological constraints when using only ξ_+ or only ξ_- , with ξ_- favouring slightly lower values of S_8 in comparison to ξ_+ . The constraints from ξ_+ alone are very similar to the constraints where the two statistics are analysed in combination, as ξ_+ carries the highest S/N, as shown in Fig. 4.

(viii) *2D versus tomography*. Our primary cosmological parameter likelihood analysis uses four tomographic bins. We also determined the cosmological constraints from a ‘2D’ case using all source galaxies selected with $0.1 < z_B < 0.9$, excluding systematics modelling. The cosmological constraints were in excellent agreement with the tomographic ‘no-systematics’ case analysis.

APPENDIX F: BEST-FITTING MODEL PARAMETERS

In Tables F1 and F2, we present detailed results for the best-fitting model parameters for all MCMC runs described in Table 4. We include the seven primary parameters, along with a few derived parameters of interest. Note that the primary parameters $\Omega_b h^2$, θ_{MC} , n_s , and B are heavily constrained by the priors rather than by the KiDS-450 data. The same is true for the derived parameter H_0 . We report the χ^2_{eff} of the best-fitting model, the number of degrees of freedom and the ‘Deviance Information Criterion’ (DIC; Joudaki et al. 2016a). Fig. F1 shows 2D projections of the confidence region in 7D primary parameter space for all combinations of parameters in the primary KiDS-450 run. A similar plot for derived parameters can be found in Fig. F2.

The full cosmological analysis was also carried out with the two other blindings. Those yielded a tension in the S_8 parameter with respect to *Planck* of 1.7 and 2.8σ , respectively.

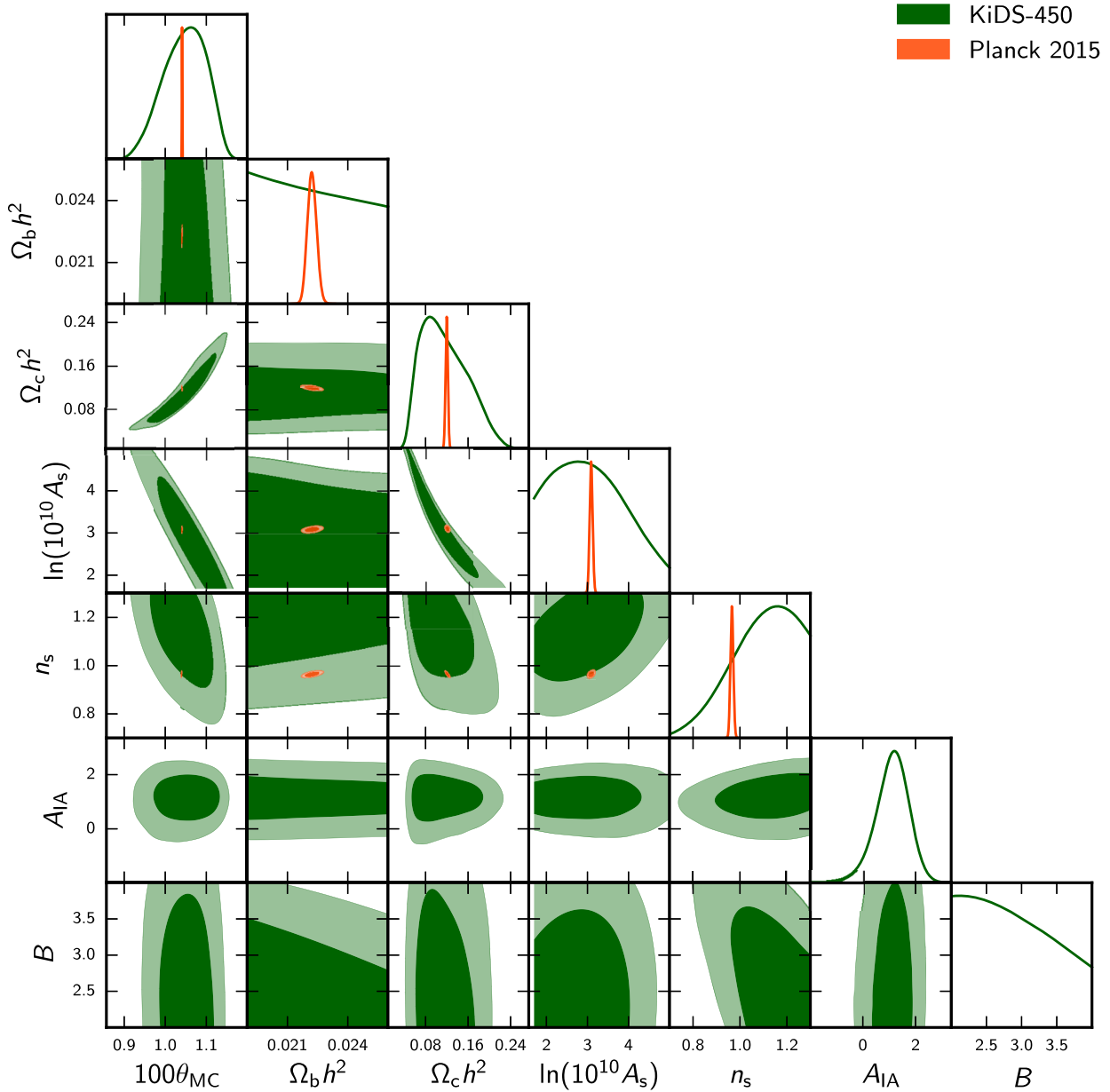


Figure F1. Posterior distributions of the primary model parameters and their correlation. Parameter definitions and priors are listed in Table 3.

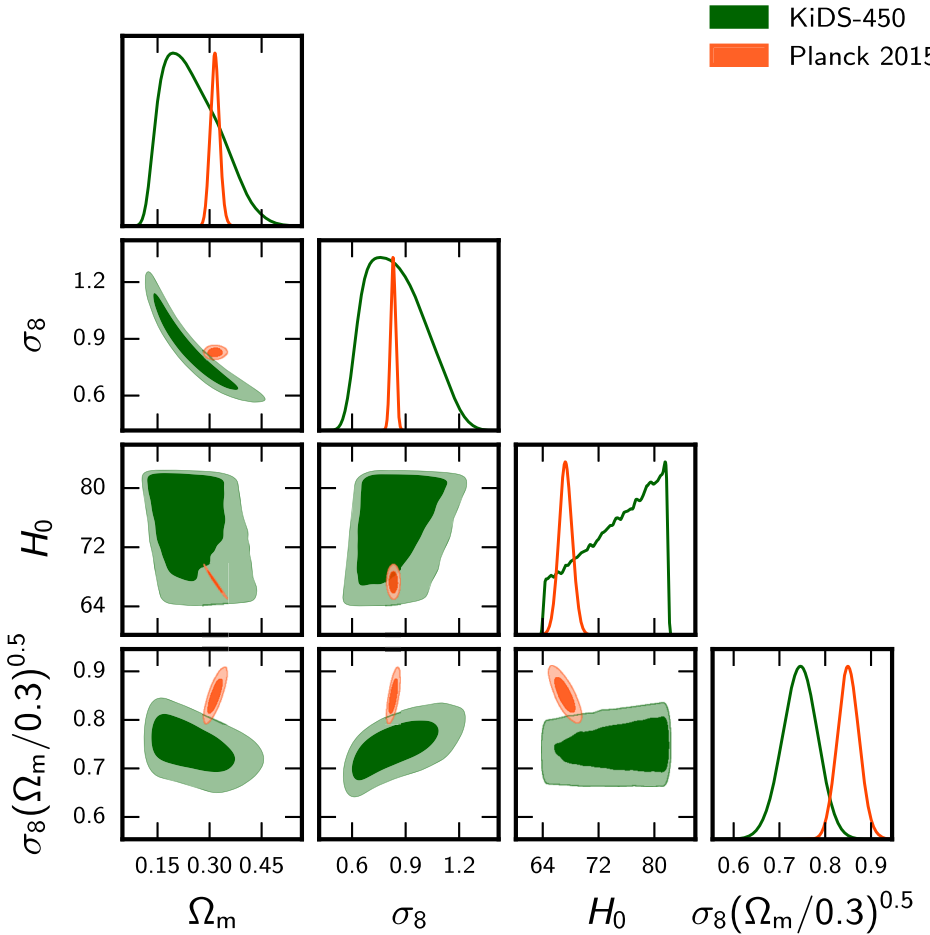


Figure F2. Posterior distributions of derived cosmological parameters and their correlation.

¹Argelander-Institut für Astronomie, Auf dem Hügel 71, D-53121 Bonn, Germany

²Leiden Observatory, Leiden University, Niels Bohrweg 2, NL-2333 CA Leiden, the Netherlands

³Institute for Astronomy, University of Edinburgh, Royal Observatory, Blackford Hill, Edinburgh EH9 3HJ, UK

⁴Centre for Astrophysics and Supercomputing, Swinburne University of Technology, PO Box 218, Hawthorn, VIC 3122, Australia

⁵University College London, Gower Street, London WC1E 6BT, UK

⁶Department of Physics, University of Oxford, Denys Wilkinson Building, Keble Road, Oxford OX1 3RH, UK

⁷Kapteyn Astronomical Institute, University of Groningen, NL-9700AD Groningen, the Netherlands

⁸Department of Physics, University of Napile Federico II, via Cintia, I-80126 Napoli, Italy

⁹Institute of Space Sciences and Astronomy (ISSA), University of Malta, Msida, MSD 2080, Malta

¹⁰Department of Physics, University of Malta, Msida, MSD 2080, Malta

¹¹INAF – Osservatorio Astronomico di Capodimonte, Via Moiariello 16, I-80131 Napoli, Italy

¹²Department of Physics and Astronomy, University of British Columbia, 6224 Agricultural Road, Vancouver, BC V6T 1Z1, Canada

¹³INAF – Osservatorio Astronomico di Padova, via dell’Osservatorio 5, I-35122 Padova, Italy

This paper has been typeset from a $\text{\TeX}/\text{\LaTeX}$ file prepared by the author.